REAL-TIME AUTONOMY AND MANEUVERING SIMULATION OF AN UNMANNED UNDERWATER VEHICLE NEAR A MOVING SUBMARINE USING ACTIVELY SAMPLED GAUSSIAN PROCESS SURROGATE MODELS

by

Brady M. Hammond

Submitted to the Department of Mechanical Engineering
in partial fulfillment of the requirements for the degree of

Doctor of Philosophy in Mechanical Engineering

at the

MASSACHUSETTS INSTITUTE OF TECHNOLOGY

June 2023

© 2023. Brady M. Hammond. The author hereby grants to MIT a nonexclusive, worldwide, irrevocable, royalty-free license to exercise any and all rights under copyright, including to reproduce, preserve, distribute and publicly display copies of the thesis, or release the thesis under an open-access license.

Author ....
Department of Mechanical Engineering
April 21, 2023

Certified by..
Themistoklis P. Sapsis
Professor
Thesis Supervisor

Accepted by ....
Nicolas Hadjiconstantinou
Chairman, Department Committee on Graduate Theses

REAL-TIME AUTONOMY AND MANEUVERING SIMULATION OF AN UNMANNED UNDERWATER VEHICLE NEAR A MOVING SUBMARINE USING ACTIVELY SAMPLED GAUSSIAN PROCESS SURROGATE MODELS

by

Brady M. Hammond

Submitted to the Department of Mechanical Engineering
on April 21, 2023, in partial fulfillment of the
requirements for the degree of
Doctor of Philosophy in Mechanical Engineering

Abstract

Unmanned Underwater Vehicle (UUV) maneuvering simulators have severe limitations on modeling UUV motion near a moving submarine because they are not capable of determining the complex, turbulent, hydrodynamic interactions in real time. Potential flow solvers are typically fast enough, but they neglect viscosity which introduces large inaccuracies that play a critical role in control. On the other hand, Computational Fluid Dynamics (CFD) accurately models these hydrodynamic interactions, but a simulation of a single UUV in one specific configuration typically takes hours or days to complete. Therefore, it is not practical for real-time applications. To bridge this gap, a machine learning framework based on actively sampled Gaussian Process (GP) regression is developed to create a reduced-order model (ROM) that predicts the hydrodynamic interactions in real time using a minimum number of expensive simulations.

We show that the introduced active learning framework, called Non-Myopic Multi-Fidelity (NMMF) active learning for GP regression, significantly and parsimoniously accelerates the convergence of the surrogate model by combining the low cost of the low-fidelity, potential flow simulations to explore the domain, as well as optimally selected high-fidelity CFD simulations as training data to improve the model accuracy. It is shown that the resulting GP regression model captures accurately and efficiently the hydrodynamic interactions between the UUV and the moving submarine. Based on the developed algorithms, we are able to define operating envelopes that outline regions where the UUV safely overcomes the hydrodynamic interactions, as well as, regions where the UUV is overpowered and collides with the submarine. This approach also enables us to develop new autonomous protocols that compensate for the hydrodynamic interactions, by adjusting the desired UUV heading and speed, which enables the UUV to safely stay on the desired course. A sensitivity analysis confirms the robustness of the presented control strategies. The developed ideas pave the way for control algorithms in complex environments, such as turbulent boundary layers, which were previously impossible to navigate in real-time.

Thesis Supervisor: Themistoklis P. Sapsis
Title: Professor

Acknowledgments

I am truly grateful for the opportunity to pursue my Doctoral degree at the Massachusetts Institute of Technology (MIT). I am so amazed by the brilliant achievements and selfless work ethic of people that have mentored me and worked alongside me throughout my time at MIT. Serving in the United States Navy has been one of the greatest honors of my life. I feel so blessed that I was given the opportunity to join the Naval Construction and Engineering program and be a part of this amazing cohort.

First, I wish to thank my advisor Themistoklis Sapsis. His guidance and mentorship have been invaluable. I have no idea how one person can have such expertise in so many different fields. Because this thesis bridged many different fields of expertise, his guidance was vital to the completion of this study. Additionally, all of the individuals in the Stochastic Analysis and Nonlinear Dynamics (SAND) lab have been monumentally helpful in my work. Their continual input and feedback throughout my research has had an immeasurable impact.

I would also like to extend a special thanks to the following individuals. Their guidance and input has played a vital role in shaping this research and has provided a major contribution to the impact of this study.

- Chris Harding, Geoffrey McNally, and others in the Warfare Integrated Systems Branch, Naval Undersea Warfare Center
- Sasha Tsarev and others in the Maritime Systems Hydromechanics Branch, Naval Surface Warfare Center
- CDR Kyle Weorner, the Program Manager of the Tactical Technology Office, Defense Advanced Research Projects Agency
- Daniel Milligan, the Undersea Vehicles Lead and many others at General Dynamics Electric Boat

- Joel Parry, the Maritime Warfare and ISR, Business Area Lead, and many others at Draper Laboratory
- David A. Drazen, the Chief Technology Officer, and others at the Naval Surface Warfare Center
- Supun Randeni of the MIT Sea Grant and Tyler Paine of the MIT Marine Autonomy Lab

Most importantly, I wish to thank my loving wife Jackie. The unwavering love, support, and commitment that she has given me has been the enabling power to allow me to pursue my dreams. There is no way I could have done this without her and am so grateful for her wonderful example, friendship, and strength.

Contents

1 Introduction **23**

1.1 Motivation . . . 23

1.2 Hydrodynamics . . . 28

1.2.1 Experimental Fluid Dynamics . . . 29

1.2.2 Parametric Models . . . 30

1.2.3 Potential Flow . . . 31

1.2.4 Computational Fluid Dynamics . . . 32

1.3 Machine Learning . . . 34

1.3.1 Active Learning . . . 37

1.4 Thesis Objective . . . 37

1.4.1 Thesis Problem Statement . . . 38

1.4.2 List of Contributions . . . 38

1.5 Thesis Outline . . . 39

2 Non-Myopic Multi-Fidelity Active Learning **41**

2.1 Introduction . . . 41

2.2 Background . . . 44

2.2.1 Gaussian Process Regression . . . 44

2.2.2 Active Learning . . . 46

2.2.3 Myopic versus Non-Myopic Active Learning Algorithms . . . 47

2.2.4 Multi-Fidelity Modeling . . . 49

2.3 Non-Myopic Multi-Fidelity Active Learning . . . 52

2.3.1 Inter-Model Acquisition Function 52
2.3.2 Non-Myopic Multi-Fidelity (NMMF) Active Learning Algorithm 55
2.3.3 Advantages of Multi-Fidelity Gaussian Process Regression Model 57
2.4 Evaluation of NMMF Active Learning Algorithm 58
2.4.1 Park Function 58
2.4.2 Three DOF trebuchet with a hinged counterweight and sling . 60
2.4.3 Borehole Function 63
2.4.4 Subsonic Straight-Tapered Wing Lift Curve Slope 65
2.5 Adaptations for Multi-Dimensional Outputs 67
2.6 Conclusion 71

3 Computational Modeling of Multiple Body Hydrodynamic Interactions 73
3.1 Introduction 73
3.2 Vehicle Configuration 74
3.3 Computational Fluid Dynamics 76
3.3.1 Introduction 76
3.3.2 Governing Equations 77
3.3.3 Single Vehicle CFD Simulation 79
3.3.3.1 Domain 79
3.3.3.2 Mesh 81
3.3.3.3 Boundary Layer and Turbulence Modeling 82
3.3.3.4 Angled Vehicle Simulation 84
3.3.3.5 Results and Validation 86
3.3.4 Multiple Vehicle CFD Simulation 89
3.3.4.1 Domain 89
3.3.4.2 Mesh 90
3.3.4.3 Boundary Layer and Turbulence Modeling 91
3.3.4.4 Results and Validation 93
3.4 Potential Flow 95

3.4.1 Governing Equations 95
3.4.2 Results and Validation 96
3.5 Evaluation of One-Way Assumption 97
3.6 Conclusion 106

4 Reduced Order Modeling of Hydrodynamic Interactions between a UUV and Submarine 109
4.1 Introduction 109
4.2 Input Variables 110
4.2.1 Three Degree of Freedom Simulation 112
4.2.2 Quasi-Static Simulation 113
4.2.3 Domain of Input Variables for Surrogate Model 114
4.3 Constraints 118
4.4 Reduced Order Model Approach 121
4.5 Results 123
4.6 Validation 132
4.7 Conclusion 133

5 Simulating UUV Motion with Hydrodynamic Interactions 135
5.1 Introduction 135
5.2 Approach 136
5.3 Deviations from MOOS-IvP 139
5.4 Equations of Motion 141
5.5 Gaussian Process Regression 149
5.6 Control Theory 153
5.7 Autonomous Behaviors 154
5.8 Robustness 157
5.9 UUV Simulation Setup 161
5.10 UUV Simulation Validation 161
5.11 Results 163
5.11.1 Force and Moment Maps 163

5.11.2 Results for Standard UUV 164
5.11.3 Effects of Waves 167
5.12 Conclusion 172

6 Developing Autonomous Behaviors to Overcome Hydrodynamic Interactions 175
6.1 Introduction 175
6.2 Approach 176
6.3 Autonomous Behaviors 177
6.3.1 N_{uv} Compensating Behavior 177
6.3.2 Modified Waypoints Behavior 181
6.4 Results 185
6.4.1 Results for N_{uv} Compensating Behavior 185
6.4.2 Effects of Waves 189
6.5 Conclusions 193

7 Conclusion 195
7.1 Summary 195
7.2 Future Work 197

A Code Documentation 199
A.1 Overview 199

List of Figures

1-1 Submarine and UUV hydrodynamic interaction 27

2-1 Active sampling method 47
2-2 Myopic sampling algorithm 48
2-3 Non-myopic sampling algorithm 49
2-4 Inter-model acquisition function 54
2-5 Different sampling algorithms on Park function 59
2-6 3DOF trebuchet 60
2-7 Different sampling algorithms on 3DOF trebuchet 62
2-8 Different sampling algorithms on borehole function 64
2-9 Different sampling algorithms on wing lift curve slope 67
2-10 Multiple output active sampling methods 70

3-1 Geometry and orientation of vehicle configuration 76
3-2 SUBOFF model CFD simulation domain 80
3-3 SUBOFF model CFD simulation domain symmetry 81
3-4 SUBOFF model CFD simulation mesh 82
3-5 SUBOFF model CFD simulation boundary layer mesh 83
3-6 SUBOFF model CFD simulation y^+ 84
3-7 Angled SUBOFF model CFD simulation mesh 85
3-8 Angled SUBOFF model CFD simulation boundary layer mesh 85
3-9 Angled SUBOFF model CFD simulation y^+ 86
3-10 Non-zero heading angle SUBOFF model CFD validation 87

3-11 Two vehicle CFD simulation domain 90
3-12 Two vehicle CFD simulation mesh 91
3-13 Two vehicle CFD simulation mesh boundary layer 92
3-14 Two vehicle CFD simulation y^+ 92
3-15 Two vehicle CFD validation 94
3-16 Non-zero heading angle SUBOFF model P-Flow validation 96
3-17 Fluid velocity profile around SUBOFF model 98
3-18 Fluid velocity profile of one-way assumption 99
3-19 Fluid velocity profile of two vehicles 100
3-20 Fluid velocity profile of UUV near submarine mid-body 101
3-21 Fluid velocity profile of UUV near submarine bow 103
3-22 Different cases used to evaluate the one-way assumption 104

4-1 UUV and inertial coordinate systems 110
4-2 Geometric configuration of lateral constraint on ROM 119
4-3 L/D_{UUV} vs. D_{Sub}/D_{UUV} and constraints 120
4-4 Hydrodynamic interactions: Y' and N' for R_{Lat} vs. R_{Long} 124
4-5 Hydrodynamic interactions: X' for different R_{Long} 125
4-6 Hydrodynamic interaction: Pressure field 126
4-7 Hydrodynamic interactions: Y' and N' for ψ vs. u 127
4-8 Hydrodynamic interactions: X' for different L/D_{UUV} 128
4-9 Hydrodynamic interactions: High and low fidelity Y' and N' for R_{Lat} vs. R_{Long} 130
4-10 Hydrodynamic interactions: High and low fidelity Y' and N' for ψ vs. u131
4-11 Hydrodynamic interactions: High and low fidelity X' for L/D_{UUV} vs. ψ132

5-1 UUV and inertial coordinate systems 137
5-2 UUV control system block diagram 138
5-3 Block diagram of GP surrogate integration into UUV control system . 153
5-4 Waypoints behavior 155
5-5 UUV collision with submarine 156

5-6 Example of UUV maneuvering in waves 160
5-7 Four-degree rudder validation 162
5-8 Alpha mission validation 163
5-9 Hydrodynamic interactions: Y_s' and N_s' for R_{Lat} vs. R_{Long} 164
5-10 Operating envelopes 165
5-11 Operating envelopes at different d_{lead} 167
5-12 Operating envelopes in SS6 at 50 meters 168
5-13 Operating envelopes in SS6 at 90 meters 170
5-14 Operating envelopes in SS5 at 50 meters 171

6-1 Block diagram of GP surrogate integration into UUV control system . 177
6-2 Standard waypoint behavior vs. N_{uv} compensation 180
6-3 Demonstration of standard waypoints behavior 182
6-4 Modified waypoints behavior 183
6-5 Speed policy 184
6-6 Comparison of standard and modified waypoints behavior 185
6-7 Operating envelopes with and without N_{uv} compensation 186
6-8 Operating envelopes with N_{uv} compensation at different γ 188
6-9 Operating envelopes with and without N_{uv} compensation in SS5 at 50 meters 190
6-10 Operating envelopes with and without N_{uv} compensation in SS6 at 90 meters 191
6-11 Operating envelopes with and without N_{uv} compensation in SS6 at 50 meters 192

A-1 Block diagram of GP surrogate integration into UUV simulator . . . 201

THIS PAGE INTENTIONALLY LEFT BLANK

List of Tables

1.1 UUV classification based on vehicle size 25
1.2 Different missions of different size UUVs 25

3.1 CFD validation of zero degree heading angle SUBOFF model 87
3.2 CFD validation of SUBOFF model at various heading angles 88
3.3 Comparison of one-way assumption and unassumed hydrodynamic interactions 104

4.1 Sizes of various UUVs 116
4.2 Input variables for reduced order model 117
4.3 Error of the GP regression model outputs 133

5.1 Sea state parameters 158

THIS PAGE INTENTIONALLY LEFT BLANK

Acronyms

AMC	Australian Maritime College.
ASW	Anti-Submarine Warfare.
AUV	Autonomous Underwater Vehicle.
BEM	Boundary Element Method.
BSLRSM	Baseline Reynolds Stress Model.
CAD	Computer Aided Design.
CB	Center of Buoyancy.
CFD	Computational Fluid Dynamics.
CN3	Communication/Navigation Network Nodes.
DARPA	Defense Advanced Research Projects Agency.
DNS	Direct Numerical Solution.
DOE	Design of Experiments.
DOF	Degree of Freedom.
DSTO	Defense.
EFD	Experimental Fluid Dynamics.
GP	Gaussian Process.
HWV	Heavy Weight Vehicle.
ID	Identification.
IO	Information Operations.
ISE	International Submarine Engineering.
ISR	Intelligence.
ITTC	International Towing Tank Conference.

L&R	Launch and Recovery.
LOA	Length Over All.
LWV	Light Weight Vehicle.
MAE	Mean Absolute Error.
MAPE	Mean Absolute Percentage Error.
MCM	Mine Countermeasures.
MIT	Massachusetts Institute of Technology.
NCMEH	National Centre for Maritime Engineering and Hydrodynamics.
NMMF	Non-Myopic Multi-Fidelity.
NPS	Naval Postgraduate School.
OED	Optimal Experimental Design.
PID	Proportional Integral Derivative.
PMS 406	Unmanned Maritime Systems Program Office.
RBF	Radial Basis Function.
ROM	Reduced Order Model.
ROV	Remotely Operated Vehicle.
SAND	Stochastic Analysis and Nonlinear Dynamics.
SDV	Swimmer Delivery Vehicle.
SST	Shear-Stress Transport.
TCS	Time Critical Strike.
US	United States.
USN	United States Navy.
UUV	Unmanned Underwater Vehicle.
VPT	Virginia Payload Tube.

Nomenclature

A	Wave Amplitude.
B	UUV Buoyancy.
c	Clearance Between Vehicles.
$\mathcal{D}$	Data Set.
D_{Sub}	Submarine Diameter.
D_{UUV}	UUV Diameter.
d	Input Dimension of Surrogate Model.
d_{lead}	Lead Distance.
d_{off}	Lead Offset for Modified Waypoints Behavior.
d_{perp}	Perpendicular Distance from Track-line.
F_a	Hydrodynamic Force due to Added Mass.
F_B	UUV Body Forces.
F_C	UUV Control Forces.
F_d	Hydrodynamic Force due to Damping.
F_{HS}	Hydrostatic Force.
I	Moment of Inertia.
K	Rolling Moment.
K_d	Derivative Gain.
K_i	Integral Gain.
K_p	Proportional Gain.
K_{Prop}	Propeller Torque.
$K_{yy}(\mathbf{X}_*, \mathbf{X}'_*)$	Surrogate Predicted Covariance.

k	Wave Number.
$k(x, x')$	Gaussian Process Covariance Function or Kernel.
L/D_{UUV}	UUV Length-to-Diameter Ratio.
L_{Sub}	Submarine Length.
L_{UUV}	UUV Length.
M	Pitching Moment.
$\mathbf{M}$	Inertial Matrix.
M_a	Hydrodynamic Moment due to Added Mass.
M_d	Hydrodynamic Moment due to Damping.
m	Mass.
$m_{i_1 i_2}$	Added Mass.
N	Yawing Moment.
N_s	Surrogate Model Yawing Moment.
N'	Yawing Moment Coefficient.
N'_s	Surrogate Model Yawing Moment Coefficient.
n	Number of Samples.
P	Pressure.
p	Roll Velocity.
q	Pitch Velocity.
q_{IM}	Inter-Model Acquisition Function.
R_{UUV}	UUV Radius.
R_{Lat}	Latitudinal Separation Ratio.
R_{Long}	Longitudinal Separation Ratio.
Re	Reynolds Number.
r	Yaw Velocity.
U	Velocity.
U_{ot}	Overtaking Velocity.
U_{Sub}	Submarine Velocity.
$\mathbf{u}$	Input Vector.
u	Surge Velocity.

u_d	Desired UUV Speed.
u_w	Wave Surge Velocity.
v	Sway Velocity.
v_{comp}	Theoretical Compensated Sway Velocity.
v_w	Wave Sway Velocity.
W	UUV Weight.
w	Heave Velocity.
X	Surge Force.
$\mathbf{X}$	Inputs in Data Set.
$\mathbf{X}_*$	Inputs where Predicted Mean/Variance are Desired.
X_s	Surrogate Model Surge Force.
X'	Surge Force Coefficient.
X'_s	Surrogate Model Surge Force Coefficient.
X_{Prop}	Propeller Thrust.
x	x Cartesian Coordinate.
x^*	Optimal Sampling Location.
$\mathbf{x}$	State Vector.
$\mathbf{x_d}$	Desired State Vector.
x'_i	Optimal Sampling Location for Single Output.
x_n	Input for Single Data Point in Data Set.
Y	Sway Force.
Y_s	Surrogate Model Sway Force.
Y'	Sway Force Coefficient.
Y'_s	Surrogate Model Sway Force Coefficient.
y	y Cartesian Coordinate.
$\mathbf{y}$	Outputs in Data Set.
$y(\mathbf{X}_*)$	Surrogate Predicted Mean.
y^*	Output for Optimal Sampling Location.
y^+	Non-dimensional Wall Distance.

y_n	Output for Single Data Point in Data Set.
Z	Heave Force.
z	z Cartesian Coordinate.
α	Modified Waypoints Behavior Parameter.
β	Angle Between Submarine Velocity and Track-line.
γ	N_{uv} Compensation Parameter.
$\Delta\delta_{eq,N}$	Yaw Equivalent Rudder Angle Difference.
$\Delta\delta_{eq,Y}$	Sway Equivalent Rudder Angle Difference.
δ	Prandtl Turbulent Boundary Layer Thickness.
δ_r	Rudder Angles.
θ	Pitch Angle.
λ	Wavelength.
μ	Fluid Dynamic Viscosity.
$\mu(x)$	Gaussian Process Mean.
ν	Fluid Kinematic Viscosity.
ρ	Fluid Density.
σ	Surrogate Model Error.
σ_n^2	Training Data Aleatoric Uncertainty.
σ_w^2	Weighted Variance.
$\sigma_{y,i}^2$	Measured Variance for Each Set of Output Data.
τ	Fluid Stress Tensor.
$\tau_{X_{Prop}}$	Change in Propeller Thrust.
τ_{δ_r}	Change in Rudder Angle.
ϕ	Roll Angle.
ψ	Heading Angle or Yaw Angle.
ψ_d	Desired Heading Angle.
$\psi_{d,comp}$	N_{uv} Compensated Desired Heading Angle.
ω	Wave Angular Frequency.
$\%X_{prop}$	Percent of Propulsive Force.

Chapter 1

Introduction

1.1 Motivation

While the United States Navy (USN) has developed a strong arsenal of tools to model the hydrodynamic forces and moments of different vehicles in different conditions, they do not have a means of performing real-time modeling of the forces and moments that an Unmanned Underwater Vehicle (UUV) experiences when in close proximity to a moving submarine as a result of the interactions between their wakes and flow fields. One goal of this thesis is to develop a method of modeling the hydrodynamic interaction forces and moments between these two submerged moving bodies in order to incorporate these forces and moments into a UUV maneuvering simulator. The real-time modeling of these forces and moments at various positions, angles, speeds, and vehicle sizes is vital to simulate the motion of the two submerged bodies in close proximity. This thesis provides a method to create a reduced order surrogate model of these hydrodynamic interaction forces and moments, which enables the simulation of a UUV maneuvering in close proximity to a submarine. This further enables the development of safe operating envelopes and new autonomous behaviors that allow the UUV to overcome these unwanted hydrodynamic interactions.

In 2000, the USN released its Unmanned Undersea Vehicle Master Plan and provided updates in 2004 and 2011. This plan stressed the importance of UUVs and their capability to continually demonstrate new possibilities that can assist our naval forces in maintaining maritime superiority around the world [1]. UUVs are a broad category of vehicles that include both Remotely Operated Vehicles (ROVs) and Autonomous Underwater Vehicles (AUVs). Because of the limited use cases of ROVs, UUVs are often simply referred to as AUVs. UUVs are being incorporated into the fleet because they have potential capability in nine different mission areas (or UUV "Sub-Pillars") including Intelligence, Surveillance, and Reconnaissance (ISR), Mine Countermeasures (MCM), Anti-Submarine Warfare (ASW), Inspection/Identification (ID), Oceanography, Communication/Navigation Network Nodes (CN3), Payload Delivery, Information Operations (IO), and Time Critical Strike (TCS) [1].

Due to their ability to avoid detection, submarines provide an opportune platform for the launch and recovery (L&R) of UUVs. Because of their large draft and non-expendable nature, submarines cannot operate in littoral waters near an enemy coastline as well as UUVs. By integrating submarines and UUVs, the UUVs can take on certain mission sets of submarines and act as force multipliers and risk reducers to manned platforms, especially in littoral waters [1]. The expertise of the submarine crew involving underwater and covert operations is valuable to the deployment of UUVs. Submarine operational time is in high demand and enabling UUVs to accomplish certain submarine tasks will provide the submarine with flexibility and time to perform other tasks or mission sets [1]. In order to integrate submarines and UUVs, many different L&R systems have been explored to provide this new capability.

UUVs are available in four different classes. These classes are outlined in the UUV Master Plan and further expanded upon by the Unmanned Maritime Systems Program Office (PMS 406) [1, 2]. Table 1.1 describes the different features of these different UUV classes.

Table 1.1: UUV classification based on vehicle size [1, 2].

UUV Master Plan Class	PMS 406 Class	Diameter (in)	Weight (lbs)
Man-Portable	Small	3 to 10	25 to 100
Light Weight Vehicle (LWV)	Medium	10 to 12.75	∼500
Heavy Weight Vehicle (HWV)	Medium	12.75 to 21	∼3000
Large	Large	21 to 84	∼20,000
N/A	Extra Large	>84	N/A

Different classes of UUV are capable of performing different mission sets. Allowing submarines to perform L&R operations for different size UUVs enables them to accomplish a wider variety of mission sets. Table 1.2 illustrates the potential mission sets that each UUV class is capable of performing. These missions are prioritized based on importance to the USN.

Table 1.2: Different missions of different size UUVs [1].

Mission	Priority	Man-Portable	LWV	HWV	Large
ISR	1	Special Purpose	Harbor	Tactical	Persistent
MCM	2	(Very) Shallow Water, Search, Classify, Map, Neutralizers	Operating Area Clearance	Clandestine Reconnaissance	-
ASW	3	-	-	-	Hold-at-Risk
Inspection / ID	4	Homeland Defense/Anti-Terrorism Force Protection	-	-	-
Oceanography	5	-	Special Purpose	Littoral Access	Long Range
CN3	6	Very Shallow Water/Special Operations Forces	Mobile CN3	-	-

Payload Delivery	7	-	-	-	Special Operations Forces, ASW, MCM, TCS
IO	8	-	Network Attack	Submarine Decoy	-
TCS	9	-	-	-	Deliver Ordinance

Table 1.2 illustrates how there is a very high priority for all different sizes of UUVs to be able to be incorporated into the submarine fleet. These different size UUVs will act as force multipliers by taking on tasks that the high-value submarine asset would have to perform. If UUVs can be successfully integrated into the submarine fleet, submarines will be able to accomplish many more tasks by outsourcing them to the different size UUVs. Because UUVs are a very small fraction of the cost of the high-value submarine, this provides major cost saving advantages for the completion of a specified task. Additionally, UUVs operate as risk reducers. Placing a high value submarine asset in a dangerous situation, like operating in very shallow waters or close to obstacles, is very risky. However, placing an inexpensive UUV in the same scenario reduces the risk of losing a high value asset or the personnel on the submarine. Therefore, UUVs provide a means of transferring the risk to an expendable vehicle, which reduces the overall risk of a mission.

To successfully launch and recover UUVs from submarines, these two vehicles will be operating in very close proximity to each other. The flow around the submarine and UUV in close proximity will be different than if the two vehicles are far apart. The wake, pressure field, and boundary layer created by the submarine will interact with the UUV as illustrated in the figure below.

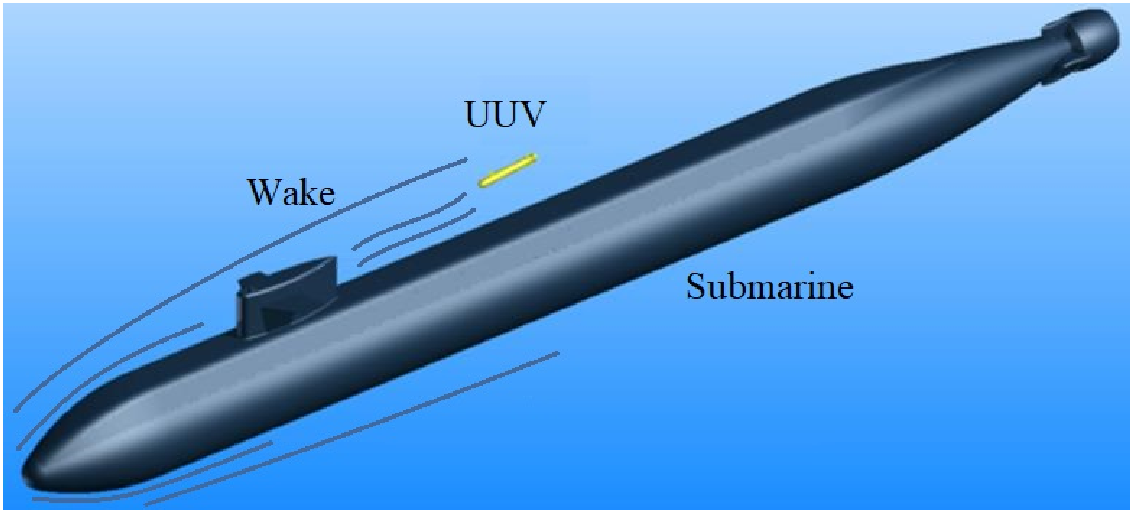

Figure 1-1: Demonstration of the impact the submarine has on flow. As a UUV operates in close proximity to the submarine, this wake and flow field influences the operation of the UUV [3].

The interactions between the submarine and UUV create forces and moments which may result in uncontrollable vehicle motions and create a challenge for the precise vehicle control required for the L&R of UUVs [4]. Because the UUV is much smaller than the submarine, the UUV is affected much more by these unwanted hydrodynamic interaction forces and moments. Understanding the hydrodynamic interactions between these two vehicles enables the Navy to better simulate UUV L&R approaches, develop better UUV autonomy and control systems, and provide additional insight when designing different UUV L&R architectures. Many different UUV L&R systems have been explored throughout the literature. Each technique has its advantages and disadvantages. Some of these most popular system concepts include L&R via [3, 4, 5, 6]:

- Enlarged Torpedo Tubes
- Existing Missile Tubes
- Dry Casing Mounted Hanger
- Wet Casing Mounted Hangar

- AUV Bespoke Multiple Hangars
- Docking Envelopes
- Mechanically Actuated Submarine

These many different potential L&R systems each require the UUV to be in a unique position. Understanding the hydrodynamic interactions of the UUV in any location with respect to the submarine is very valuable because it allows decision makers to assess the feasibility and risk of each L&R system.

1.2 Hydrodynamics

While the hydrodynamic forces acting on a single moving submarine or UUV are well known, modeling the effects of the forces and moments due to the hydrodynamic interactions between a submarine and UUV operating in close proximity is an open area of research. As a UUV travels close to a moving submarine, the pressure field and wake around the submarine cause the UUV to experience unwanted external forces and moments which make the UUV have undesirable motions and may even cause the UUV to become uncontrollable [3]. This could result in L&R failure or even a collision between the two vessels. These external forces and moments acting on the vessels operating in close proximity are known as hydrodynamic interactions.

In order to better enable L&R of UUVs from submarines, one objective of this research is to determine the hydrodynamic interaction forces and moments in real time to enable the simulation of a UUV maneuvering in close proximity to a submarine. UUV control and autonomy systems respond to perturbations from unknown external disturbances in fractions of a second in order to stay on course. This means that the hydrodynamic interaction forces and moments need to be determined in real time in order to be used to simulate their impact on UUV maneuvering.

Many methods have been developed to predict the hydrodynamic forces acting on an object. There are many means by which the hydrodynamic interactions may be predicted, each with its own advantages and disadvantages. These methods include experimental fluid dynamics (EFD) using tow tanks, empirical or semi-empirical parametric models fit to validated data, potential flow modeling using simplified physics, and computational fluid dynamics (CFD) approaches to solve the Navier-Stokes equations.

1.2.1 Experimental Fluid Dynamics

One potential approach to determine the hydrodynamic interactions is to use experimental fluid dynamics to determine the forces and moments of a UUV interacting with a moving submarine. Because this approach collects force data from physical models, usually in a tow tank, the results are generally considered valid. They often eliminate errors in computational models that exist from not capturing the real complexity of the physical world [7]. However, performing physical experiments is both challenging and expensive. In order to experimentally determine the forces and moments experienced by the UUV near a submarine, the methods used on surface ships need to be upgraded to capture the six degree-of-freedom (DOF) motion capability of submerged vehicles [4, 8]. When the effects on multiple vehicles are being studied, the required instrumentation and infrastructure increases significantly. Additionally, the facilities required to capture the range of variables studied in this research create a large obstacle. In order to have the experimental model be unaffected by the restricted water effect, the model needs to be small enough to fit in a tow tank and allow water to flow around it without having changes in the pressure and velocity field around the hull due to the tow tank walls and bottom [9, 10, 11]. However, the model needs to be as large as possible to better capture the full-scale physics and reduce EFD uncertainty. For straight-line tests, the ratio of the model length to tank width ratio should be about 0.47 [11]. Arguments have been made this is too large for submerged vehicles due to the proximity to the bottom of the tank, but this number is used to illustrate the problem [9]. Models can be slightly bigger, but corrections need to be made and errors can be introduced due to blockage effects [10]. According to this model length to tank width ratio, a 2.43 meter (8 foot) wide tow tank should have a model roughly

1.15 meters long. If the submarine being modeled is an Ohio class submarine and the UUV being modeled is a 3-inch man-portable UUV, then the submarine model would need to be about 8.6 cm in diameter. To maintain the same diameter ratio between the submarine and UUV of 168, the UUV model would need to be about 0.5 mm in diameter [12]. Collecting any usable data with a UUV model this small is completely unrealistic. Even if a medium or large UUV is modeled, rather than a man-portable UUV, this would still require the model diameters to be 3.6 mm and 14 mm respectively. These represent submarine-to-UUV diameter ratios of 24 and 6 respectively. These ratios produce model sizes that are too small to produce any useful data. In a novel study that performed EFD to validate CFD studies of the hydrodynamic interactions between submarines and UUVs, the diameter ratio between submarine and UUV is limited to 2.239 due to the previously discussed limitations on the model sizes with respect to the size of the tow tank facility [3]. Even at this extreme diameter ratio, blockage effects are still experienced in the EFD results. This is why two tank facilities often drastically limit the range of hydrodynamic interactions that can be studied based on submarine and UUV sizes.

1.2.2 Parametric Models

Several empirical parametric models have been made in an attempt to predict the hydrodynamic interactions between a submarine and UUV. Many different methods have been used to create these parametric models. One study approaches this problem by creating a partially-fixed parametric model of the hydrodynamic interaction forces and moments based on both potential theory and experimentally derived models available in the literature [13]. Much of the data is taken from the better-known interactions between surface ships and applied to submarines and UUVs. Because the model is partially created from experimental models and validated against other data within these models, it is considered accurate for its intended use. However, due to the very limited nature of the available experimental models, including only modeling very large-sized UUV at zero-degree heading angles, the results are limited to specific scenarios. The model does not have the broad level applicability to create maneuvering simulations of interest to the Navy.

Another study modeled Phoenix Autonomous Underwater Vehicle (AUV) docking into a retractable recovery tube on a Los Angeles submarine [5]. This study assumes that the submarine is large enough with respect to the UUV to appear as a flat plate. The approach determines the parabolically shaped boundary layer along the submarine hull using Prandtl's boundary layer theory over a flat plate. Within this boundary layer, the UUV experiences a reduction in fluid velocity caused by the viscous effects of the fluid acting on the hull. While this study is one of the first to model the UUV maneuverability near a moving submarine through real-time flow disturbances from the submarine, the simplicity of the method fails to capture the complexity needed to more accurately predict the behavior of the UUV. For example, this approach assumes perturbations in the flow field caused by the AUV itself are negligible. This is sometimes called the "one-way" assumption because the submarine disturbs the flow field but not the AUV. This "one-way" assumption presents significant errors when the AUV is close enough to the UUV that its own hull causes blockage effects of the flow between the vehicles. This approach also fails to account for areas near the bow and stern of the submarine where hull curvature exists.

1.2.3 Potential Flow

Potential flow is an approach that simplifies the governing fluid equations by assuming that the fluid is incompressible, inviscid, and irrotational. These simplifications enable solving the governing equations in real-time. However, neglecting fluid viscosity results in no viscous drag or flow separation along the UUVs. This results in the prediction of zero drag for a UUV moving at a constant speed through a fluid. This result is obviously incorrect and this contradiction is known as the d'Alembert paradox [14, 15]. While this approach has known limitations, there is still useful information that can be gathered by studying the hydrodynamic interactions between two vehicles using potential flow.

One study examined using potential flow methods to solve real-time hydrodynamic interactions between a surface ship and a tug boat for the use in ship maneuvering simulators. Some of the limitations of the potential flow methods are able to be overcoming using build-in parametric models that predict viscous drag on the tug. However, the study found that the potential flow solver is limited in its ability to predict real-time hydrodynamic interactions within ship handling simulators because it fails to produce accurate results when the vehicle is at non-zero heading angles [16].

1.2.4 Computational Fluid Dynamics

Computational Fluid Dynamics is a method of simultaneously solving the Navier-Stokes and continuity equations in order to fully resolve fluid flow and predict hydrodynamic forces. Analytical solutions to the Navier-Stokes equations are very limited. In certain geometries and applications, this set of coupled non-linear partial differential equations can be simplified and used to get exact solutions. However, a general smooth solution to the three-dimensional incompressible Navier-Stokes equations does not exist and remains one of the seven most important open problems in mathematics [17]. The geometry of this specific problem is too complicated to reach an analytical solution to the Navier-Stokes equations so CFD provides a good approach to numerically solving or approximating a solution to these governing equations.

The Navier-Stokes and continuity equations can be directly numerically solved using an approach called a direct numerical solution (DNS). However, in order to fully resolve the smallest scale eddies that arise due to turbulence, the resolution of the solution space has to be so fine that even supercomputers are only able to solve very simple geometries. For this reason, DNS is a good research tool for validating solutions, but not good as a means to solve the Navier-Stokes equations for engineering problems and exploring design spaces [18]. To overcome this limitation, several turbulence models have been developed which produce approximate solutions much faster than DNS methods. However, even using these turbulence models, simulations still often take hours or days to complete.

One study uses CFD to investigate the hydrodynamic interactions of a UUV at various positions relative to the sail of a moving submarine in order to determine which locations would allow for the best L&R of a UUV [19]. The study found that in the forward region of the submarine, the hydrodynamic interactions cause the UUV to be repelled and the magnitude of the force increased as the vehicles moved closer together. When the UUV is parallel and adjacent to the sail or cylindrical body, the UUV experiences attraction forces between the two vessels. This is caused by the Bernoulli effect of the flow velocity increase between the submarine and UUV. The study also found that vortices are generated by the sail and cause fluctuations in the hydrodynamic forces. Since the scope of the study is narrow in the locations and vessel diameters that it investigated, these results would need to be greatly expanded to develop usable force maps. This study also does not solve the problem of computing the hydrodynamic interactions in real time.

A pioneering study initiated and partially funded by the Defense, Science and Technology Organization (DSTO) and the National Centre for Maritime Engineering and Hydrodynamics (NCMEH) at the Australian Maritime College (AMC) was able to make great progress exploring the hydrodynamic interactions between a UUV and submarine [3]. The investigation examined hydrodynamic interactions of an unappended UUV based on the relative speed, longitudinal position, lateral position, and size difference with respect to an unappended submarine. The work involved the development of CFD models to simulate the hydrodynamic interactions and map the resulting forces and moments. This study also conducted tow tank experiments with two submerged bodies and used the results to validate its computational models. While this examination is much more extensive than previous studies, different length-to-diameter ratios and different heading angles need to be further examined to fully understand the effects of the hydrodynamic interactions to enable the simulation of the maneuvering UUV in close proximity to the submarine.

While each of these approaches has its own advantages and disadvantages, none of them is capable of accurately solving the hydrodynamic interactions between a submarine and UUV in real time. Without real-time modeling of the hydrodynamic interactions, these forces and moments cannot be incorporated into UUV maneuvering simulators to determine the impact of the hydrodynamic interactions. As such, this research takes a new approach using machine learning to bridge this gap by developing a surrogate model trained on accurate CFD data capable of computing the hydrodynamic interactions in real time. This surrogate model may be incorporated into UUV maneuvering simulators in order to determine the impact of the hydrodynamic interactions and develop strategies to overcome them.

1.3 Machine Learning

In order to simulate the complex and diverse maneuverability space of a UUV in close proximity to a submarine, the forces and moments due to their hydrodynamic interactions need to be known at various positions, orientations, velocities, submarine to UUV diameter ratios, and UUV length to diameter ratios. Changing one of these variables results in different hydrodynamic interaction forces and moments experienced by the UUV. As such, the real-time determination of the hydrodynamic interactions based on these variables is essential to simulate UUV autonomy and maneuvering when operating near a moving submarine. Because traditional hydrodynamic techniques are not capable of being solved in real time, machine learning provides a possible means of creating a surrogate model capable of solving the hydrodynamic interactions in real time. Training this surrogate model on data gathered from traditional validated hydrodynamics techniques enables the surrogate to capture the accuracy of the underlying technique while drastically reducing the computational cost to predict the hydrodynamic interaction forces and moments for any UUV state.

Machine learning is a vast area of study that explores many different problems or applications. This particular problem of mapping desired outputs to their inputs based on data provided by a supervisor is a type of supervised machine learning known as regression. Supervised machine learning is when the output data is known and provided by a supervisor. In this case, the known outputs, which are the hydrodynamic interactions, are provided using traditional hydrodynamic techniques. Regression is a process for mapping and predicting the output based on the model inputs.

There are many supervised machine learning regression methods that are potential candidates for this study. A few popular regression techniques include linear and non-linear regression, neural networks, neural operators, and Gaussian Process (GP) regression. Each of these approaches has its advantages and disadvantages. Linear regression is easy to implement but is unable to accurately predict non-linear outputs. Non-linear regression is also relatively easy to implement, but the output is modeled as a function of the input using basis functions. This is useful if the shape of the output is known so that the basis functions can be selected to accurately map the output. When mapping the hydrodynamic interaction forces and moments to the state of the UUV around the submarine, the shape of the output function is unknown. This makes using linear and non-linear regression unrealistic.

Neural networks are capable of mapping outputs with a non-linear and unknown shape. However, these techniques often employ several hidden layers of a large number of neurons combined with activation functions in order to create non-linear outputs. Because of this multi-layer and multi-neuron architecture, these approaches often take a large amount of training data in order to determine all of the weights and become accurate. Neural operators employ similar multi-layer strategies of operators, which also requires large amounts of training data. Because of the high computational or experimental cost to determine the hydrodynamic interactions of a single UUV at one state, these approaches are unlikely to be successful without generating training data beyond the resources of this research.

However, GP regression is a prime candidate to map the hydrodynamic interactions to the state of the UUV. GP regression can be used to simulate a Bayesian linear regression model with an infinite number of basis functions [20]. Because an infinite number of these basis functions can determine the form of any sufficiently smooth output function, this method is well suited for this study with an unknown shape for the output functions. Additionally, because GP regression uses a kernel rather than a large number of neurons and layers, this approach often requires a smaller amount of training data than other machine learning regression methods to accurately map inputs to outputs [20]. GP regression also has inherently robust uncertainty quantification that is useful in assessing the accuracy of the surrogate model.

There is a wide range of UUV states for which the hydrodynamic interactions can be determined. Because determining the hydrodynamic interactions at a specific UUV state is expensive, the UUV state should be selected to ensure that the data provides the most benefit to the machine learning surrogate model. Carefully selecting which experiments to run in order to extract the largest amount of information is known as the Design of Experiments (DOE). This field of study originated in agriculture and deals with planning, conducting, and analyzing the input and output variables of an experiment [21]. DOE is conducted before an experiment is performed to determine how to best use the valuable experimental resources. This practice reduces the number of experiments needed to create a statistically valid model. Optimal experimental design (OED) is performed by selecting the most efficient set of experiments needed to accurately estimate the output.

In the OED field, the practice of performing an experiment for every possible combination of discrete input variables is called a full factorial design [21, 22]. This method provides the most comprehensive exploration of the design space but is often way too resource intensive to be considered feasible, as is the case with this research. There are many approaches to reduce the number of experiments needed to adequately explore the design space, but they are generally narrowed into two categories: fractional factorial design and sequential design [22]. The fractional factorial design establishes the full set of experiments that will be performed before any single experiment is performed or results are obtained. This approach is well suited to map a function within a given range of input variables and is a good method to comprehensively explore a design space. However, a disadvantage of the fractional factorial design is that it may spend resources exploring regions of the design space that may be of no interest or well modeled. Eliminating unimportant areas of the design space and adjusting the design to focus on areas that better improve the surrogate provides a more efficient means of conducting the experiments. This sequential design type of OED is often referred to as active learning in the machine learning field [23, 24, 25].

1.3.1 Active Learning

For many problems, like the one considered for modeling the UUV hydrodynamic interactions, the cost of obtaining accurate training data is very large. Active learning consults the surrogate after every experiment is performed to try to find the next new experiment that provides the most benefit. In order to use active learning, the surrogate model is retrained after every new experiment is conducted. This enables the surrogate to update after every experiment and identify the next optimal experiment to run. The next optimal experiment is found using an equation known as an acquisition function [23, 24].

There are many known acquisition functions that depend on the quantity of interest [25, 26]. While many of these acquisition functions apply to this research, there is no specific acquisition function that is well-suited to combine the available different hydrodynamic methods for multiple forces and moments. One goal of this research is to explore various means of utilizing all available hydrodynamic resources to provide an acquisition function capable of producing an accurate and low-cost surrogate model.

1.4 Thesis Objective

In order to enable the launch and recovery of UUVs from submarines, a UUV needs to be able to overcome the hydrodynamic interaction forces and moments between the two vehicles [3]. Because of its accuracy and ease of implementation, CFD is often used to predict these hydrodynamic interactions. While most CFD simulations take hours to days to complete, a UUV control system provides updates multiple times a second to its desired speed and heading based on its current state in order to maintain the desired trajectory. As such, the hydrodynamic interaction forces and moments need to be determined in real time in order to accurately simulate UUV maneuvering around a moving submarine. This thesis intends to bridge this technological gap by creating a surrogate with the accuracy of CFD and the necessary speed to be solved in real time. This surrogate can be used to simulate UUV maneuvering around the submarine as well as develop new autonomous behaviors capable of overcoming these unwanted hydrodynamic interactions.

1.4.1 Thesis Problem Statement

To develop a methodology for simulating UUV maneuvering around a moving submarine by accurately predicting the complex hydrodynamic interactions in real time using novel active sampling machine learning approaches as a surrogate model.

1.4.2 List of Contributions

Provided is a list of the contributions made by this thesis to overcome the technical gap summarized in the thesis problem statement.

- A generalizable method of actively sampling data points across multi-fidelity GP regression framework using a new Non-Myopic Multi-Fidelity active learning algorithm. This includes a new method of acquiring optimal sampling locations between multi-fidelity frameworks. This approach includes the formulation of the inter-model acquisition function and is capable of being used in a variety of other applications. This method has been submitted for publication.
- A methodology of implementing a surrogate model into a UUV motion simulator in order to study the impact of the hydrodynamic interactions on UUV motion. This method has been submitted for publication. This includes:
    - Methodology for the development of a surrogate model capable of predict-

  ing the hydrodynamic interactions between a UUV and a submarine in real time.

  - Methodology for integrating the surrogate model into the UUV equations of motion.

  - Development of force and moment maps using the surrogate model to better quantify the unwanted hydrodynamic interactions.

  - Development of operating envelopes that outline regions where the UUV safely overcomes the hydrodynamic interactions and where the UUV is overpowered and collides with the submarine.

- A methodology of implementing a surrogate model into a UUV autonomy architecture in order to develop new autonomous behaviors capable of overcoming unwanted hydrodynamic interactions. This method has been submitted for publication. This includes:

  - Method for integrating the surrogate model into the autonomy architecture of the UUV.

  - Method for adjusting the UUV heading to account for the moving submarine reference frame. This is known as the modified waypoints behavior.

  - Method for adjusting the UUV heading to account for the yaw moment hydrodynamic interaction. This is known as the N_{uv} compensating behavior.

1.5 Thesis Outline

This thesis chapter introduces the motivation, problem, and approach to bridge the technological gap using a methodology of implementing a surrogate model into a UUV motion simulator in order to study the impact of the hydrodynamic interactions on UUV motion.

The remaining chapters are outlined below:

Chapter 2: Non-Myopic Multi-Fidelity Active Learning

Describes the new active learning method that utilizes the low cost of the low fidelity potential flow model to explore the design space while leveraging the high accuracy of the high fidelity CFD simulator to create a surrogate model. This also includes the method of active learning that accounts for multiple outputs.

Chapter 3: Computational Modeling of Multiple Body Hydrodynamic Interactions

Outlines the methods and procedures of implementing potential flow and CFD simulators to predict the hydrodynamic interactions. This includes validation of these methods against tow tank experiments.

Chapter 4: Reduced Order Modeling of Hydrodynamic Interactions between a UUV and Submarine

Describes the approach of designing and developing the hydrodynamic interaction surrogate model. The surrogate is validated real-world results.

Chapter 5: Simulating UUV Motion with Hydrodynamic Interactions

Details the method of incorporating the hydrodynamic interaction surrogate model into the equations of motion of the UUV maneuvering simulator. The UUV simulator is validated and safe operating envelopes are developed for various scenarios.

Chapter 6: Developing Autonomous Behaviors to Overcome Hydrodynamic Interactions

Describes the method of incorporating the hydrodynamic interaction surrogate model into the autonomous behavior architecture of the UUV simulator. This method is used to develop new autonomous behaviors better capable of overcoming these unwanted hydrodynamic interactions.

Chapter 7: Conclusion

Summarizes the thesis and research contributions as well as provides suggestions for future work.

Chapter 2

Non-Myopic Multi-Fidelity Active Learning

2.1 Introduction

In order to enable the launch and recovery of UUVs from submarines, a UUV needs to be able to overcome the hydrodynamic interaction forces and moments between the two vehicles [3]. These hydrodynamic interactions are often predicted using high fidelity CFD modeling due to its high accuracy. While most CFD simulations take hours to days to complete, a UUV control system needs to respond to perturbations and changes to the vehicle position and heading within fractions of a second in order to maintain the desired trajectory. As such, the UUV needs to determine the hydrodynamic interaction forces and moments in real time based on its position, heading, speed, and proximity to its desired path.

Modeling forces and moments on a UUV can be performed with a variety of computational models that resolve the governing fluid equations. These range from low fidelity and low cost models to more expensive and more accurate models. Specifically, low fidelity models, such as potential flow solvers use simplified physics which neglects viscosity, skin friction, boundary layer development, and flow separation.

This simplified approach leads to the d'Alembert paradox, which infamously predicts zero drag on a UUV moving at constant velocity and suggests that the body will perpetually move forward [14, 15]. These low fidelity solvers are often improved and supplemented with simple parametric models to help overcome these weaknesses. They also often have the capability to be solved in real time [27]. However, due to these shortcomings, potential flow solvers ultimately lack the accuracy needed to model the complex real world hydrodynamic interactions to enable UUV launch and recovery operations. This can be achieved by CFD solvers that rigorously model all the important fluid dynamics phenomena, but they have significant computational cost. Because the required accuracy of the CFD is not capable of being delivered in real time, a surrogate model is needed that is capable of being implemented in real time and has the accuracy of the CFD.

A typical approach for building a surrogate model is to collect high fidelity data from expensive and highly accurate CFD solvers and apply reduced order modeling ideas. However, the computational cost of CFD can be prohibitive, given that the parameter space for a UUV is significantly large. For such a case, an alternative is to combine a few, carefully selected high fidelity simulations from a CFD model with plenty of low fidelity computations from a potential flow solver. Integrating various fidelity models into one surrogate is known as multi-fidelity modeling [28, 29]. By leveraging data from a lower cost and less accurate model with data from a high fidelity model, the accuracy of the surrogate model can be improved without the need for an excessive number of high fidelity simulations. This results in a significant reduction of the computational cost of the surrogate model without sacrificing accuracy.

An important question for developing accurate surrogate models is the selection of the most informative training data, i.e. what CFD simulations one should perform to get the most important information. This can be achieved by employing active learning, a type of machine learning data sampling method in which the algorithm is able to determine the optimal set of input parameters for which the next simulation should be performed [23, 24, 25]. Typical active learning algorithms are characterized by myopia, or nearsightedness, which is a condition in which the lack of foresight can inhibit the ability of a sampling algorithm to select the optimal sampling location for the surrogate model [26, 30]. For example, a game exists where an unknown random number is selected between 0 and 100. The object of the game is to minimize the value between a number chosen by the participant and the unknown random number. In this instance, the optimal number to select would be 50, halfway between the two endpoints. This ensures that the maximum error between any random number and the selected value is 50. Now assume the participant is allowed to select a second number. Once 50 is selected, the next optimal value would be either 25 or 75. However, neither of these two options reduces the maximum error because there is still the potential to be off by 50. This problem exists because of myopia. Originally, the participant is only considering selecting one single number. If the selection method is non-myopic, there are different optimal values chosen. By knowing beforehand that two selections would be made, the optimal selections would be at 25 and 75. By selecting these two points, the maximum value between any random number and one of the selected values would be 25. This illustrates how having the foresight of knowing about future sampling characteristics provides a different set of optimal sampling locations.

This thesis introduces the use of a non-myopic multi-fidelity (NMMF) active learning Gaussian Process (GP) regression algorithm for reduced order modeling and compares it with standard myopic active learning techniques. A review of Gaussian process regression, multi-fidelity modeling, and active learning in a myopic and non-myopic setup is outlined. The formulation and implementation of the NMMF method is detailed, including the its relative advantages in the context of standard benchmark functions and prototype problems for scalar and vector outputs. The performance of the NMMF active learning algorithm is also examined in the context of reduced order modeling for UUV and submarine hydrodynamic interactions.

2.2 Background

2.2.1 Gaussian Process Regression

The purpose of GP regression is to develop a surrogate or reduced order model (ROM) that is capable of predicting the value of dependent variables based on the input of independent variables. However, in contrast to typical regression methods, GP provides rigorous estimates for the epistemic uncertainty of the derived model, i.e. errors due to lack of data. The GP regression model can be expressed as a random function,

$$y = f(x) + \epsilon \tag{2.1}$$

where $x \in \mathbb{R}^d$, $\epsilon \sim \mathcal{N}(0, \sigma^2)$ represents the noise of the model. The random function f follows a Gaussian distribution with prescribed mean and covariance function such that [20]:

$$f(x) \sim \mathcal{GP}(\mu(x), k(x, x')), \tag{2.2}$$

where $\mu(x)$ is the mean and $k(x, x')$ the covariance as shown in the following equations.

$$\mu(x) = \mathbb{E}[f(x)] \tag{2.3}$$

$$k(x, x') = \mathbb{E}[(f(x) - \mu(x))(f(x') - \mu(x'))] \tag{2.4}$$

There are many different covariance functions (or kernels) that are often used in GP models. Some of the more popular kernels include the white noise kernel, squared exponential kernel, rational quadratic kernel, and the periodic kernel [31]. Rather than explore the impact of these different kernels, this thesis uses the following popular radial basis function (RBF) kernel with automatic relevance determination:

$$k(x, x') = \exp\left(\frac{-(x - x')^T \lambda^{-1}(x - x')}{2}\right) \tag{2.5}$$

where λ is the diagonal matrix containing the length scales of each input dimension. This kernel is selected because it simulates a Bayesian linear regression model with an infinite number of basis functions. In other words, this kernel can be formed from a linear combination of an infinite number of Gaussian-shaped basis functions [20]. Because an infinite number of these basis functions can determine the form of any sufficiently smooth output function, this method is well suited for this study with an unknown form for the different output functions. Automatic relevance determination is used because it enables the GP regression kernel to have different length scales for each input dimension.

GP regression is ultimately used to calculate the predicted mean $y(\mathbf{X}_*)$ and covariance $K_{yy}(\mathbf{X}_*, \mathbf{X}'_*)$ from a set of input-output data pairs. In particular, the model is trained with a data set $\mathcal{D}$ =$\{x_i, y_i\}_{i=1}^n$, where n is the number of samples. This data set $\mathcal{D}$ is also categorized into inputs and outputs denoted as $\mathbf{X} = [x_1, ..., x_n] \in \mathbb{R}^{d \times n}$ and $\mathbf{y} = [y_1, ..., y_n] \in \mathbb{R}^n$ where the d represents the dimension of the input domain. Likewise, $\mathbf{X}_* = [x_{*1}, ..., x_{*m}] \in \mathbb{R}^{d \times m}$, is a set of m locations within the $d-$dimension domain for which a prediction is desired. Equations (2.6) and (2.7) determine the predicted mean and covariance at a set of points $\mathbf{X}_*$ [20]:

$$y(\mathbf{X}_*) = K(\mathbf{X}_*, \mathbf{X})[K(\mathbf{X}, \mathbf{X}) + \sigma_n^2 \mathbf{I}]^{-1}\mathbf{y} \tag{2.6}$$

$$K_{yy}(\mathbf{X}_*, \mathbf{X}'_*) = K(\mathbf{X}_*, \mathbf{X}'_*) - K(\mathbf{X}_*, \mathbf{X})[K(\mathbf{X}, \mathbf{X}) + \sigma_n^2 \mathbf{I}]^{-1} K(\mathbf{X}, \mathbf{X}'_*) \tag{2.7}$$

The term σ_n^2 represents the aleatoric uncertainty in the training samples. This is a hyperparameter that is optimized using gradient descent methods to improve the predictive capabilities of the GP regression [20]. Additionally, it helps ensure the matrix in brackets in equations (2.6) and (2.7) is well conditioned.

2.2.2 Active Learning

For many problems, like the one considered for modeling the UUV hydrodynamic interactions, the cost of obtaining accurate training data for GP regression is very large. As such, each new data point is selected sequentially and methodically, so that it provides the most improvement to the surrogate model. This type of data sampling method in which the algorithm is able to determine the optimal set of input parameters for the next sample is called active learning or optimal experimental design [23, 24].

In order to understand active learning, suppose there exists a GP regression model $y_{n-1}(x)$ with an error of $\sigma_{n-1}(x) = \sqrt{K_{yy}(x,x)}$ trained from a data set with input vectors $\{x_1, x_2, ..., x_{n-1}\}$. The goal of active learning is to use the predicted mean and error estimate, to optimize the selection of the next sample, x^*. Specifically, active learning uses what is called an acquisition function $q(x|y_{n-1}, \sigma_{n-1})$ in order to determine this next optimal sample x^*. The definition of a generic acquisition function is as follows:

$$x^* = \arg\max q(x|y_{n-1}, \sigma_{n-1}). \tag{2.8}$$

Once this optimal sampling location x^* is determined, the sample is taken at that point to determine its output y^*. The new data is then added to the existing data set $\mathcal{D}_n = \{\mathcal{D}_{n-1} \cup (x^*, y^*)\}$. The new surrogate mean $y_n(x)$ and error $\sigma_n(x)$ are determined and the process is iterated as necessary. Figure 2-1 illustrates the active sampling process.

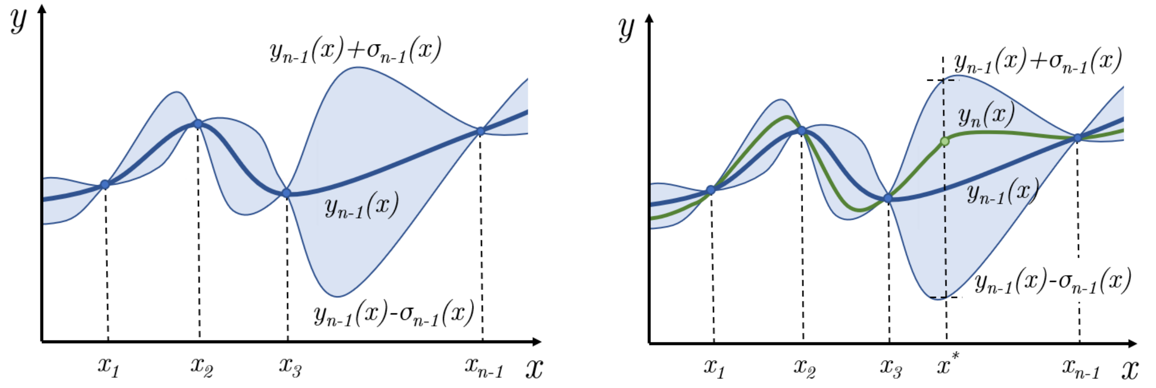

(a) Estimation of the surrogate predicted mean y_{n-1} and its error σ_{n-1}

(b) Sampling at a new optimal location x^* and estimation of new surrogate predicted mean y_n

Figure 2-1: Demonstration of active sampling method of determining the optimal sample location and updating the predicted mean of the surrogate model.

In figure 2-1, the optimal sampling location x^* is determined by locating the point in the domain with the largest model error σ_{n-1}. This popular acquisition function is known as Uncertainty Sampling (US) and is shown in equation (2.9), [25].

$$q_{US}(x) = \sigma^2(x) \tag{2.9}$$

The US acquisition function is widely used because it is intuitive, robust, broadly applicable, inexpensive to compute, and has analytical gradients, which allows the use of gradient-based optimizers so it becomes considerably more efficient than other acquisition functions [32]. There are many different acquisition functions like integrated variance reduction, input-weighted integrated variance reduction, mutual information, and likelihood-weighted acquisition functions [25]. However, for the purpose of this thesis in which non-myopic active learning is explored, only the US acquisition function is used due to its robustness.

2.2.3 Myopic versus Non-Myopic Active Learning Algorithms

Typical active learning sampling methods are myopic, meaning that they only consider a single step into the future when selecting the next optimal sampling location

[26]. Once a location is selected, the output is evaluated at that single point and this new data is added to the existing data set. In particular, when a new single location x_n is determined using active learning criteria, the output y_n is computed from a simulation or experiment, and the data set is augmented with the new information, i.e. $\mathcal{D}_n = \{\mathcal{D}_{n-1} \cup (x_n, y_n)\}$. Figure 2-2 illustrates this myopic sampling algorithm.

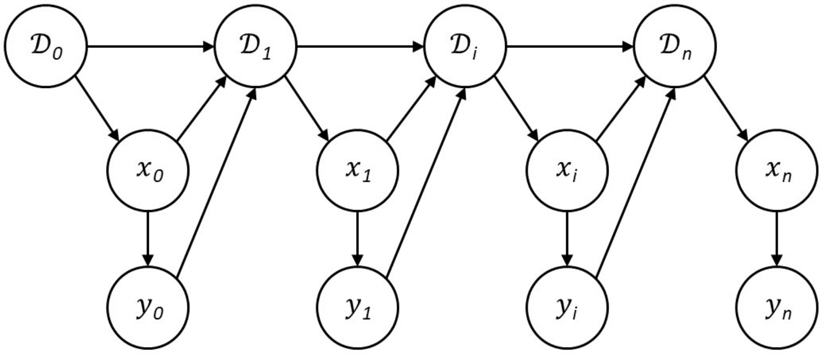

Figure 2-2: Myopic Sampling Algorithm: At every step, an active learning criterion determines a single new input x_n, for which we obtain the output y_n.

While this myopic approach is often used in practice, there are other non-myopic approaches that provide solutions to the multi-step look-ahead problem with better results than a myopic approach [26, 30]. Specifically, a non-myopic approach enables the algorithm to determine the next optimal sampling location based on the influence of several future potential sampling locations. This allows the algorithm to select the optimal sampling location with the knowledge about how the multiple future sampling locations may influence the next sample. This influence of future evaluations on current sampling locations is illustrated in figure 2-3 using a blue line.

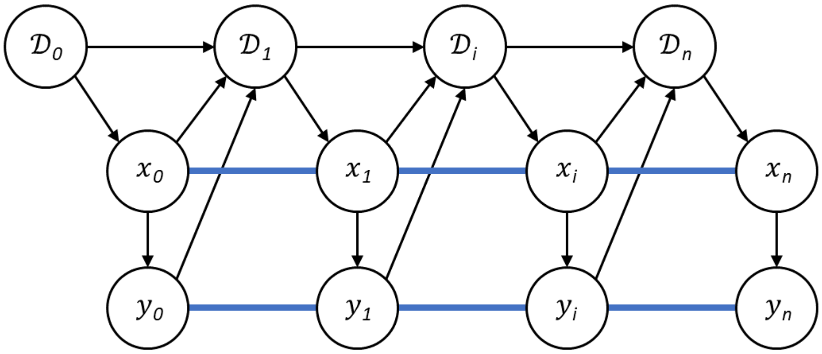

Figure 2-3: Non-Myopic Sampling Algorithm: The next sample is influenced by potential locations of future samples. This allows the method to consider the impact of future results beyond the capability of myopic sampling.

There are many different non-myopic algorithms that use various acquisition functions to evaluate the impact of future samples [26, 30, 33, 34]. These acquisition functions vary in how they evaluate and utilize the expected value of the future samples on the model. However, all of these non-myopic sampling methods are only used for single fidelity surrogate models and do not offer a means to which non-myopic methods can be expanded to operate between models of different fidelity. In this thesis, a new sampling method is explored by bridging the gap between non-myopic sampling and multi-fidelity GP modeling to achieve improvements in lowering the cost and increasing the accuracy of high fidelity simulators.

2.2.4 Multi-Fidelity Modeling

Multi-fidelity GP modeling uses multiple separate simulators or experiments to develop the surrogate model. Like in the present context of modeling UUV hydrodynamic interactions, there is a high fidelity model which is computationally expensive to use and a low fidelity model which requires much less computational effort to perform. In the context of this work, the high fidelity simulation is CFD and the low fidelity simulation is a potential flow solver. Because of the different assumptions and physics being modeled, the CFD and potential flow simulators produce different results for any given sampling location. These results are stored in a high fidelity data set denoted by $\mathcal{D}_{\mathcal{HF}} = \{\mathbf{X}_{\mathcal{HF}}, \mathbf{y}_{\mathcal{HF}}\}$ and a low fidelity data set $\mathcal{D}_{\mathcal{LF}} = \{\mathbf{X}_{\mathcal{LF}}, \mathbf{y}_{\mathcal{LF}}\}$. Kennedy and O'Hagan developed the following first-order auto-regressive co-kriging scheme for the relationship between high and low fidelity models [29].

$$f_{\mathcal{HF}}(\mathbf{X}_*) = \rho(\mathbf{X}_*) f_{\mathcal{LF}}(\mathbf{X}_*) + \delta(\mathbf{X}_*) \tag{2.10}$$

Functions $f(\mathbf{X}_*)$ and $\delta(\mathbf{X}_*)$ represent GP regression models while ρ is a scaling factor that correlates the high fidelity and low fidelity models. This scaling factor is set to one for the purposes of this thesis because there is no scaling needed between CFD and potential flow simulators. Using a multi-fidelity modeling approach provides the benefit of improving the accuracy and cost of the surrogate model by combining expensive accurate high-fidelity data with cheaper and less accurate low-fidelity data [29]. This scheme and the others can be used recursively to account for more than two levels of fidelity, but only two levels are used for this thesis. There are other schemes to account for multi-fidelity modeling besides the first-order auto-regressive co-kriging scheme. These other schemes include a deep GP in which the scaling factor is replaced with an unknown function $z(f_{\mathcal{LF}}(x))$ which maps the difference between the low and high fidelity models [35]. This function z is often another GP regression, which is why this is often called deep GP regression, but the added layer of GP regression comes at a steep computational price. Another scheme is the non-linear auto-regressive multi-fidelity GP regression scheme in which a higher dimension GP regression model is created that jointly relates the input space and the outputs of the lower fidelity level to the output of the higher fidelity model. Once again, this modification to the multi-fidelity modeling scheme increases the computational cost of the model [36].

As such, the first-order auto-regressive co-kriging scheme is used for this study due to its low cost and ease of implementation [35, 36, 29]. Equation (2.10) implies the Markov property: given $f_{\mathcal{LF}}(\mathbf{X}_*)$, nothing more can be learned about $f_{\mathcal{HF}}(\mathbf{X}_*)$ from any other model output $f_{\mathcal{LF}}(\mathbf{X}'_*)$ for $\mathbf{X}_* \neq \mathbf{X}'_*$, i.e $\text{cov}\{f_{\mathcal{HF}}(\mathbf{X}_*), f_{\mathcal{LF}}(\mathbf{X}'_*) | f_{\mathcal{LF}}(\mathbf{X}_*)\} = 0$, [29].

This allows for the following definition of the high fidelity $f_{\mathcal{HF}}(\mathbf{X}_*)$, low fidelity $f_{\mathcal{LF}}(\mathbf{X}_*)$, multi-fidelity $f_{\mathcal{MF}}(\mathbf{X}_*)$, and $\delta(\mathbf{X}_*)$ GP regression models:

$$\begin{aligned}
f_{\mathcal{HF}}(\mathbf{X}_*) &\sim \mathcal{GP}(y_{\mathcal{HF}}(\mathbf{X}_*), K_{yy,\mathcal{HF}}(\mathbf{X}_*, \mathbf{X}'_*)) \\
f_{\mathcal{LF}}(\mathbf{X}_*) &\sim \mathcal{GP}(y_{\mathcal{LF}}(\mathbf{X}_*), K_{yy,\mathcal{LF}}(\mathbf{X}_*, \mathbf{X}'_*)) \\
\delta(\mathbf{X}_*) &\sim \mathcal{GP}(y_{\delta}(\mathbf{X}_*), K_{yy,\delta}(\mathbf{X}_*, \mathbf{X}'_*)) \\
f_{\mathcal{MF}}(\mathbf{X}_*) &\sim \mathcal{GP}(y_{\mathcal{MF}}(\mathbf{X}_*), K_{yy,\mathcal{HF}}(\mathbf{X}_*, \mathbf{X}'_*)) \\
\text{where} \quad y_{\mathcal{MF}}(\mathbf{X}_*) &= y_{\mathcal{LF}}(\mathbf{X}_*) + y_{\delta}(\mathbf{X}_*) \\
\text{and} \quad K_{yy,\mathcal{MF}}(\mathbf{X}_*, \mathbf{X}'_*) = K_{yy,\mathcal{HF}}(\mathbf{X}_*, \mathbf{X}'_*) &= K_{yy,\delta}(\mathbf{X}_*, \mathbf{X}'_*)
\end{aligned} \tag{2.11}$$

By expanding equations (2.2), (2.6), (2.7), and (2.10) to account for the multi-fidelity modeling approach, the predicted mean and covariance of the low and high fidelity GP models are derived. Additionally, the $\delta(\mathbf{X}_*)$ GP regression model from equation (2.10) has a predicted mean and covariance listed in equation (2.14). In order to determine the mean of the $\delta(\mathbf{X}_*)$ GP regression model, a vector of the outputs $\mathbf{y}_\delta$ is needed. This is found by using the difference between the high fidelity and low fidelity outputs for each of the n high fidelity samples at the corresponding low fidelity sample locations as shown in equation (2.15). This requires that the samples of the high fidelity data set are a subset within the low fidelity data set, i.e $\mathbf{X}_{\mathcal{LF}} \subseteq \mathbf{X}_{\mathcal{HF}}$.

$$\begin{aligned}
y_{\mathcal{HF}}(\mathbf{X}_*) &= K(\mathbf{X}_*, \mathbf{X}_{\mathcal{HF}})[K(\mathbf{X}_{\mathcal{HF}}, \mathbf{X}_{\mathcal{HF}}) + \sigma_n^2 \mathbf{I}]^{-1} \mathbf{y}_{\mathcal{HF}} \\
K_{yy,\mathcal{HF}}(\mathbf{X}_*, \mathbf{X}'_*) &= K(\mathbf{X}_*, \mathbf{X}'_*) - K(\mathbf{X}_*, \mathbf{X}_{\mathcal{HF}})[K(\mathbf{X}_{\mathcal{HF}}, \mathbf{X}_{\mathcal{HF}}) + \sigma_n^2 \mathbf{I}]^{-1} K(\mathbf{X}_{\mathcal{HF}}, \mathbf{X}'_*) \\
\sigma_{\mathcal{HF}}(\mathbf{X}_*) &= \sqrt{K_{yy,\mathcal{HF}}(\mathbf{X}_*, \mathbf{X}_*)}
\end{aligned} \tag{2.12}$$

and

$$\begin{aligned}
y_{\mathcal{LF}}(\mathbf{X}_*) &= K(\mathbf{X}_*, \mathbf{X}_{\mathcal{LF}})[K(\mathbf{X}_{\mathcal{LF}}, \mathbf{X}_{\mathcal{LF}}) + \sigma_n^2\mathbf{I}]^{-1}\mathbf{y}_{\mathcal{LF}} \\
K_{yy,\mathcal{LF}}(\mathbf{X}_*, \mathbf{X}'_*) &= K(\mathbf{X}_*, \mathbf{X}'_*) - K(\mathbf{X}_*, \mathbf{X}_{\mathcal{LF}})[K(\mathbf{X}_{\mathcal{LF}}, \mathbf{X}_{\mathcal{LF}}) + \sigma_n^2\mathbf{I}]^{-1}K(\mathbf{X}_{\mathcal{LF}}, \mathbf{X}'_*) \\
\sigma_{\mathcal{LF}}(\mathbf{X}_*) &= \sqrt{K_{yy,\mathcal{LF}}(\mathbf{X}_*, \mathbf{X}_*)}
\end{aligned} \tag{2.13}$$

and

$$\begin{aligned}
y_{\delta}(\mathbf{X}_*) &= K(\mathbf{X}_*, \mathbf{X}_{\mathcal{HF}})[K(\mathbf{X}_{\mathcal{HF}}, \mathbf{X}_{\mathcal{HF}}) + \sigma_n^2\mathbf{I}]^{-1}\mathbf{y}_{\delta} \\
K_{yy,\delta}(\mathbf{X}_*, \mathbf{X}'_*) &= K_{yy,\mathcal{HF}}(\mathbf{X}_*, \mathbf{X}_*) \\
\sigma_{\delta}(\mathbf{X}_*) &= \sqrt{K_{yy,\delta}(\mathbf{X}_*, \mathbf{X}_*)}
\end{aligned} \tag{2.14}$$

and

$$\mathbf{y}_{\delta} = \{y_{\mathcal{HF},i} - y_{\mathcal{LF},i}\}_{i=1}^{n} \tag{2.15}$$

Equations (2.11) through (2.15) are the framework for multi-fidelity GP regression. This framework provides the grounds for which the non-myopic active sampling concept can be incorporated into a multi-fidelity GP regression scheme to improve the cost and accuracy of the surrogate model.

2.3 Non-Myopic Multi-Fidelity Active Learning

2.3.1 Inter-Model Acquisition Function

Motivated by the advantage of producing a low cost and high accuracy surrogate model using the multi-fidelity framework, as well as a non-myopic setup for active learning, the formulation of a new non-myopic multi-fidelity active learning algorithm is formalized.

Before the algorithm can be formalized, a new type of acquisition function called an inter-model acquisition function q_{IM} must be introduced. It is used to determine the next optimal location for the high fidelity simulation to be performed. This new type of acquisition function is unique because it takes into account the statistics of multiple GP regression models with differing fidelity, rather than a single fidelity GP regression model. The generic form of the inter-model acquisition function is as follows:

$$q_{IM}(\mathbf{X}_*) = f(y_{\mathcal{HF}}(\mathbf{X}_*), \sigma_{\mathcal{HF}}(\mathbf{X}_*) = \sigma_\delta(\mathbf{X}_*), y_{\mathcal{LF}}(\mathbf{X}_*), \sigma_{\mathcal{LF}}(\mathbf{X}_*), y_\delta(\mathbf{X}_*)). \tag{2.16}$$

In order to formulate an effective inter-model acquisition function, consider an example high fidelity and a multi-fidelity GP regression model. Recall from equation (2.11) that $y_{\mathcal{MF}}(\mathbf{X}_*) = y_{\mathcal{LF}}(\mathbf{X}_*) + y_\delta(\mathbf{X}_*)$ and $\sigma_{\mathcal{MF}}(\mathbf{X}_*) = \sigma_{\mathcal{HF}}(\mathbf{X}_*) = \sigma_\delta(\mathbf{X}_*)$. Figure 2-4 illustrates a high fidelity and a multi-fidelity GP regression model from equation (2.11) with three different low fidelity active samples.

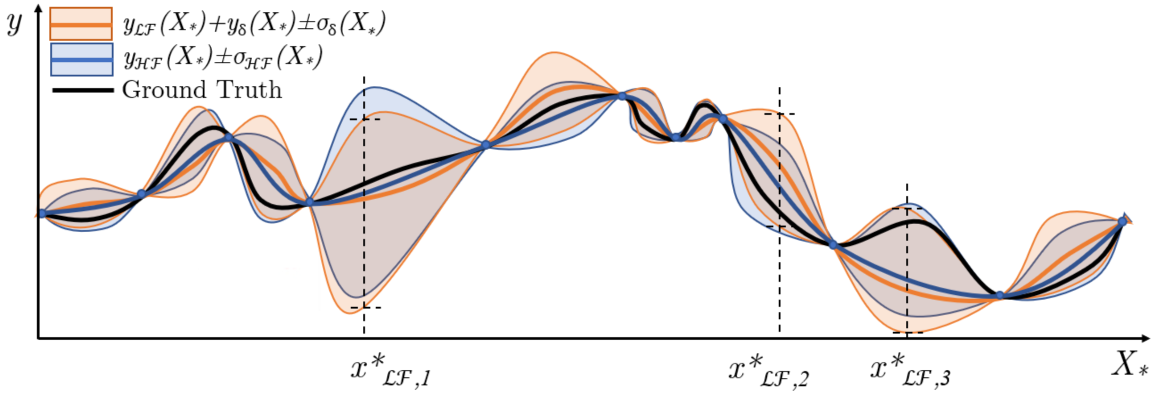

(a) Low Fidelity Active Sampling: The high (blue) and multi-fidelity (orange) GP regression models are shown with the next three low fidelity sampling locations.

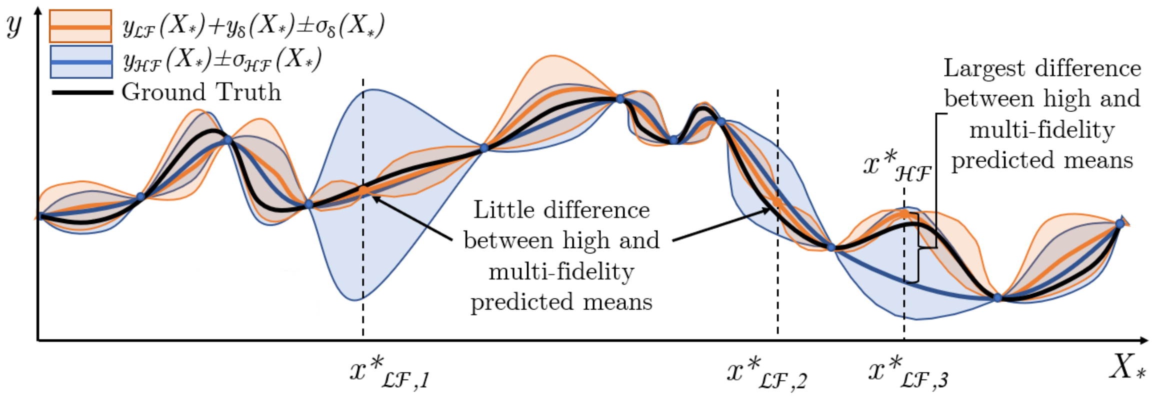

(b) Inter-Model Active Sampling: The high fidelity sampling location is determined by considering how the multi-fidelity model is impacted by the new low fidelity samples.

Figure 2-4: Inter-Model Acquisition Function: The location of the next high fidelity sample is determined by considering the difference between the predicted mean of the high and multi-fidelity models.

In the example in figure 2-4, the first two low fidelity active samples have little impact on the mean of the multi-fidelity GP regression model. This is because the multi-fidelity GP regression model is close to the ground truth in these sampling locations so little improvement is made. The third low fidelity sample has a large impact on the multi-fidelity GP regression model because the ground truth is farther away from the prediction. For this reason, the inter-model acquisition function in use for this thesis calculates the absolute difference between the predicted mean of the high and multi-fidelity GP regression models. This is referred to as the absolute difference inter-model acquisition function and is defined in equation (2.17). The high fidelity sample is selected at the location in the domain where the maximum absolute difference between the mean of the high and multi-fidelity GP model exists. This is chosen to capitalize on the exploration of the low fidelity sampling. If this difference is the result of a divergence between the low and high fidelity simulations, rather than an optimal location where the high fidelity GP model could be improved, then the $\delta(\mathbf{X}_*)$ GP model from equations (2.10) and (2.11) is updated to account for this discrepancy. This correction allows the multi-fidelity GP regression model to provide greater opportunities to identify optimal locations for future high fidelity samples.

$$\begin{aligned} q_{AD}(\mathbf{X}_*) = |y_{\mathcal{HF}}(\mathbf{X}_*) - y_{\mathcal{MF}}(\mathbf{X}_*)| = |y_{\mathcal{HF}}(\mathbf{X}_*) - (y_{\mathcal{LF}}(\mathbf{X}_*) + y_\delta(\mathbf{X}_*))| \\ x^*_{\mathcal{HF}} = \arg\max q_{AD}(\mathbf{X}_*) = \arg\max |y_{\mathcal{HF}}(\mathbf{X}_*) - y_{\mathcal{MF}}(\mathbf{X}_*)| \end{aligned} \tag{2.17}$$

Because the low fidelity model can be sampled many times before sampling a high fidelity data point, the non-myopic characteristic of the acquisition function emerges. It considers how the low fidelity model changes as it iterates through many future low fidelity samples and uses this information to determine the location of the next high fidelity sample. This non-myopia allows the more robust exploration of the domain in the low fidelity regime before a high fidelity sample is taken. This can help identify inaccuracies in the high fidelity regime.

2.3.2 Non-Myopic Multi-Fidelity (NMMF) Active Learning Algorithm

By combining the multi-fidelity GP regression framework with the non-myopic approach for active learning, the formulation of a non-myopic multi-fidelity active learning algorithm emerges. It consists of the following steps listed in the pseudo-code in Algorithm 1:

1. Begin with a small number of high and low fidelity simulations performed as bootstraps, i.e. $\mathcal{D}_{\mathcal{HF}}$ and $\mathcal{D}_{\mathcal{LF}}$. These bootstraps are performed at the same $\mathbf{X}$ locations within the domain but result in different outputs, i.e. $\mathbf{y}_{\mathcal{HF}}$ and $\mathbf{y}_{\mathcal{LF}}$. These bootstrapped data sets are used to determine $\mathcal{D}_\delta = \{\mathbf{X}, \mathbf{y}_\delta\}$ from equation (2.15). Next, GP regression is performed on $\mathcal{D}_{\mathcal{HF}}, \mathcal{D}_{\mathcal{LF}}, \mathcal{D}_\delta$ to obtain $y_{\mathcal{LF}}$, $y_{\mathcal{HF}}$, y_δ, $\sigma_{\mathcal{LF}}$, and $\sigma_{\mathcal{HF}} = \sigma_\delta$ using equations (2.12), (2.13), and (2.14).

2. Perform active learning to select a sample from the low fidelity model using equation (2.8) and run the corresponding low fidelity simulation. The uncertainty sampling acquisition function in equation (2.9) is used due to its ro-

bustness. After the sample has been selected and simulated, GP regression is performed using equation (2.13) to find the new $y_{\mathcal{LF}}$ and $\sigma_{\mathcal{LF}}$. This low fidelity sampling is repeated for a set number of iterations n. This search provides new information about the low fidelity GP regression model at many new points without having the cost of running multiple high fidelity simulations.

3. Select the high fidelity sample using equation (2.17) and perform the high fidelity simulation at this sample location. This inter-model acquisition function is non-myopic because it considers how the low fidelity model evolves through multiple samples and uses this information to select the high fidelity sampling location. Next, perform a low fidelity simulation at the location of the high fidelity sample and add it to the low fidelity data set $\mathcal{D}_{\mathcal{LF}}$.

4. Remove any low fidelity samples from the low fidelity data set $\mathcal{D}_{\mathcal{LF}}$ that are not at locations where high fidelity samples are also taken. This prevents the low fidelity data set from becoming too large to perform the inverse matrix operation in equation (2.13) and from having a negative impact on the GP regression. Use equation (2.15) to update $\mathcal{D}_{\delta}$ with the new high fidelity sample. Finally, perform GP regression on $\mathcal{D}_{\mathcal{HF}}, \mathcal{D}_{\mathcal{LF}}, \mathcal{D}_{\delta}$ to obtain $y_{\mathcal{LF}}$, $y_{\mathcal{HF}}$, y_{δ}, $\sigma_{\mathcal{LF}}$, and $\sigma_{\mathcal{HF}} = \sigma_{\delta}$ using equations (2.12), (2.13), and (2.14).

5. Repeat steps 2 through 4 until the desired number of high fidelity samples is taken m.

The pseudo-code in Algorithm 1 outlines the non-myopic multi-fidelity active learning algorithm for GP regression.

Algorithm 1 Non-Myopic Multi-Fidelity (NMMF) Active Learning

```
Input: $\mathcal{D}_{\mathcal{HF}} = \{X_{\mathcal{HF}}, \mathbf{y}_{\mathcal{HF}}\}, \mathcal{D}_{\mathcal{LF}} = \{X_{\mathcal{LF}}, \mathbf{y}_{\mathcal{LF}}\}, \mathcal{D}_{\delta} = \{\mathbf{X}_{\delta}, \mathbf{y}_{\delta}\}$ where $X_{\mathcal{LF}} = X_{\mathcal{HF}} = X_{\delta}$
Perform GP regression on $\mathcal{D}_{\mathcal{HF}}, \mathcal{D}_{\mathcal{LF}}, \mathcal{D}_{\delta}$ to obtain $y_{\mathcal{LF},0}(\mathbf{X}_*)$, $\sigma_{\mathcal{LF},0}(\mathbf{X}_*)$, $y_{\mathcal{HF},0}(\mathbf{X}_*)$, $\sigma_{\mathcal{HF},0}(\mathbf{X}_*)$, $y_{\delta,0}(\mathbf{X}_*)$, $\sigma_{\delta,0}(\mathbf{X}_*)$; equations (2.12, 2.13, 2.14)
For $i = 1$ to $m$
    For $j = 1$ to $n$
        Select low fidelity location $x^*_{\mathcal{LF},j} = arg\ max\ q_{US}(\mathbf{X}_* | \sigma_{\mathcal{LF},j-1}(\mathbf{X}_*))$; equations (2.8, 2.9)
        Run low fidelity simulation at $x^*_{\mathcal{LF},j}$ to obtain $y^*_{\mathcal{LF},j}$
        Temporarily augment data set $\mathcal{D}_{\mathcal{LF},j} = \{(\mathbf{X}_{\mathcal{LF},j-1}, \mathbf{y}_{\mathcal{LF},j-1}) \cup (x^*_{\mathcal{LF},j}, y^*_{\mathcal{LF},j})\}$ until $x^*_{\mathcal{HF},i}$ is found
        Perform GP regression on $\mathcal{D}_{\mathcal{LF},j}$ to obtain $y_{\mathcal{LF},j}(\mathbf{X}_*), \sigma_{\mathcal{LF},j}(\mathbf{X}_*)$; equation (2.13)
    End For
    Select high fidelity location $x^*_{\mathcal{HF},i} = arg\ max\ q_{AD}(\mathbf{X}_* | y_{\mathcal{HF}}(\mathbf{X}_*), y_{\mathcal{LF}}(\mathbf{X}_*), y_{\delta}(\mathbf{X}_*))$; equation (2.17)
    Run high fidelity simulation at $x^*_{\mathcal{HF},i}$ to obtain $y^*_{\mathcal{HF},i}$
    Augment data set $\mathcal{D}_{\mathcal{HF},i} = \{(\mathbf{X}_{\mathcal{HF},i-1}, \mathbf{y}_{\mathcal{HF},i-1}) \cup (x^*_{\mathcal{HF},i}, y^*_{\mathcal{HF},i})\}$
    Restore low fidelity data set $\mathcal{D}_{\mathcal{LF}}$ to condition before augmented with $x^*_{\mathcal{LF},j}, y^*_{\mathcal{LF},j}$, i.e. $\mathcal{D}_{\mathcal{LF},i-1}$
    Run low fidelity simulation at $x^*_{\mathcal{LF},i} = x^*_{\mathcal{HF},i}$ to obtain $y^*_{\mathcal{LF},i}$
    Augment data sets $\mathcal{D}_{\mathcal{LF},i} = \{(\mathbf{X}_{\mathcal{LF},i-1}, \mathbf{y}_{\mathcal{LF},i-1}) \cup (x^*_{\mathcal{LF},i}, y^*_{\mathcal{LF},i})\}$, and $\mathcal{D}_{\delta,i} = \{(\mathbf{X}_{\delta,i-1}, \mathbf{y}_{\delta,i-1}) \cup (x^*_{\mathcal{LF},i}, y^*_{\mathcal{HF},i} - y^*_{\mathcal{LF},i})\}$; equation (2.15)
    Perform GP regression on $\mathcal{D}_{\mathcal{HF},i}, \mathcal{D}_{\mathcal{LF},i}, \mathcal{D}_{\delta,i}$ to obtain $y_{\mathcal{LF},i}(\mathbf{X}_*)$, $\sigma_{\mathcal{LF},i}(\mathbf{X}_*)$, $y_{\mathcal{HF},i}(\mathbf{X}_*)$, $\sigma_{\mathcal{HF},i}(\mathbf{X}_*)$, $y_{\delta,i}(\mathbf{X}_*)$, $\sigma_{\delta,i}(\mathbf{X}_*)$; equations (2.12, 2.13, 2.14)
End For
```

2.3.3 Advantages of Multi-Fidelity Gaussian Process Regression Model

While the multi-fidelity GP regression model serves an important role in the active learning process by reducing cost and increasing accuracy of the surrogate model, there are additional benefits that come from using this approach. Because this multi-fidelity GP model is used to find the relationship between the high fidelity and low fidelity simulators, this difference can be used by simulation developers to better understand the limitations of low fidelity simulators. There may be portions of the input space in which the low fidelity model is suitable for many purposes. The multi-fidelity GP model helps quantify the accuracy of the low fidelity model with respect to the high fidelity model. Additionally, the results of the multi-fidelity GP model could be integrated directly into the low fidelity simulators to improve their accuracy.

2.4 Evaluation of NMMF Active Learning Algorithm

To assess the performance of the NMMF active learning algorithm compared to other state of the art algorithms, a large number of high fidelity simulations needs to be performed. For this reason, multiple test problems were used to evaluate the performance of the NMMF algorithm before it is used for CFD simulations on UUV hydrodynamic interactions. Specifically, the performance of the developed algorithm is compared to that of the traditional myopic multi-fidelity sampling method, as well as the standard sampling method using the US acquisition function for the high fidelity model.

Four different prototype problems are selected in a multi-fidelity setup with a number of dimensions close to that of the UUV and submarine hydrodynamics problem. For the test problems in this section, the number of low fidelity samples that are performed before selecting the high fidelity sampling location is held constant at 10. The error in use to evaluate the accuracy of the surrogates is the Mean Absolute Percentage Error (MAPE). This is chosen because it normalizes the error, rather than looking at absolutes error alone. The MAPE is defined in the following equation in terms of the predicted quantity, y_p, and its exact value y_e:

$$MAPE = \frac{1}{n}\sum_{i=1}^{n}\left|\frac{y_{p,i} - y_{e,i}}{y_{e,i}}\right| \tag{2.18}$$

2.4.1 Park Function

Park developed a four dimensional problem that has been used in literature to evaluate the accuracy of computer models [37]. Xiong provided a low fidelity approximation to this function which has further been used to evaluate multi-fidelity models [38].

The following equations are the high and low fidelity models used to evaluate the non-myopic multi-fidelity sampling algorithm.

$$y_{\mathcal{HF}}(x) = \frac{2}{3}e^{x_1+x_2} - x_4 \sin(x_3) + x_3 \tag{2.19}$$

$$y_{\mathcal{LF}}(x) = 1.2y_{\mathcal{HF}}(x) - 1 \tag{2.20}$$

The domain of the input space is $x_i \, \epsilon \, [0, 1]$ for all $i = 1, 2, 3, 4$. In order to evaluate the performance of the new sampling method, the NMMF sampling algorithm is run alongside the traditional myopic multi-fidelity sampling algorithm and a standard high fidelity active learning algorithm. The following plot shows how the error of the different methods is reduced as the number of high fidelity simulations was performed. The entire process was repeated 100 times to reduce the variance between experiments.

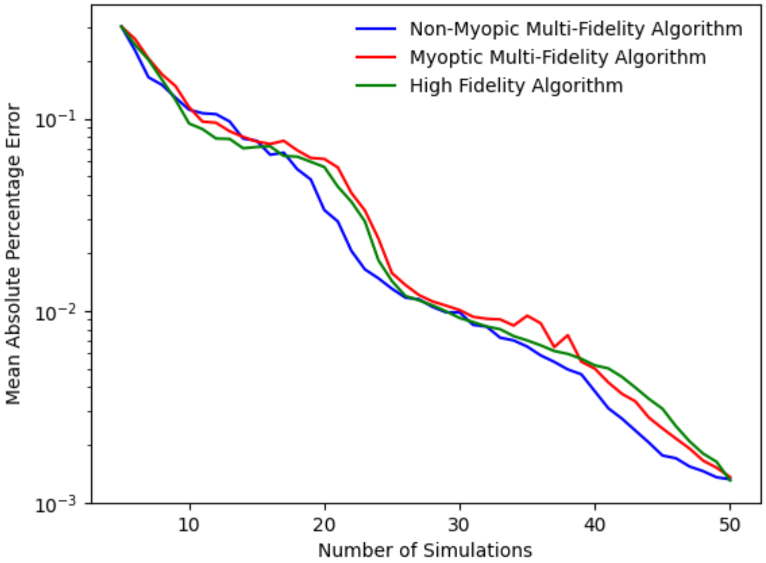

Figure 2-5: Comparison of non-myopic multi-fidelity active learning algorithm against other active sampling algorithms on the Park function.

Overall, throughout the majority of the solution space, the NMMF sampling algorithm outperforms both the myopic multi-fidelity and standard high fidelity algorithms. While the NMMF algorithm did not start out as the most accurate method, after about 18 simulations, this method improved the accuracy of the surrogate model more than the other methods. These results support using the non-myopic multi-fidelity sampling algorithm to increase the accuracy of a surrogate model at a cheaper cost.

2.4.2 Three DOF trebuchet with a hinged counterweight and sling

Consider other test problem that simulates the projectile range from a three degree of freedom (DOF) trebuchet with a hinged counterweight and sling [39, 40, 41]. Figure 2-6 illustrates the mechanical system of the simulation.

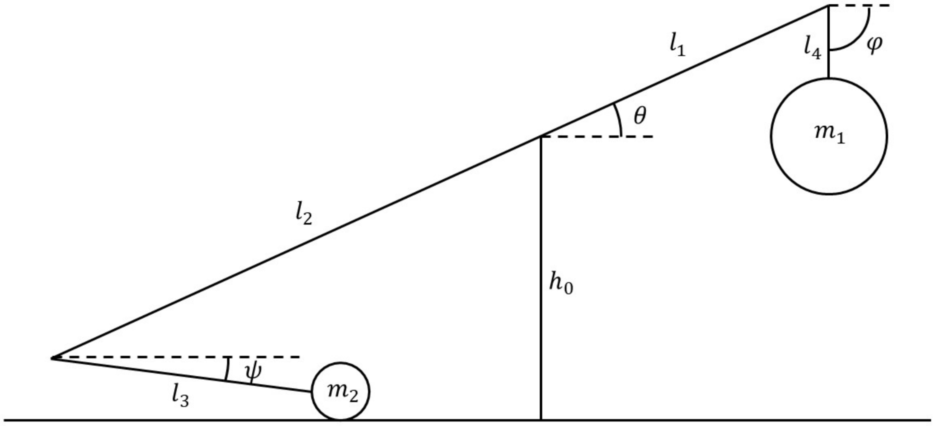

Figure 2-6: Three DOF Trebuchet with a Hinged Counterweight and Sling

Using Lagrangian mechanics, the equations of motion outlined in equation (2.21) are derived to simulate the motion of the trebuchet using the variables defined in figure 2-6. These equations of motion are coupled and highly non-linear. These are the types of problems for which surrogate models are often created. The UUV hydrodynamic interactions are also coupled and non-linear like this test case.

$$\begin{bmatrix} m_1 l_1^2 + m_2 l_2^2 + m_{arm} l_{arm}^2 + I_{arm} & m_1 l_1 l_4 \cos(\theta - \phi) & -m_2 l_2 l_3 \cos(\theta - \phi) \\ m_1 l_1 l_4 \cos(\theta - \phi) & m_1 l_4^2 & 0 \\ -m_2 l_2 l_3 \cos(\theta - \phi) & 0 & m_2 l_3^2 \end{bmatrix} \begin{bmatrix} \ddot{\theta} \\ \ddot{\phi} \\ \ddot{\psi} \end{bmatrix} = \\ \begin{bmatrix} -m_1 l_1 l_4 \dot{\phi}^2 \sin(\theta - \phi) + m_2 l_2 l_3 \dot{\psi}^2 \sin(\theta - \phi) - (m_1 l_1 - m_2 l_2 - m_{arm} l_{arm}) g \cos(\theta) \\ m_1 l_1 l_4 \dot{\theta}^2 \sin(\theta - \phi) - m_1 l_4 g \cos(\phi) \\ m_2 l_2 l_3 \dot{\theta}^2 \sin(\theta - \phi) - m_2 l_3 g \cos(\psi) \end{bmatrix} \tag{2.21}$$

where $m_{arm}{=}f(l_1, l_2, constants)$, $l_{arm}{=}f(m_{arm}, l_1, l_2, constants)$, and $I_{arm}{=}f(m_{arm}, l_1, l_2, constants)$.

The initial conditions in use to solve the system of equations are listed below:

$$\theta_0 = \sin^{-1}\left(\frac{h_0}{l_2}\right),\ \phi_0 = \frac{-\pi}{2},\ \psi_0 = 0,\ \dot{\theta}_0 = 0,\ \dot{\phi}_0 = 0,\ \dot{\psi}_0 = 0 \tag{2.22}$$

The projectile is released at a constant launch hook angle β. After the projectile is released, the range of the projectile is determined using standard Newtonian projectile motion physics which neglects air resistance.

These equations of motion have the potential to allow for a higher dimension domain by allowing more parameters to vary, like the launch hook angle β or other trebuchet arm moment of inertia parameters like material density or thickness of the arm. Likewise, the domain could be reduced by fixing certain input variables to a constant value. The domain for this problem is selected to be six-dimensional and the range of the various input variables is as follows:

$$
\begin{aligned}
l_1 &\in [0.5, 1.5] \text{ m} \\
l_2 &\in [3.5, 4.5] \text{ m} \\
l_3 &\in [3.0, 4.0] \text{ m} \\
l_4 &\in [0.1, 1.0] \text{ m} \\
h_0 &\in [3.0, 3.5] \text{ m} \\
m_1 &\in [40, 400] \text{ kg}
\end{aligned} \tag{2.23}
$$

A simpler two degree of freedom simulation is used for the low fidelity model of the trebuchet. For this model, the counterweight is not hinged. Instead, it is mounted directly on the end of the trebuchet rotating arm. This simplifies the equations of motion by removing the influence of the l_4 and ϕ variables.

Figure 2-7 shows the performance of the different methods on the three DOF trebuchet problem. The entire process is repeated 100 times to reduce the variance between experiments.

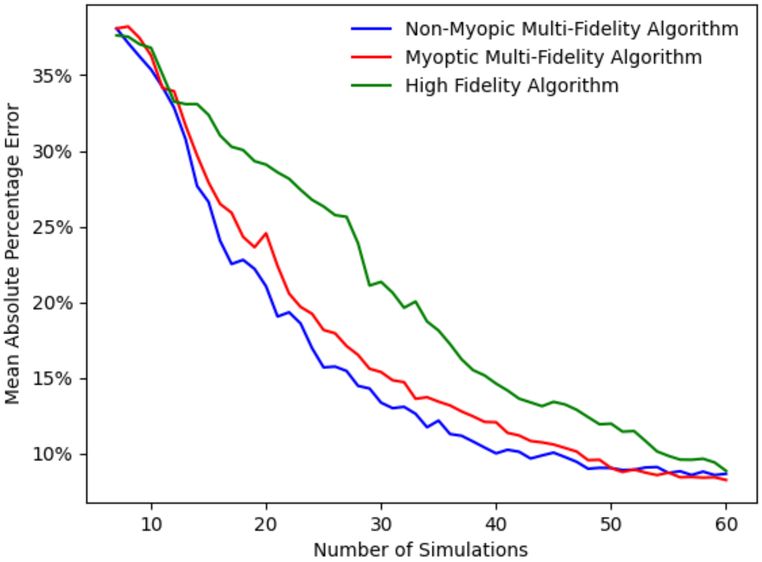

Figure 2-7: Comparison of non-myopic multi-fidelity active learning algorithm against other active sampling algorithms on the three DOF trebuchet.

The addition of the extra low fidelity data points significantly improves the surrogate model. In addition, the non-myopic multi-fidelity sampling method produces a more accurate model with fewer high-fidelity experiments than the other sampling methods, although the benefits in this case are not substantial.

2.4.3 Borehole Function

The borehole function is an eight-dimensional highly non-linear equation developed by Harper and Gupta [42]. This equation is used to determine the volumetric flow rate through a borehole that is drilled through an upper aquifer, a nuclear waste repository, and into a lower aquifer. This function has been used in literature to evaluate the performance of computer models [25]. Xiong also developed a low fidelity approximation of this model which enables the borehole function to also evaluate multi-fidelity models [38]. The multi-fidelity borehole function, listed in equations (2.24) and (2.25), is used to evaluate the performance of the non-myopic multi-fidelity sampling algorithm.

$$y_{\mathcal{HF}}(x) = \frac{2\pi T_u(H_u - H_l)}{\ln{(r/r_w)}} \left(1 + \frac{2LT_u}{\ln{(r/r_w)} r_w^2 K_w} + \frac{T_u}{T_l}\right)^{-1} \tag{2.24}$$

$$y_{\mathcal{LF}}(x) = \frac{5T_u(H_u - H_l)}{\ln{(r/r_w)}} \left(1.5 + \frac{2LT_u}{\ln{(r/r_w)} r_w^2 K_w} + \frac{T_u}{T_l}\right)^{-1} \tag{2.25}$$

Equation (2.26) lists the domain of the various input variables.

$$\begin{aligned} r_w &\in [0.05, 0.15] \text{ m} \\ r &\in [100, 50000] \text{ m} \\ T_u &\in [63070, 115600] \text{ m}^2/\text{yr} \\ H_u &\in [990, 1110] \text{ m} \\ T_l &\in [63.1, 116] \text{ m}^2/\text{yr} \\ H_l &\in [700, 820] \text{ m} \\ L &\in [1120, 1680] \text{ m} \\ K_w &\in [9855, 12045] \text{ m}/\text{yr} \end{aligned} \tag{2.26}$$

The considered GP sampling methods are evaluated on the borehole function 450 times to reduce the variance of the results. Figure 2-8 shows how each method performs on the borehole function test case.

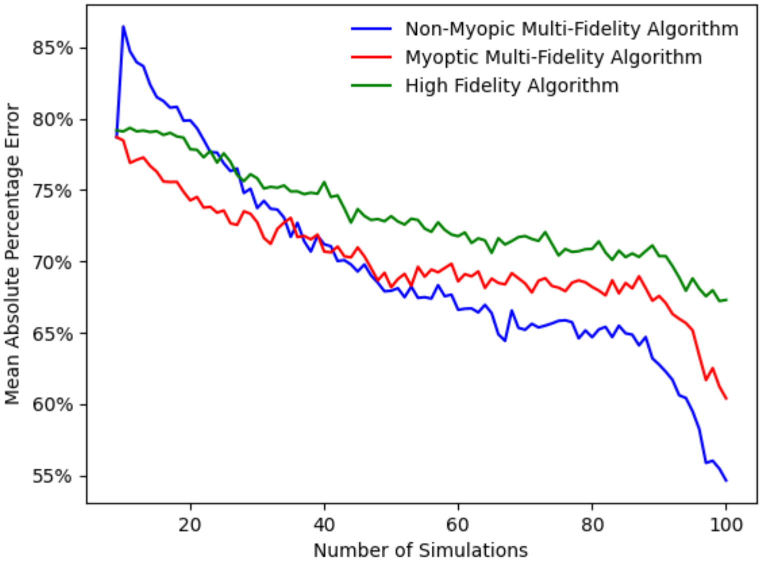

Figure 2-8: Comparison of non-myopic multi-fidelity active learning algorithm against other active sampling algorithms on the borehole function.

The NMMF sampling method is able to produce the lowest model error in the majority of the solution space. Initially, this method has the highest error, but it rapidly improves to the most accurate sampling scheme, approximately after 30 to 40 simulations are conducted. This is likely because the low and high fidelity models have a larger difference than in the other test cases. This means that the initial high fidelity samples are likely used to quantify the difference $\delta(\mathbf{X}_*)$ (equations (2.10) and (2.11)) between the high and low fidelity models, rather than better explore the domain. Once this difference is well explored and quantified, the exploratory benefits of the NMMF algorithm quickly outperform the other two sampling methods.

2.4.4 Subsonic Straight-Tapered Wing Lift Curve Slope

The last test problem used to evaluate the NMMF active learning GP algorithm is the prediction of the Wing Lift Curve Slope for subsonic straight-tapered aircraft wings. This approach used two different models from *USAF Stability and Control DATCOM* and from *Commercial Airplane Design Principles* [43, 44]. The following series of equations were used as the low and high fidelity models.

Low fidelity model:

$$\begin{aligned}
\Lambda_{LE} &= \tan^{-1}\left(\tan(\Lambda_{c/4}) + \frac{1}{A}\left(\frac{1-\lambda}{1+\lambda}\right)\right) \\
(C_{L_\alpha})_{theory} &= 8\tan^{-1}\left(\frac{\pi A}{16 + \pi A/(1 + 2\lambda\tan(\Lambda_{LE}))}\right) \\
\frac{C_{L_\alpha}}{(C_{L_\alpha})_{theory}} &= f\left(\frac{1}{3+A}\left(\frac{1-\lambda}{1+2\lambda}\right)^2, \frac{t}{c}\right) \text{ from Figure 4.1.3.2-50a [44]} \\
y_{\mathcal{LF}}(x) &= C_{L_\alpha} = (C_{L_\alpha})_{theory}\left(\frac{C_{L_\alpha}}{(C_{L_\alpha})_{theory}}\right)
\end{aligned} \tag{2.27}$$

High fidelity model:

$$\begin{aligned}
&\beta = \sqrt{1 - M^2} \\
&\kappa = c_{l\alpha}/2\pi \\
&\Lambda_{c/2} = \tan^{-1}\left(\tan(\Lambda_{c/4}) - \frac{1}{A}\left(\frac{1-\lambda}{1+\lambda}\right)\right) \\
&y_{\mathcal{HF}}(x) = C_{L_\alpha} = \frac{2\pi A}{2 + \sqrt{\frac{A^2\beta^2}{\kappa^2}\left(1 + \frac{\tan^2(\Lambda_{c/2})}{\beta^2}\right) + 4}}
\end{aligned} \tag{2.28}$$

The domain across the various input variables is as follows.

$$\begin{aligned}
&c_{l\alpha}\,\epsilon\,[0.11, 0.12] \\
&A\,\epsilon\,[5, 20] \\
&\lambda\,\epsilon\,[0.2, 0.25] \\
&\Lambda_{c/4}\,\epsilon\,[15, 35] \text{ degrees} \\
&M\,\epsilon\,[0.2, 0.8] \\
&t/c\,\epsilon\,[0.08, 0.2]
\end{aligned} \tag{2.29}$$

The various sampling methods are repeated on the Wing Lift Curve Slope 100 times to ensure the consistency of the results. The figure below shows the performance of each sampling method.

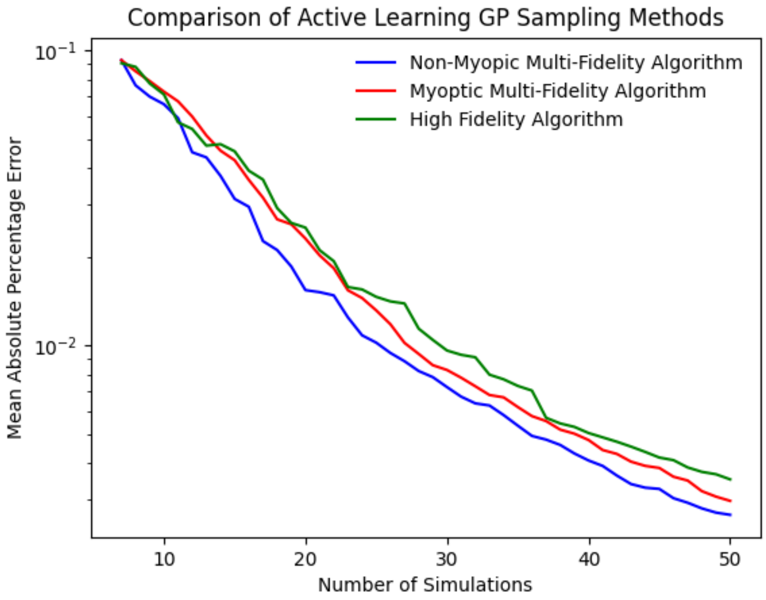

Figure 2-9: Comparison of non-myopic multi-fidelity active learning algorithm against other active sampling algorithms on the wing lift curve slope.

Once again, the NMMF sampling method is able to produce the lowest error as high fidelity simulations are added to the surrogate models. This means that a more accurate surrogate can be developed using a smaller number of expensive high fidelity simulations which further supports the use of the non-myopic multi-fidelity active learning algorithm.

2.5 Adaptations for Multi-Dimensional Outputs

The considered example problems demonstrate the effectiveness of the NMMF active learning algorithm in setups where the output is a scalar quantity. However, for the submarine and UUV hydrodynamic interaction problem, the hydrodynamic interaction surrogate model has vector outputs. One can address this issue by simply building three separate surrogate models, one for each output. This is a simple approach that is often used in practice rather than adapting GP regression kernels for multiple outputs due to its ease of implementation [45]. However, having multiple outputs creates a new obstacle for the active learning process. When a high fidelity

CFD simulation is run at a single location in the domain, all three outputs are determined. The acquisition functions so far have been for a single output, but they need to be modified to account for multiple outputs. The best way to make these modifications is explored and evaluated.

Three different methods are considered as options to determine the optimal sampling location for the multiple outputs. The first is a round robin method, meaning that the output for which the optimal point is selected is alternated between all the outputs. The number of outputs of the surrogate is denoted as k. Let σ_i^2 denote each one of the three different surrogate output variances or epistemic uncertainties where $i = 1, ..., k$. Equation (2.30) shows the round robin method in which the sampling location is selected by alternating which output is used for the acquisition function over the span of all n samples.

$$x_{j+1}^* = \text{arg max}\, q_{US}\left(x|\sigma_i\right) \text{ for } i = j - 1(\,mod\, k) + 1. \tag{2.30}$$

The second method is the maximum variance method. This approach begins by computing the optimal sampling location x_i' for each output individually. Next, the GP model is used to predict the epistemic variance at each location $\sigma_i^2(x_i')$. This is then normalized by the measured variance of the output data for each output $\sigma_{y,i}^2$. Lastly, the sampling location with the largest normalized variance is selected because this is the theorized location in which a sample could best reduce the uncertainty of the multiple outputs. Equation (2.31) denotes the maximum variance method.

$$\begin{gathered} x_{j+1}^* = \text{arg max}\left(\frac{\sigma_i^2(x_i')}{\sigma_{y,i}^2}\right) \text{ for } i = 1, .., k, \\ \text{where} \quad x_i' = \arg\max q_{US}(x|\sigma_i^2) \quad \text{and} \quad \sigma_{y,i}^2 = \frac{1}{j}\sum_{l=1}^{j}\left(y_{i,l} - \bar{y}_i\right)^2 \end{gathered} \tag{2.31}$$

The third method under consideration is called the weighted method. This approach looks for an optimal sampling location by assessing the multiple outputs as a whole rather than individually. Specifically, the statistics of the individual outputs are combined based on a weight factor into a single weighted variance σ_w^2 to be used with the US acquisition function. The weight used for each output is the inverse of its training data variance for that given output. This is used as the weight in order to try and normalize the different output variances before they are combined. If they are not normalized, then the variance of one output could dominate the weighted variance, even if it has a low epistemic uncertainty. This could happen because the outputs are not normalized so outputs with larger values would have a larger impact on the weighted variance. Once these individual variances are combined into a single weighted variance, the optimal sampling location is selected using the following acquisition function:

$$x_{j+1}^* = \arg\max q_{US}(x|\sigma_w^2(x)), \quad \text{where} \quad \sigma_w^2(x) = \sum_{i=1}^{k} \frac{\sigma_i^2(x)}{\sigma_{y,i}^2} \tag{2.32}$$

An example problem with three outputs y_1, y_2, and y_3 is used to evaluate these different multiple output sampling methods. The Park 1, Park 2, and Colville functions listed as equations (2.33), (2.34), and (2.35) are used as the three surrogate outputs [46]. The domain of the input space is $x_i \in [0.1, 1]$ for all $i = 1, 2, 3, 4$.

$$y_1(x) = \frac{2}{3}e^{x_1+x_2} - x_4 \sin(x_3) + x_3 \tag{2.33}$$

$$y_2(x) = \frac{x_1}{2}\left[\sqrt{1 + (x_2 + x_3^2)\frac{x_4}{x_1^2}} - 1\right] + (x_1 + 3x_4)e^{1+\sin(x_3)} \tag{2.34}$$

$$\begin{aligned} y_3(x) = {} & 100(x_1^2 - x_2)^2 + (x_1 - 1)^2 + (x_3 - 1)^2 + 90(x_3^2 - x_4)^2 \\ & + 10.1((x_2 - 1)^2 + (x_4 - 1)^2) + 19.8(x_2 - 1)(x_4 - 1) \end{aligned} \tag{2.35}$$

The various multiple output sampling methods are repeated 100 times to ensure the results are consistent. Figure 2-10 shows the performance of each sampling method.

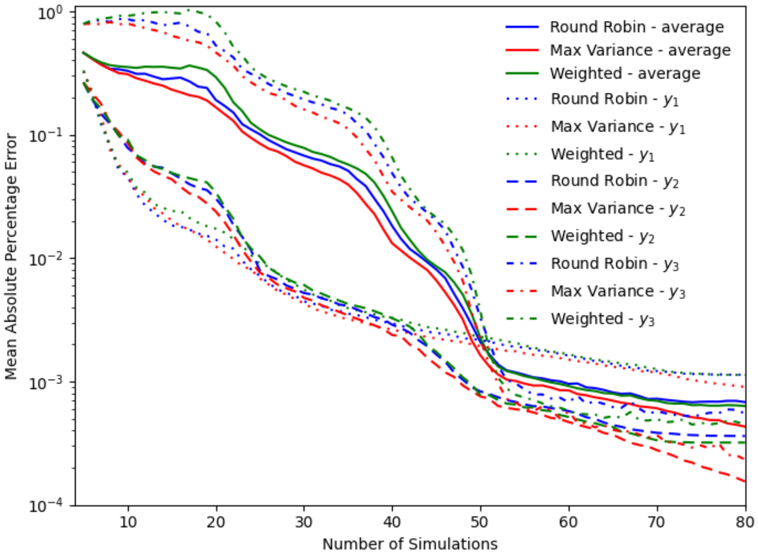

Figure 2-10: Comparison of the round robin, maximum variance, and weighted multiple output active sampling methods for three test cases.

The maximum variance criterion slightly outperforms the other two sampling methods. This is true when looking at each output individually and also when looking at the average MAPE of all three outputs. The only portion of the solution space in which the maximum variance criterion did not outperform the other two methods is in the early stages of the sampling with less than 20 samples for y_1. The round robin method allocates optimal samples to this output despite it having the smallest error while the maximum variance method allocates optimal samples for the outputs with larger errors. This allows the round robin method to temporarily outperform the maximum variance method for y_1. However, the maximum variance method is able to quickly catch up and outperform the round robin method for this output. The weighted output method underperformed the other two methods. To this end, the maximum variance criterion is selected as the multiple output sampling method for the UUV and submarine hydrodynamic interactions problem.

2.6 Conclusion

A new method for active sampling has been formulated that is non-myopic and also utilizes models of multiple fidelity. The new approach allows for efficiently computing reduced order models with unprecedented accuracy due to its non-myopic active search properties. It is ideal for situations where plentiful and accurate training data is not easy to obtain, e.g. because of high computational cost. The advantages of the new approach are demonstrated in four representative prototype systems. Additionally, three different active sampling methods are evaluated for multiple output GP regression models, with the maximum variance method having the best performance. Overall, the NMMF active learning method is able to outperform the other sampling methods and emerges as the ideal candidate for use when creating a surrogate model to accurately predict the complex hydrodynamic interactions between a submarine and UUV. This approach is well suited to capitalize on the high accuracy of the CFD and the exploration of the low fidelity potential flow model.

Using GP regression as a surrogate enables the real-time prediction of the UUV hydrodynamic interactions with the accuracy of CFD. Real-time modeling of these hydrodynamic interactions is essential to simulate the motion required to launch and recover UUVs from submarines. To this end, this surrogate model may be integrated into UUV control and autonomy systems and motion simulators to further enable UUV launch and recovery from submarines.

THIS PAGE INTENTIONALLY LEFT BLANK

Chapter 3

Computational Modeling of Multiple Body Hydrodynamic Interactions

3.1 Introduction

One of the objectives of this thesis is to create a surrogate model that can make real time predictions of the forces and moments due to the hydrodynamic interactions between a moving UUV and submarine operating in close proximity. This surrogate model must be capable of determining these forces and moments based on the any relative speed, longitudinal position, lateral position, heading angle, and size difference between the two vehicles. Determining these hydrodynamic interactions in real time enables the surrogate model to be incorporated into the UUV control and autonomy systems. Before this surrogate model can be created, the hydrodynamic interaction forces and moments needed to be accurately simulated. The results of these simulations can then be used as training data for the surrogate model. Without verifying and validating the accuracy of the simulations, error could be introduced into the surrogate model. Due to the complex and resource intensive nature of the building real-world physical models, potential flow (P-Flow) and computational fluid dynamics (CFD) are used as two different simulation approaches to determine the forces and moments caused by the hydrodynamic interactions.

3.2 Vehicle Configuration

In 1989, the Submarine Technology Program Office of the Defense Advanced Research Projects Agency (DARPA) developed a submarine hull geometry known as the SUBOFF model. The purpose of this standardized submarine hull geometry is to allow computational methods like potential flow analysis or CFD and real-world modeling using experimental fluid dynamics (EFD) to be performed by different entities. The DARPA SUBOFF model is a relevant submarine hull shape and has since been studied extensively using both CFD and EFD approaches [47, 48, 49, 50, 51, 52]. As such, the DARPA SUBOFF submarine hull model is the ideal candidate with which to perform the P-Flow and CFD simulations for this study. A scale model of the International Submarine Engineering (ISE) Explorer AUV is used as the submarine in the simulation in order to be consistent with the EFD results [3, 53]. The bow of the Explorer model is an ellipsoid while the stern is a paraboloid. The equation of the elliptical cross section of the bow is as follows where x is the distance along the vehicle axis, y is the perpendicular distance from the axis, and R_{UUV} is the radius of the vehicle.

$$\left(\frac{x}{2R_{UUV}}\right)^2 + \left(\frac{y}{R_{UUV}}\right)^2 = 1 \tag{3.1}$$

Likewise, the equation for the parabolic cross section of the stern is listed below.

$$\left(\frac{x}{4R_{UUV}}\right)^2 + \frac{y}{R_{UUV}} = 1 \tag{3.2}$$

To begin the P-Flow and CFD simulations, the unappended SUBOFF model and the Explorer model are created in Siemens Solid Edge, a three-dimensional computer aided design (CAD) modeling software. For the purpose of P-Flow and CFD validation, in order to be consistent with the EFD data, the SUBOFF model is used as the UUV while the Explorer model is used as the submarine. The EFD data used to validate the hydrodynamic interactions between the two vehicles is gathered at a submarine to UUV diameter ratio D_{Sub}/D_{UUV} of 2.239. This same diameter ratio was used for the potential flow and CFD simulations. The length and diameter of the Explorer submarine model are $L_{Sub} = 2.935$ m and $D_{Sub} = 0.405$ m respectively. To maintain the same diameter ratio as the EFD experiments, the length and diameter of the UUV SUBOFF model are determined to be $L_{UUV} = 1.552$ m and $D_{UUV} = 0.181$ m respectively. The simulations are run at a forward speed of $U = 0.75$ m/s with a water density of $\rho = 997 kg/m^3$ and dynamic viscosity of $\mu = 8.899x10^{-4}$ Pa-s. Using the both the submarine and UUV lengths over all (LOA) as the characteristic lengths L, the Reynolds Numbers are $Re_{Sub} = 2.47x10^6$ and $Re_{UUV} = 1.31x10^6$. All of these parameters are held constant across the different simulations to align with the EFD methods.

Two non-dimensional parameters known as the lateral and longitudinal separation ratios, R_{Lat} and R_{Long}, are used to refer to the distances between the two vehicles in non-dimensional terms. The equations for these two parameters are as follows

$$R_{Lat} = \frac{y_{Dist}}{L_{Sub}} \tag{3.3}$$

$$R_{Long} = \frac{x_{Dist}}{L_{Sub}} \tag{3.4}$$

where the relative lateral distance x_{Dist} and relative longitudinal distance y_{Dist} are measured between the centers of buoyancy (CB) of the two vehicles. The R_{Long} parameter is positive when the CB of the UUV is located in front of the CB of the submarine. The following figure illustrates the geometry and arrangements of the P-Flow and CFD simulations.

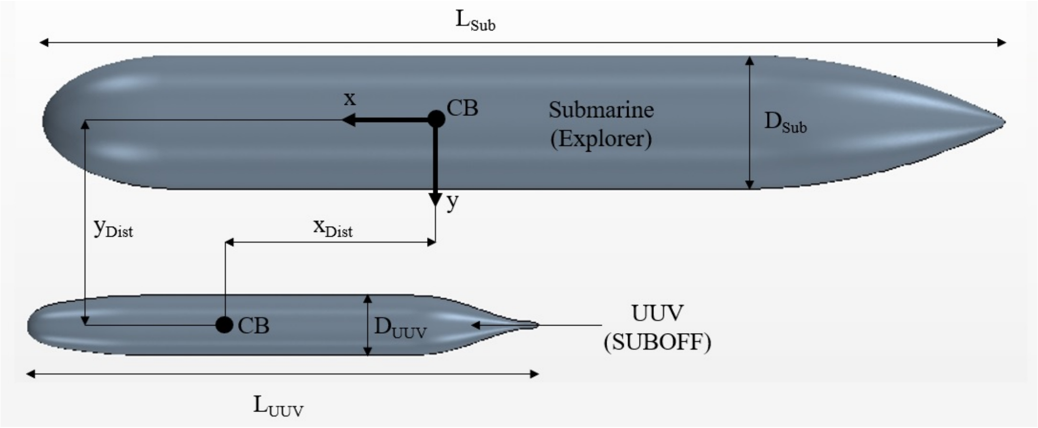

Figure 3-1: Geometry and orientation of vehicles configuration used to perform the potential flow and CFD simulations. This is consistent with the EFD setup in order to validate the results.

3.3 Computational Fluid Dynamics

3.3.1 Introduction

In order to complete the objectives of this study, many CFD simulations need to be performed based on the relative speed, longitudinal position, lateral position, heading angle, and size difference between the two vehicles. Ideally, a mesh independence study, turbulence model independence study, and boundary layer independence study would be performed for each configuration and simulation in the study, but this would be computationally very expensive. Due to the limited resources available to perform these necessary CFD simulations, various methods in the literature are leveraged to ensure that accurate results are obtained. Resources are best spent examining the domain of the surrogate model in order to deepen the understanding and resolution of the solution space rather than performing these independence studies for each possible configuration. Additionally, CFD simulations are validated against results from EFD methods using a tow tank in order to confirm their accuracy. This further removes the necessity for independence studies.

3.3.2 Governing Equations

The fundamental principles used to develop the governing hydrodynamic equations are the conservation of mass and the conservation of momentum. The equation for the conservation of mass for a fluid is

$$\frac{\partial \rho}{\partial t} + \vec{v} \cdot \nabla \rho + \rho \nabla \cdot \vec{v} = \frac{D\rho}{Dt} + \rho \nabla \cdot \vec{v} = 0 \tag{3.5}$$

where ρ is the density of the fluid and $\vec{v} = \langle u, v, w \rangle$ is the three dimensional Cartesian velocity of the fluid. The first two terms in equation (3.5) combine into the material derivative of the density $D\rho/Dt$.

The conservation of momentum for a fluid in differential form is

$$\rho \frac{D\vec{v}}{Dt} = \rho \left(\frac{\partial \vec{v}}{\partial t} + \vec{v} \cdot \nabla \vec{v} \right) = \vec{F} + \nabla \cdot \tau \tag{3.6}$$

where τ is three by three tensor of the stresses on the fluid. These conservation of momentum equations conserve momentum in the three Cartesian directions and are often referred to as the Euler equations. While the conservation of mass and three conservation of momentum equations provide a well defined structure, they do not provide enough constraint to usefully resolve a given fluid field. These equations provide a total of 10 unknowns, each one representing a three-dimensional field that can also vary in time. These unknowns include the density $\rho(\vec{x}, t)$, three components of the velocity vector $\vec{v}(\vec{x}, t)$, and six elements of the stress tensor $\tau(\vec{x}, t)$. There are only six unknown elements of the stress tensor rather than nine due to its symmetric properties.

In order to close these systems of equations, two assumptions are made about the properties of the fluid. The first is that the density of the fluid is constant. This assumption is valid for the conditions in which submerged vehicles operate in the ocean. This means that the material derivative of the density $\frac{D\rho}{Dt} = 0$. As such, equation (3.5) simplifies to the following equation. This is often referred to as the continuity equation.

$$\nabla \cdot \vec{v} = 0 \tag{3.7}$$

The second assumption is that the fluid is a Newtonian fluid. This means that there is a linear relationship between the dynamic stresses of the fluid and the rate of strain of the fluid. Therefore, the stress tensor simplifies to the combination of the pressure terms on the diagonal and the off-diagonal dynamic stresses represented as proportions of the strain rates. This is shown in einstein notation in the equation below.

$$\tau_{\mathbf{ij}} = P\delta_{ij} + \mu \left(\frac{\partial u_i}{\partial x_j} + \frac{\partial u_j}{\partial x_i} \right) \tag{3.8}$$

The u_i represents a component of the velocity vector, P is the pressure, δ_{ij} is the Kroenecker delta function, and μ is the fluid property known as the dynamic viscosity that represents the linear relationship between the dynamic stresses and the rate of strain of the fluid. By substituting equation (3.8) into equation (3.6), these equations simplify to the following well-known Navier-Stokes equations for incompressible Newtonian fluids

$$\frac{D\vec{v}}{Dt} = \frac{\partial \vec{v}}{\partial t} + \left(\vec{v} \cdot \nabla\right) \vec{v} = -\frac{1}{\rho} \nabla P + \nu \nabla^2 \vec{v} + \frac{1}{\rho} \vec{F} \tag{3.9}$$

where the fluid kinematic viscosity is defined as $\nu = \mu/\rho$. Equations (3.7) and (3.9) constitute a closed system of governing equations because there are four equations and four unknowns. Each of these unknowns represents a field and includes the pressure $P(\vec{x}, t)$ and the three components of the velocity vector $\vec{v}(\vec{x}, t)$.

There is a means by which these four equations can be directly numerically solved. This is known as a direct numerical solution (DNS). However, turbulence creates a major challenge for DNS. In order to fully resolve the smallest scale eddies that arise due to turbulence, the resolution has to be so fine that even supercomputers with millions of core hours are only able to solve very simple geometries. For this reason, DNS is a good research tool for validating solutions, but not good as a means to solve the Navier-Stokes equations for engineering problems and explore design spaces [18].

Because these equations cannot be directly solved with the available computational resources, many different turbulence modeling schemes have been developed to be solved simultaneously with equations (3.7) and (3.9). These turbulence models make empirical approximations reduce the computational cost of solving these equations. There are many publicly available software packages that solve this system of equations using various turbulence models. The commercially available CFD simulation software known as Simcenter STAR-CCM+ is used for this research.

3.3.3 Single Vehicle CFD Simulation

The modeling of these viscous effects in the boundary layer have a major impact on the results of the CFD simulation. As such, great care is taken to ensure that the simulation methods appropriately model the viscous effects within the boundary layer. This includes performing CFD simulations on a single vehicle and validating the results before performing the CFD simulations and validation on the hydrodynamic interactions between two vehicles.

3.3.3.1 Domain

The domain of the CFD simulation is the region in which the solver applies the governing physics and equations to determine the flow around the object. The accuracy of CFD simulations depends on the size of the domain. The ITTC suggests that the domain inlet, outlet, and side walls all be at least one model length away from the object [54]. The domain of the single vehicle simulations all fell within these minimum values. The ITTC suggests that the inlet and outlet should be placed at least 10 and 20 model lengths away respectively if significant lift forces are expected. This is not the case for these simulations, even at the largest drift angles. Additionally, the outlet boundary is placed at a distance of three lengths away from the SUBOFF model following the CFD techniques of other studies [55, 56, 48]. The following figure illustrates the simulation domain for the single vehicle simulations.

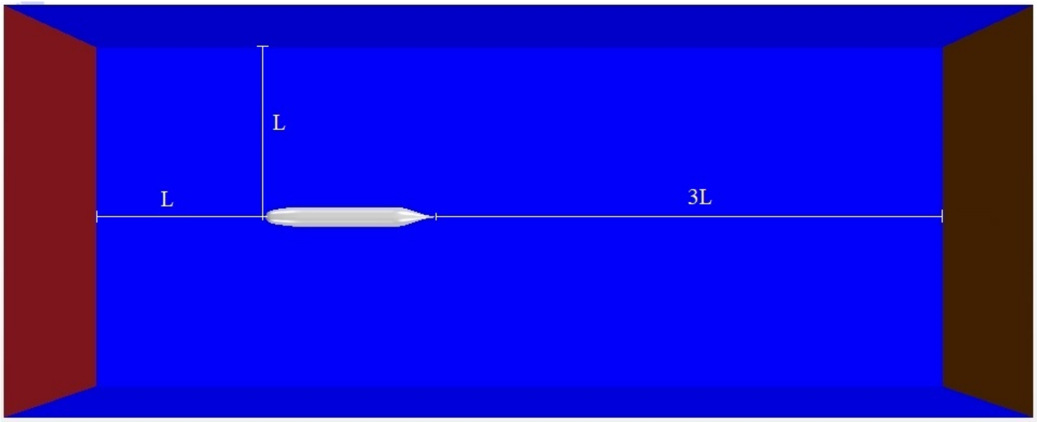

Figure 3-2: CFD domain of the SUBOFF hull simulation. Each wall is at least one vehicle length of separation from the model while the outlet boundary is three vehicle lengths of separation.

Additionally, symmetry is used to reduce the necessary size of the domain. This halves the time to complete the simulation, which enables twice the number of simulations that could be run for a given computational cost constraint. Because the SUBOFF model is axisymmetric, the domain size could be drastically reduced by only examining a small wedge about the model axis. However, when a second axisymmetric vehicle is added to the domain, there is only one plane of symmetry between the two vehicles. This is the plane which contains the axes of both vehicles. As such, the domain is limited to only one plane of symmetry which cuts the model in half. This ensures consistency with the two vehicle simulations performed in this thesis. The domain wall that intersected the SUBOFF model is assigned a symmetric boundary condition in order to capture the physics of the full model. All resulting forces and moments determined from the simulation are appropriately doubled to account for the full model, rather than the half model within the domain. The following figure illustrates the domain symmetry.

Figure 3-3: The CFD simulation domain utilizes symmetry to only model half of the vehicle in order to reduce the computational expense of the simulation.

3.3.3.2 Mesh

The mesh of the single vehicle CFD simulation is established to ensure that it met the necessary criteria to obtain accurate results according to various sources in literature. The density of the cells in this mesh near and within the boundary layer around the vehicle are much higher than around the edges of the domain. This because high fidelity is needed to accurately model the boundary layer around the vehicle compared to the far away bulk flow characteristics. According to mesh independence studies, a cell count of at least 1.2 million cells is needed in a domain of this size that does not utilize symmetry to in order to create accurate results [57, 55, 56]. The meshing techniques used in this thesis resulted in about 1.1 million cells, meaning it has the same resolution as a mesh with 2.2 million cells in a domain where symmetry is not utilized. This is well within the necessary cell count to provide accurate results.

This simulation setup uses an unstructured mesh because it more easily accommodates mesh deformation and restructuring [3]. This robust setup is particularly useful because of how these methods will ultimately be used to simulate a UUV which will be scaled and repositioned in multiple scenarios around a submarine. An unstructured mesh approach has also been found to be just as accurate as a structured mesh [58]. Additionally, in order to increase the resolution around the SUBOFF model, the surface growth rate is set to the cells size grow at a slower rate as they move away from the SUBOFF model. This technique better captures the physics of the flow around the hull and improves the accuracy of the simulation [3]. The figure below shows a cross section of the mesh used for this simulation setup.

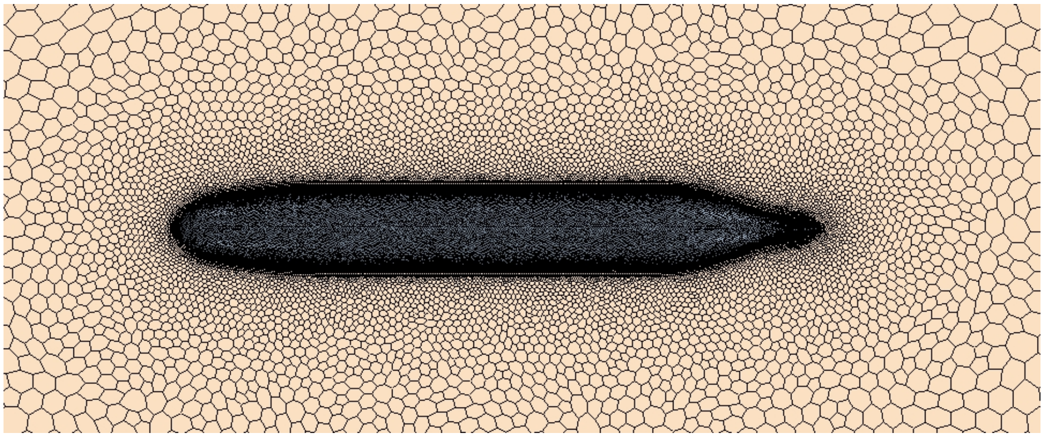

Figure 3-4: Cross section of the mesh used to validate the CFD simulation methods for the SUBOFF model.

3.3.3.3 Boundary Layer and Turbulence Modeling

Based on recommendations from the ITTC, two-equation turbulence models are by far the most common models that are applied to ship hydrodynamics and have consistently provided accurate predictions. This includes the k-ε and k-ω turbulence models. While there are more complex turbulence models, like the most classically complete Baseline Reynolds Stress Model (BSLRSM), they come at a much higher computational cost with only a small improvement in accuracy when compared to the two-equation turbulence models. For this reason, the vast majority of CFD simulations in literature use the two-equation turbulence models [54]. These different turbulence models have different required boundary layer modeling criteria recommended by the ITTC. The k-ω Shear-Stress Transport (SST) turbulence model is a modified set of equations that can be used to interpolate between these two models when the simulation falls in between these two criteria. For this simulation, the k-ω turbulence model is selected because it is more accurate in adverse pressure gradients like those experienced on the stern of the model [54, 59]. In order to ensure accuracy, this CFD simulation setup establishes the boundary layer according to the ITTC k-ω criteria so that there is no need to apply the k-ω SST model. However, STAR-CCM+

also provides backup to the user by applying the k-ω SST trubulence model in the event that this criteria is failed to be met. The total boundary layer thickness δ is determined using Prandtl's turbulent boundary layer thickness over a flat plate

$$\delta = 0.16L/Re_L^{1/7} \tag{3.10}$$

where L is the length of the vehicle and Re_L is the Reynolds number for this characteristic length. This boundary layer mesh is set up using prism layers with an expansion ratio of 1.2. The following figure illustrates the boundary layer mesh.

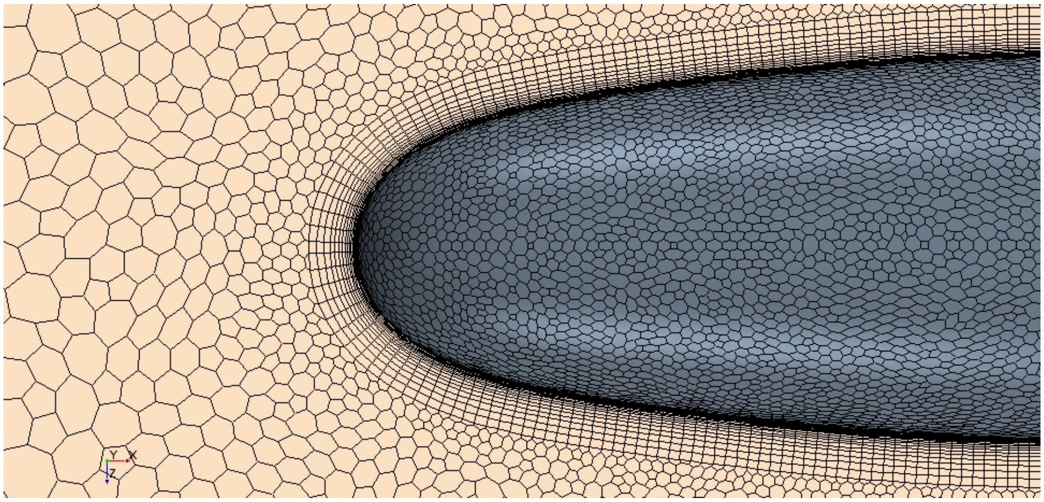

Figure 3-5: Cross section of the boundary layer mesh used to validate the CFD simulation methods for the SUBOFF model.

In order to satisfy the ITTC criteria for the k-ω turbulence model, the non-dimensional wall distance y^+ has to be less than one at all points along the model. The figure below shows the value of y^+ along the surface of the SUBOFF model. This demonstrates that the ITTC criteria is satisfied.

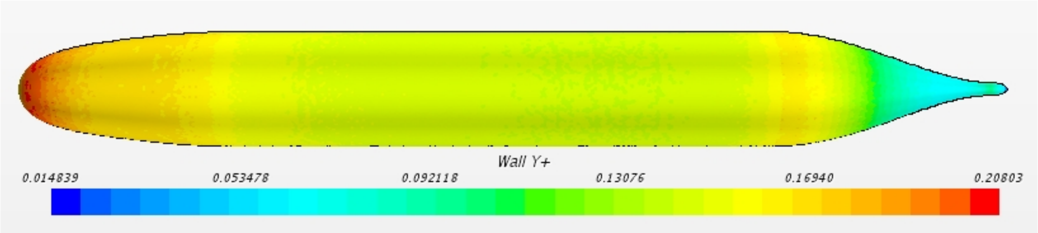

Figure 3-6: Non-dimensional wall distance y^+ across the surface of the SUBOFF model. This meets the requirement of being less than one at each point around the vehicle [54].

On average, the y^+ value along the model is about 0.15 with a maximum of 0.21. This meets the ITTC criteria which ensures that the boundary layer thickness on the vehicle is thin enough to allow the k-ω turbulence model to accurately model real-world physics.

3.3.3.4 Angled Vehicle Simulation

In order to accomplish the objective of this thesis of creating a surrogate model capable of predicting the hydrodynamic interactions between a UUV and submarine, the forces and moments of a UUV which is at a non-zero heading angle ψ need to be determined. Before the effects of the hydrodynamic interactions caused by the non-zero heading angle can be determined, the effects of varying the UUV heading angle ψ need to be validated on a single vehicle. Again, the DARPA SUBOFF model is used to simulate the forces and moments on the vehicle at various heading angles because of the readily available EFD data on this model. Multiple simulations are conducted and various heading angles up to 10.05 degrees. Overall, the same domain and mesh setup outlined in sections 3.3.3.1 and 3.3.3.2 is used on the angled vehicle simulation. The ITTC procedure recommends increasing the distance between the model and the inlet to 10 model lengths and the distance between the outlet and the model to 20 model lengths if significant lift forces are expected [54]. CFD simulations were conducted in order to see if enough lift force was generated to warrant this much larger domain. Two CFD simulations were conducted with the vehicle at a 10.05 degree heading angle, one with the domain size listed in figure 3-2 and one with this significantly larger domain. This provided a means to determine if the forces caused the results to differ between the standard and much larger domain. The surge X and sway Y forces and yawing moment N were only about 0.3% different between the large and small domain so the smaller domain was used to conserve computational resources for future simulations. The following figures show a cross section of the mesh and boundary layer mesh for the angled vehicle simulation.

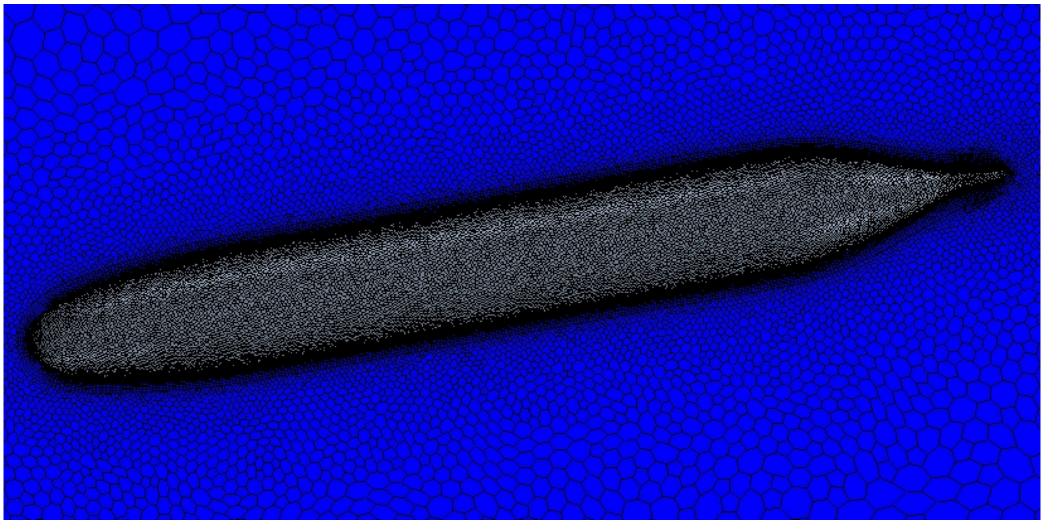

Figure 3-7: Cross section of the mesh used to validate the CFD simulation methods for the angled SUBOFF model.

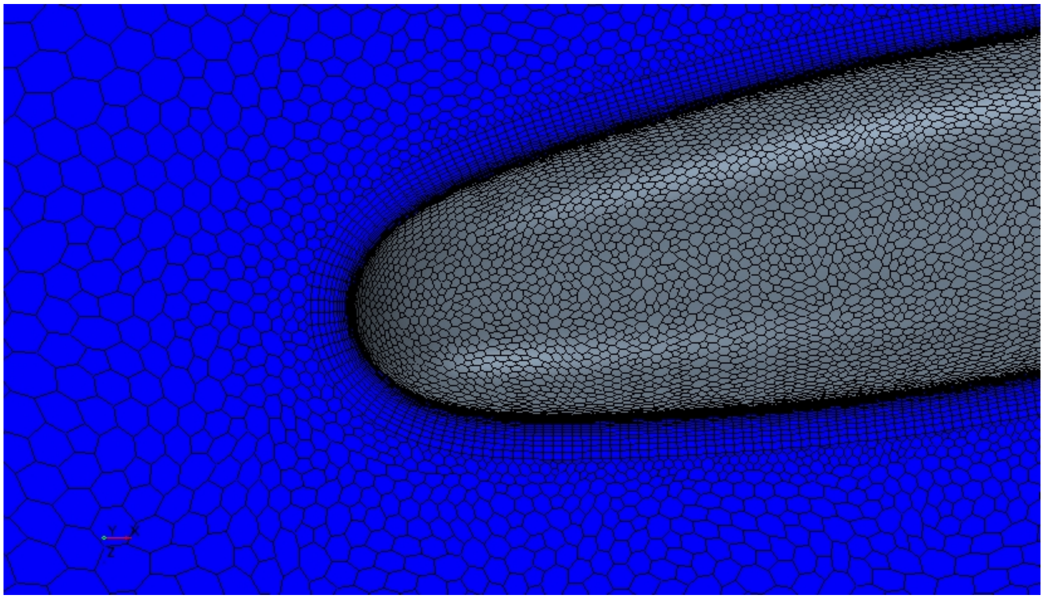

Figure 3-8: Cross section of the boundary layer mesh used to validate the CFD simulation methods for the angled SUBOFF model.

Just like simulations at a zero degree heading angle, the non-dimensional wall distance y^+ for the angled simulations are verified to ensure that they followed the ITTC recommendations. The average y^+ value was about 0.15 with the maximum being 0.202. The figure below shows the y^+ values along the surface of the angled SUBOFF model are within the ITTC requirements.

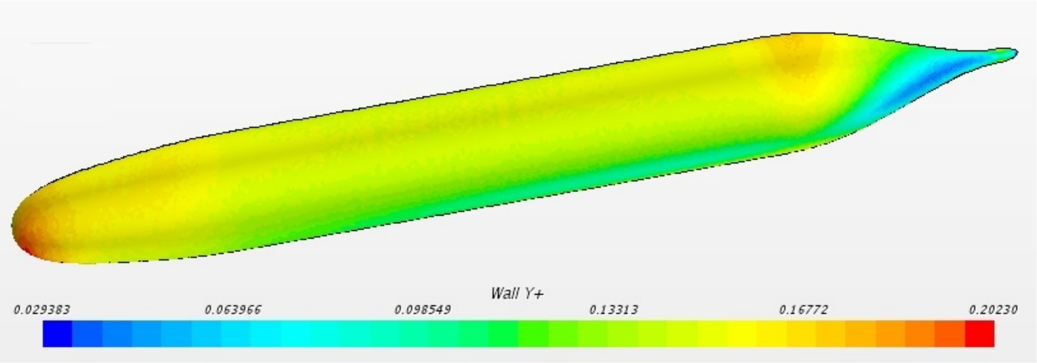

Figure 3-9: Non-dimensional wall distance y^+ across the surface of the SUBOFF model. This meets the requirement of being less than one at each point around the vehicle [54].

3.3.3.5 Results and Validation

Due to the aforementioned symmetry of the CFD simulation domain, the simulation approach is reduced from a 6 DOF system to a 3 DOF system. In this 3 DOF setup, the heave force Z, roll K, and pitch M moments are zero leaving only the surge X, sway Y, and yaw N as non-zero values. Additionally, because the SUBOFF model at a zero degree heading angle is laterally symmetric to the incoming flow, the sway force and yaw moment are both zero. This leaves only the surge force acting on the model. The following table shows the results of the zero degree heading angle SUBOFF CFD simulation compared to published EFD results, including the non-dimensional surge force coefficient (X') [52]. The percent error between the CFD and EFD results is 2.06% which validated that the CFD simulation is able to accurately predict the forces on the zero degree heading angle SUBOFF model. These results are especially important because they validate the ability of the CFD simulation to accurately predict the drag due to skin friction caused by the viscosity of the fluid.

Table 3.1: Validation of CFD against EFD results of a zero degree heading angle SUBOFF model [52].

Model	Speed	CFD X	CFD X'	EFD X	EFD X'	% Error
SUBOFF	3.05 m/s	−85.6 N	$-9.75\text{x}10^{-4}$	−87.4 N	$-9.95\text{x}10^{-4}$	2.1%

The hydrodynamic interactions of a UUV at a non-zero heading angle operating in close proximity to a submarine is a part of the solution space that is yet been explored using EFD [3]. Therefore, validating the forces and moments on a single body submersible at a non-zero heading angle is a critical intermediate step to ensure that the CFD simulation techniques can accurately reflect the results from non-zero heading angles using real-world EFD. Many simulations are performed at different heading angles and validated against published EFD results [51]. The figure below shows the force and moment coefficients at various heading angles ψ.

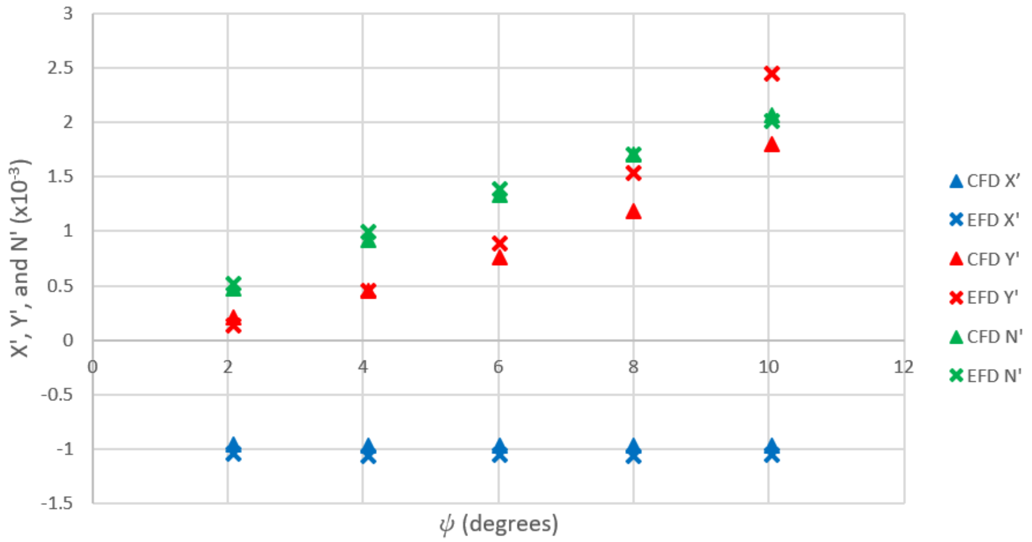

Figure 3-10: Comparison of CFD and EFD results of the surge X', sway Y', and yaw N' coefficients versus heading angle ψ of the SUBOFF model.

Figure 3-10 shows that the CFD simulations of the angled SUBOFF model are validated by the EFD results. The difference between the CFD and EFD results are within single digit percent error with the exception of the sway force coefficient at larger heading angles. The EFD results did not contain any uncertainty analysis for the unappended SUBOFF model, but they provided an approximate margin of error of about 4-10% on other SUBOFF model configurations [51]. Additionally, other literary sources estimate the uncertainty of this EFD data at 10%. This means that the CFD results are within the uncertainty of the EFD specified results [19, 60]. As the heading angle increases, so does the error of the sway coefficient between the CFD and EFD results. This finding is consistent with other results found in literature [48]. Also, a UUV performing L&R operations from a submarine is unlikely to have the UUV at large heading angles because this will cause unwanted rapid movements. For these reasons, this thesis did not further investigate heading angles ψ larger than 10 degrees. Additionally, the percent error of the sway force coefficient Y' at 2.08 degrees is also very large. However, this is much less of a concern because of the small value of the force. The sway force experienced at very shallow angles is close to zero so small errors in the magnitude of the force result in large percent errors. Because the motion of the UUV is dependent on the magnitude of the sway force rather than the percent error, the small total error between the very shallow angle CFD and EFD results is acceptable, even with a larger percent error. The table below shows the percent error of between the CFD and EFD results for each force and moment coefficient.

Table 3.2: Validation of CFD against EFD hydrodynamic coefficients for SUBOFF model at various heading angles [51].

ψ	CFD (x10^{-3})			EFD (x10^{-3})			Error (%)		
(deg)	X'	Y'	N'	X'	Y'	N'	X'	Y'	N'
2.08	-0.962	0.213	0.473	-1.045	0.134	0.517	7.92	59.5	8.52
4.07	-0.964	0.452	0.916	-1.061	0.449	0.996	9.13	0.78	8.04
6.03	-0.966	0.760	1.329	-1.059	0.886	1.385	8.77	14.2	4.06
8.00	-0.968	1.189	1.709	-1.069	1.536	1.708	9.41	22.6	0.08
10.05	-0.966	1.796	2.062	-1.049	2.450	2.008	7.94	26.7	2.67

Overall, the methods used in these CFD simulations are able to accurately predict the forces and moments experienced on a single vehicle at zero and non-zero heading angles. The next step of this thesis is to expand these CFD simulation methods in order to capture the hydrodynamic interactions between two vehicles and validate these multiple vehicle simulations against EFD data.

3.3.4 Multiple Vehicle CFD Simulation

3.3.4.1 Domain

The domain of the CFD simulations with two vehicles is similar to that outlined in section 3.3.3.1. The domain is made symmetric about the plane that intersects the axes of the two vehicles. This means that the forces and moments are simulated on half of the vehicles and then doubled to account for the forces and moments experienced on the full bodies. This allows the domain to be half the size of a domain that does not take advantage of this symmetry. The utilization of this symmetry ultimately reduces the required computational time to run a CFD simulation and allows for a more robust exploration of the surrogate model solution space by enabling more simulations to be performed.

The ITTC guidelines are not tailored for studies involving multiple bodies, but a conservative approach is taken to ensure that the minimum distance between the domain boundaries and vehicles is maintained according to ITTC recommendations [54]. The same domain is used for each simulation, even as the UUV is repositioned for different simulations. The domain is made large enough to account for the appropriate spacing, even as the UUV is repositioned between simulations. The following figure shows the design of the domain for the two vehicle CFD simulations.

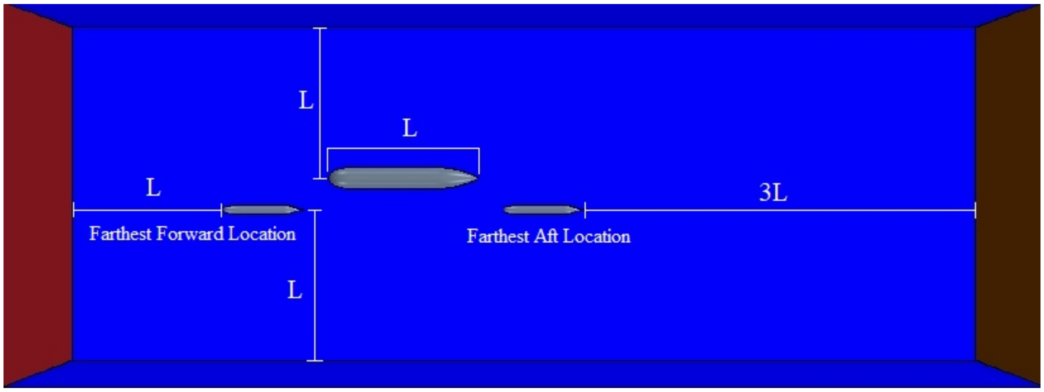

Figure 3-11: CFD domain of the two vehicle simulation. Each wall is at least one vehicle length of separation from the most extreme positions of the UUV, while the outlet boundary is three vehicle lengths of separation.

3.3.4.2 Mesh

The mesh of the CFD simulation is designed to comply with a mesh independence study in the literature in order to ensure that the results are accurate [3]. This mesh independence study shows that at 3.9 million cells and above, the force and moment predictions are within 2% of the finest mesh investigated. This domain did not take advantage of the symmetry of the problem, meaning that the same mesh resolution is reached at about 1.9 million cells for the symmetric domain in this thesis. Also, this mesh independence study is also for a much larger domain than used in this thesis, meaning that a higher resolution mesh is achieved with fewer cells. As such, 1.9 million cells is set as the threshold for the mesh cell count.

This simulation setup uses an unstructured polyhedral mesh because it more easily accommodates mesh deformation and restructuring as the UUV is repositioned between simulations [3]. Once again, the resolution around the Explorer and SUBOFF models is increased by reducing the surface growth rate of the mesh to better capture the flow around the hull. The figure below shows the basic mesh of one of the simulations.

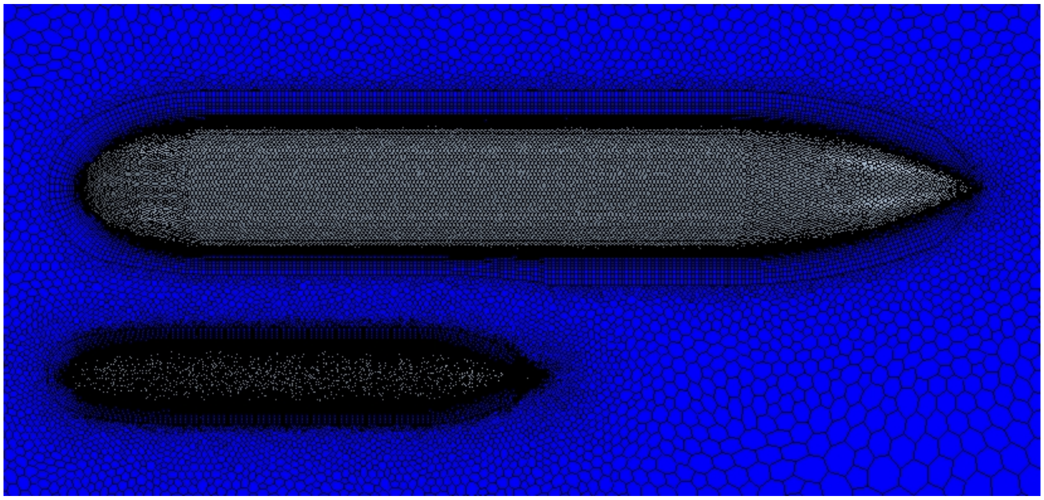

Figure 3-12: Cross section of the mesh used to validate the CFD methods for the two vehicle simulations. This sample mesh is with the UUV located at $R_{Lat} = 0.21$ and $R_{Long} = 0.234$.

3.3.4.3 Boundary Layer and Turbulence Modeling

For the reasons outlined in section 3.3.3.3, these simulations use the k-ω turbulence model because of its accuracy and low computational cost. The boundary layer is developed according to the ITTC procedures [54]. Per the recommendation of the Leong, the total boundary layer thickness is set two twice the Prandtl's turbulent boundary layer thickness outlined in equation (3.10) [3]. This is doubled from that in section 3.3.3.2. The additional thickness of the boundary layer mesh provides a higher resolution mesh farther away from the boundary, which provides a better opportunity for the prism layer mesh to capture the flow in this area of interest. This boundary layer mesh for each vehicle has an expansion ratio of 1.2. The following figure illustrates the boundary layer meshes for the two vehicle simulations.

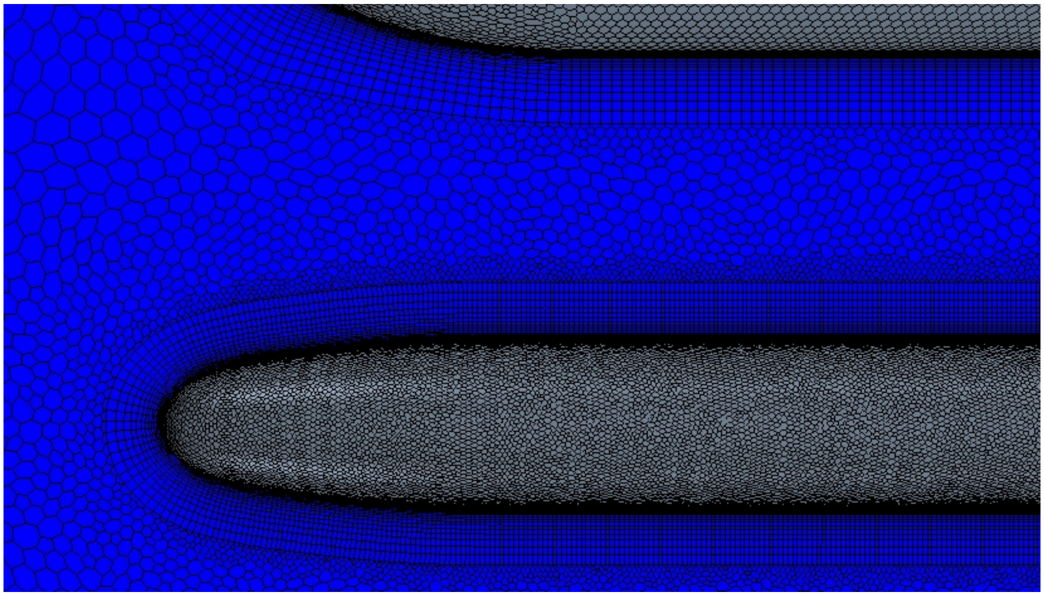

Figure 3-13: Cross section of the boundary layer mesh used to validate the CFD methods for the two vehicle simulations. This sample mesh is with the UUV located at $R_{Lat} = 0.21$ and $R_{Long} = 0.234$.

The non-dimensional wall distance y^+ values along the boundary of the submarine and UUV models are determined in order to ensure that they are less than one in accordance with the ITTC guidelines [54]. The figure below shows that the y^+ values at every point along the boundary of these two models is within these guidelines.

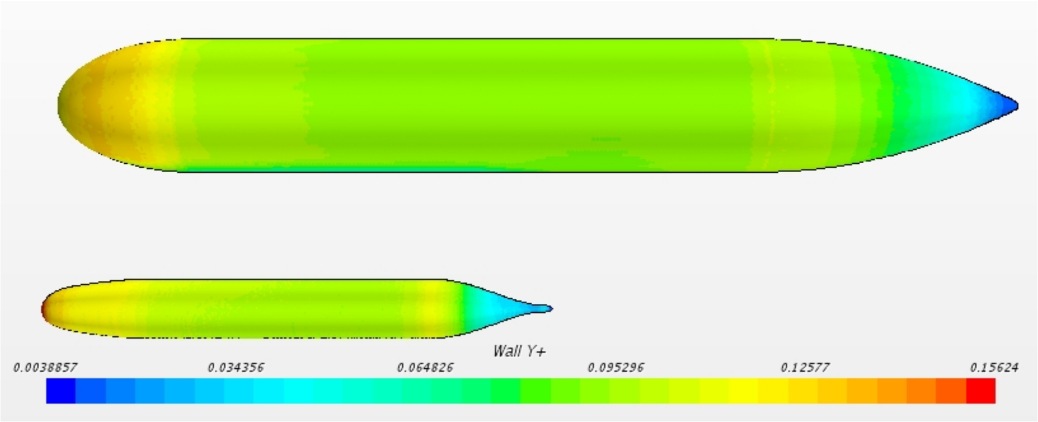

Figure 3-14: Non-dimensional wall distance y^+ across the surface of the two vehicles. This meets the requirement of being less than one at each point around the vehicles [54].

On average, the y^+ value along the model is about 0.1 with a maximum of 0.16.

This meets the ITTC criteria which ensures that the boundary layer thickness on the vehicle is thin enough to allow the k-ω turbulence model to accurately model real-world physics.

3.3.4.4 Results and Validation

The EFD data that could be used to validate these CFD results is very limited. The EFD experiments are performed by Leong at a submarine to UUV diameter ratio of 2.239 and various longitudinal positions [3]. Leong is able to create EFD experiments to measure the surge and sway forces and yawing moment on the UUV. The experimental uncertainty of the study is 2.252$\times$10$-$4 for the surge X' and sway Y' coefficients and 1.446$\times$10 $-$ 4 for the yaw coefficient N'. However, due to the limitations of the physical two tank facilities and model sizes, these EFD results are influenced by the blockage or restricted water effect. The walls of the tow tank are close enough to the models that the presence of the wall limits the ability of the water to flow freely around the models. This has an impact on the measured forces and moments. When Leong performs his CFD simulations, he is able to model the tow tank walls into the domain of his CFD simulations. When accounting for the tow tank walls in the CFD simulations, the CFD is able to accurately predict the measured forces and moments within the experimental uncertainty. In order to determine the forces and moments without the restricted water effects, Leong expands his CFD domain and removes the tow tanks walls from his simulation. By removing the tow tank walls from the CFD studies, the assumption is made that his CFD simulations are still able to capture the real world physics between the submarine and UUV model because no changes are made to this portion of the simulation. As such, Leong's CFD results with no blockage or restricted water effects are considered to be valid. The figure below shows the results of this CFD setup used in this research plotted beside Leong's EFD results. The error bars on Leong's results indicate the experimental uncertainty of his tow tank tests.

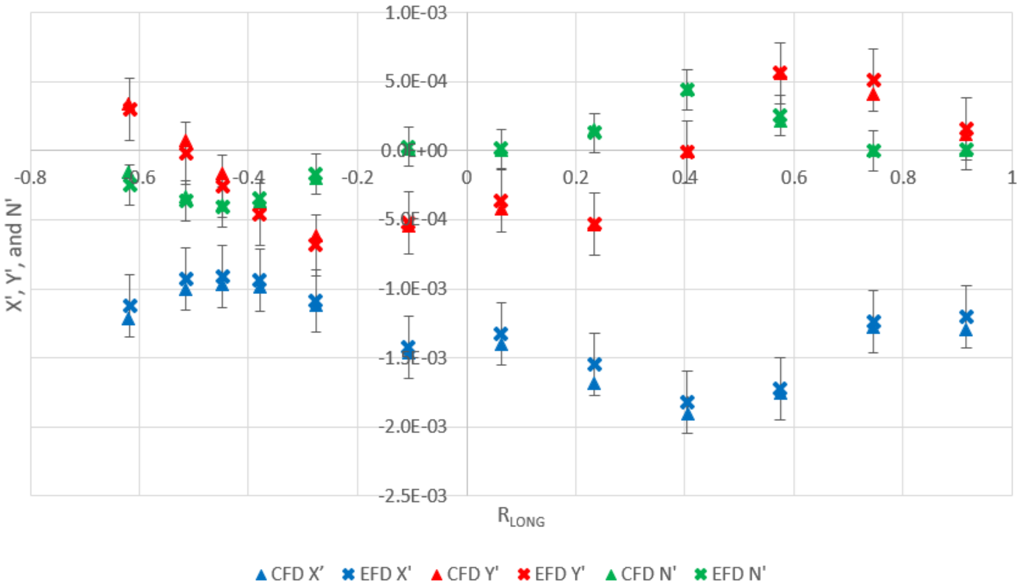

Figure 3-15: Comparison of CFD and EFD results of the surge X', sway Y', and yaw N' coefficients versus longitudinal separation ratio R_{Long} of the two vehicles [3].

As seen in figure 3-15, the CFD results of this study are within the experimental uncertainty of Leong's EFD results. The CFD simulations are able to capture the large degree of change in the hydrodynamic coefficients as the longitudinal position of the UUV is varied. Putting all of this together, the methods and setup of the CFD simulations used in this research are valid across all of the limited available data.

No EFD data is available for experiments where a UUV at a non-zero heading angle is operating in close proximity to a moving submarine. As such, no validation could be performed for this specific set of the CFD simulations explored in this study. However, the CFD results for a single UUV at a non-zero heading angle and the CFD results for a UUV at a zero degree heading angle operating in close proximity to a moving submarine were both validated against EFD data. For this reason, the CFD methods are still assumed to be accurate enough to continue with this research, even though they could not be experimentally validated.

3.4 Potential Flow

3.4.1 Governing Equations

Potential flow is another approach to solving the governing equations (3.7) and (3.6) by making some additional assumptions. In addition to assuming that the flow is incompressible, the flow is also assumed to be inviscid, i.e. $\nu = 0$. Assuming both incompressible and inviscid fluid is often called ideal flow. The last assumption made is that the flow is irrotational, i.e the vorticity $\vec{\omega} = \nabla \times \vec{v} = 0$. This means that a scalar velocity potential function $\phi(\vec{x}, t)$ exists such that $\vec{v} = \nabla\phi$. Substituting this in the continuity equation (3.7) results in the following governing equation for P-Flow.

$$\nabla^2 \phi = 0 \tag{3.11}$$

This reduces the system of governing equations to one equation and one unknown $\phi(\vec{x}, t)$. Once the velocity potential is known, it can be integrated to solve the velocity $\vec{v}(\vec{x}, t)$. Due to the assumptions made about the fluid, the fluid velocity and pressure P are decoupled and dependent so the pressure can be found using the following Bernoulli equation.

$$P = -\rho \left(\frac{\partial \phi}{\partial t} + \frac{1}{2} \left| \nabla \phi \right|^2 + gz \right) + F(\vec{x}, t) \tag{3.12}$$

These P-Flow equations are much simpler and can be solved nearly instantaneously in many cases. However, the fluid assumptions result in well known errors. Potential flow fails to capture any of the viscous drag or flow separation along a non-lifting body moving through a fluid at a constant velocity. This means that P-Flow infamously predicts zero drag on a UUV moving at constant velocity and suggests that the body will perpetually move forward [14]. This is known as the d'Alembert paradox.

In order to overcome this shortcoming, many P-Flow solvers have built-in empirical formulas used to estimate the drag on a vehicle in steady translation. A commercially available potential flow solver known as FS-Flow is used for this research. In order to provide more accurate results, the ITTC-57 parametric equations are selected within the FS-Flow potential flow solver to estimate the drag of the UUV [27].

3.4.2 Results and Validation

In order to validate the potential flow solutions, the same series of P-Flow simulations is run as the CFD simulations for figure 3-10, which is a single body submersible at a non-zero heading angles. Simulations are performed at different heading angles and validated against published EFD results [51]. The figure below shows the force and moment coefficients at various heading angles ψ.

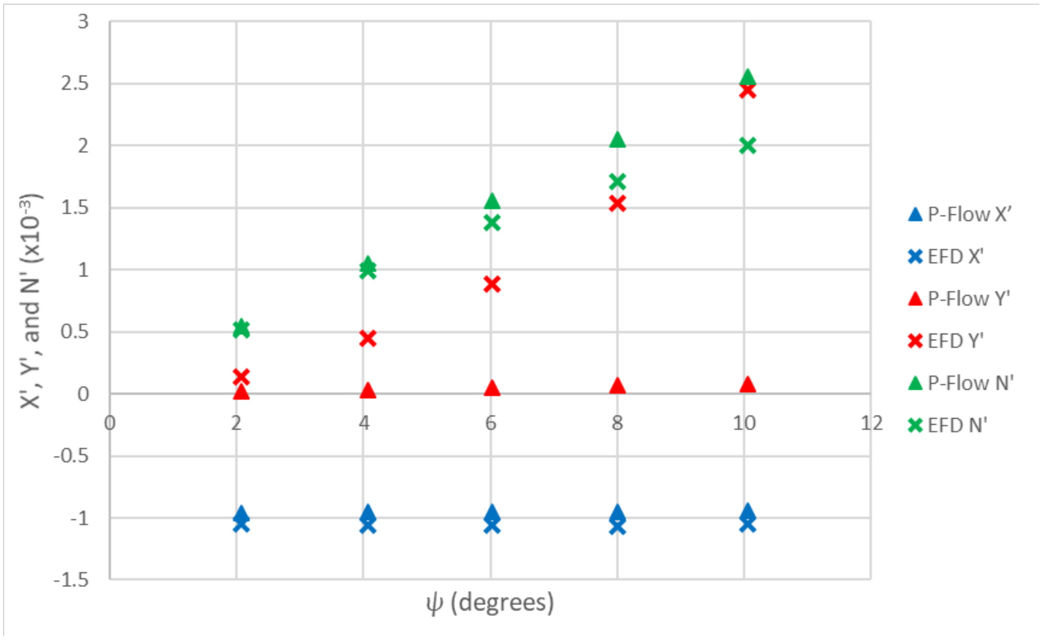

Figure 3-16: Comparison of P-Flow and EFD results of the surge X', sway Y', and yaw N' coefficients versus heading angle ψ of the SUBOFF model.

As seen in figure 3-16, the P-Flow method fails to capture the sway force experienced by the UUV at a non-zero heading angle. Again, this is a demonstration of the d'Alembert paradox and limitation of P-Flow. However, the P-Flow solver does much better at predicting the surge and yaw of the vehicle. The surge is relatively accurate because FS-Flow uses built-in ITTC-57 parametric equations to estimate the drag of the UUV [27]. Additionally, the P-Flow solution tends to slightly over-predict the yaw moment experienced by the vehicle. In P-Flow, this moment is known as the munk moment [14]. The munk moment tends to over-predict the yawing moment on the vehicle because the real vehicle experiences flow separation at its trailing edge. This means there is lower pressure on the trailing edge which results in a lower yawing moment. Overall, the P-Flow results are much less accurate than the CFD simulations shown in figure 3-10. Due to these limitations, P-Flow is not a great candidate to be used to predict the hydrodynamic interactions of a UUV for the purpose of simulation UUV maneuvering. However, when the munk moment dominates the motion of the UUV, sway has negligible impact on UUV motion, and drag can be estimated using parametric equations, P-Flow provides a reasonable means of predicting the forces and moments on a UUV.

3.5 Evaluation of One-Way Assumption

UUV maneuvering simulators have been developed using linearized six DOF equations of motion derived from Newton's second law [15, 61]. These equations determine the surge X, sway Y, and heave Z forces, as well as the roll K, pitch M, and yaw N moments acting on a vessel by determining a series of maneuvering coefficients for the vessel. These coefficients represent the forces and moments as a function of the product of the six DOF linear or angular velocities or their time derivatives. By describing the forces and moments in this way, this enables the maneuvering simulators to model the relationship between the forces and motion of the vehicles by accounting for these coefficients and the vehicle inertial properties, i.e mass, added mass, and moment of inertia. Because of the usefulness of simulating UUV motion in this manner, UUV hulls are routinely analyzed to determine these coefficients. This can be done through EFD, high-fidelity CFD modeling, or low-fidelity boundary element method (BEM) potential flow modeling.

Simplified UUV maneuvering simulations have been developed to predict how UUV motion will be impacted when operating near a moving submarine. These simulators use "one-way" assumptions to simplify this interaction. First off, the simulators determine the flow field around the submarine from the results of a CFD simulation. The figure below shows the velocity profile around a full-sized 34 foot diameter model of the unappended SUBOFF hull moving forward at five knots [49].

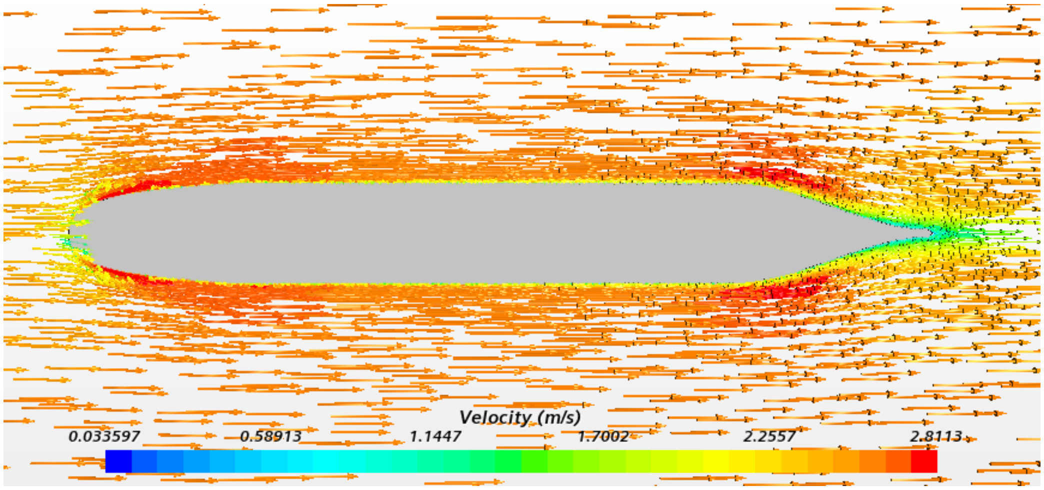

Figure 3-17: Fluid velocity profile around a full-sized 34 foot (10.36 m) diameter model of the unappended SUBOFF hull moving forward at five knots (≈ 2.6 m/s).

This simplified UUV maneuvering simulation approach assumes the UUV will experience the same flow vector shown in figure 3-17 based on its location in the velocity field. This assumption only requires that one CFD simulation needs to be run around the submarine in order to completely resolve the velocity profile around the submarine. The main advantage of the one-way assumption is that it is computationally inexpensive to only run one CFD simulation and use the results to determine the resulting forces on the UUV at any position or heading around the submarine. Because the maneuvering coefficients are known and constant for a given vehicle, the simulator can use the standard equations of motion combined with the velocity profile to simulate how the UUV will be affected by the presence of the submarine. However, the disadvantage of the one-way assumption is that it only accounts for how the presence of the submarine impacts the flow field while neglecting how the presence of the UUV impacts the flow field. The figure below illustrates the flow field of the one-way assumption. The UUV shown is a scaled model of the Explorer AUV that is about the size of a Trident II D-5 missile. This represents the upper end of the UUV size that could fit in a Virginia Payload Tube (VPT) [53, 62].

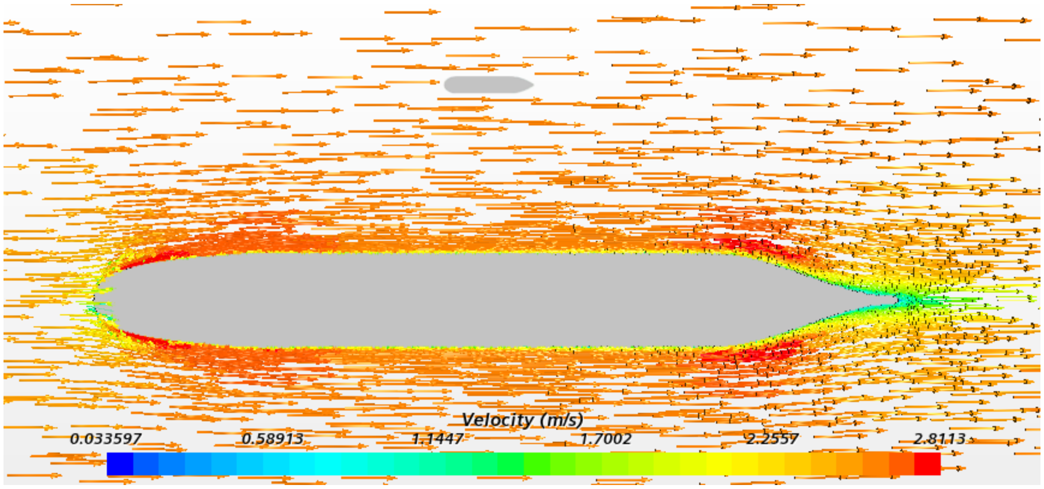

Figure 3-18: Fluid velocity profile of the two vehicles using the one-way assumption. The presence of the UUV has no impact on the fluid velocity profile.

While this one-way assumption allows the UUV motion to be simulated, it neglects how the presence of the UUV itself impacts the flow field and how the resulting forces impact the UUV motion. The fluid velocity profile with no influence from the UUV is illustrated in figure 3-18. This figure shows how the flow slows and moves around the bow of the submarine but not the UUV. When the impact of the UUV on the flow field is taken into account, it captures the real-world physics of the hydrodynamic interaction between the two vehicles. Figure 3-19 shows how the presence of the UUV impacts the flow field compared to the one-way assumption.

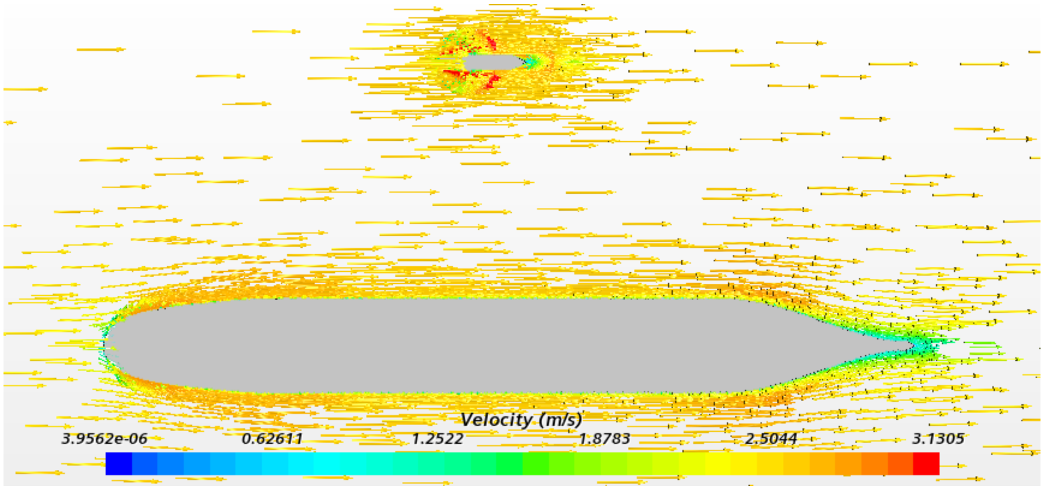

Figure 3-19: Fluid velocity profile of the two vehicles. The presence of the UUV has an impact on the fluid velocity profile compared to the one-way assumption outline in figure 3-18.

As seen in the figures 3-18 and 3-19, the one-way assumption fails to account for the complete hydrodynamic interaction between the two vehicles because it neglects the impact of the UUV in the flow field. In order to determine the real-world hydrodynamic interaction between the two vehicles, a new CFD simulation needs to be performed each time that the UUV changes position, heading, or speed. Because CFD simulations are computationally expensive, they cannot be solved in real-time nor can enough simulations be run to completely resolve the possible domain of all UUV positions, headings, and speeds. This is the major hurdle that has prevented the real-world hydrodynamic interactions from being incorporated into UUV motion simulators. This makes the one-way assumption one of the only techniques to model hydrodynamic interactions in UUV simulators, but this approach often leads to significant errors and inaccurate UUV motion simulations.

There are many instances when this one-way assumption may be appropriate. In the example above, the UUV is laterally far enough away from the submarine that the flow between the vehicles is relatively unobstructed. The impacts of the flow obstruction near the UUV does not reach the submarine. When the UUV is positioned close enough to the submarine that the flow around the UUV is influenced by the submarine, this results in real-world hydrodynamic interactions that the one-way assumption fails to predict. Figure 3-20 shows how the velocity field is impacted when the UUV moves close to the submarine.

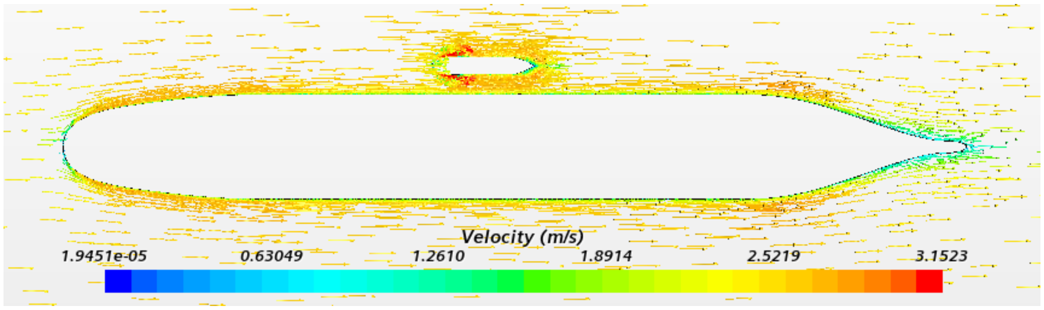

(a) Fluid velocity profile around the submarine with the UUV operating close to its parallel mid-body section.

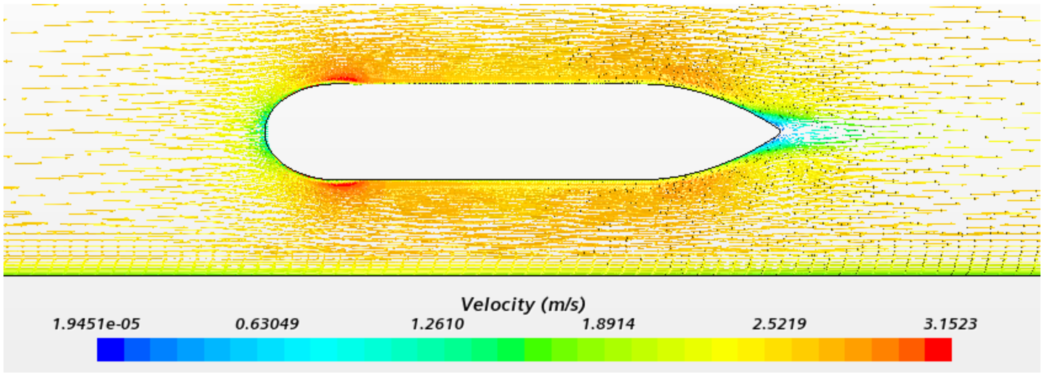

(b) Fluid velocity profile around the UUV operating close to the parallel mid-body section of the submarine.

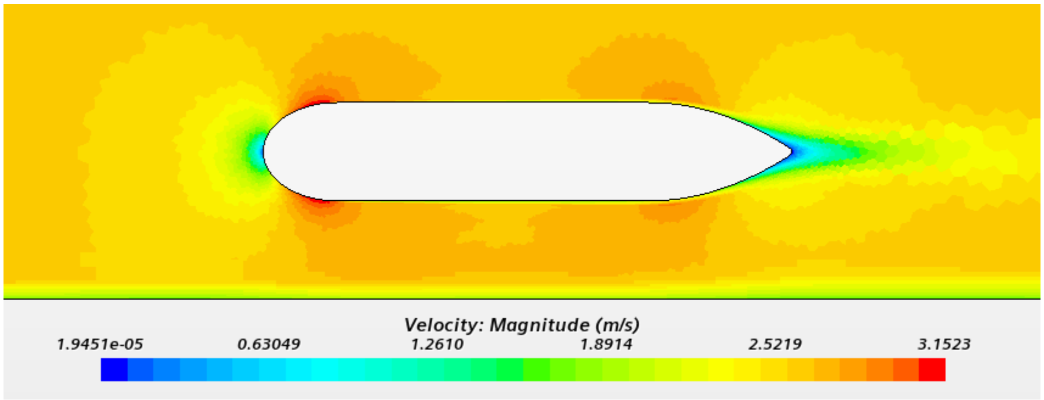

(c) Magnitude of the fluid velocity around the UUV operating close to the parallel mid-body section of the submarine.

Figure 3-20: Fluid velocity profile of the UUV operating close to the submarine near the parallel mid-body. The flow around the UUV is influenced by the presence of the submarine.

As seen in figure 3-20, more of the flow between the UUV and the submarine is at a higher velocity than the region on the opposite side of the UUV. This is often referred to as the restricted water effect. Because the region between the submarine and UUV has a more restricted area than competing flow paths, the flow acts differently than if the submarine were not present. In this case, the flow between the vehicles is faster in order to maintain continuity through a smaller area. Due to the Bernoulli effects, this higher velocity flow causes a lower pressure region between the vehicles which results in a sway force that sucks the UUV toward the submarine. This sway force is not captured using the one-way assumption.

Additionally, the flow in this region along the parallel mid-body of the submarine is relatively uniform, just like when the maneuvering coefficients are determined for a UUV. When the flow becomes non-uniform, as it does near the bow and stern of the submarine, this causes different portions of the UUV to experience different flow velocities. This non-uniform flow also causes the one-way assumption to break down and become inaccurate. The following figure is an example of where the UUV is near the bow of the submarine. In this position, the UUV experiences a non-uniform flow.

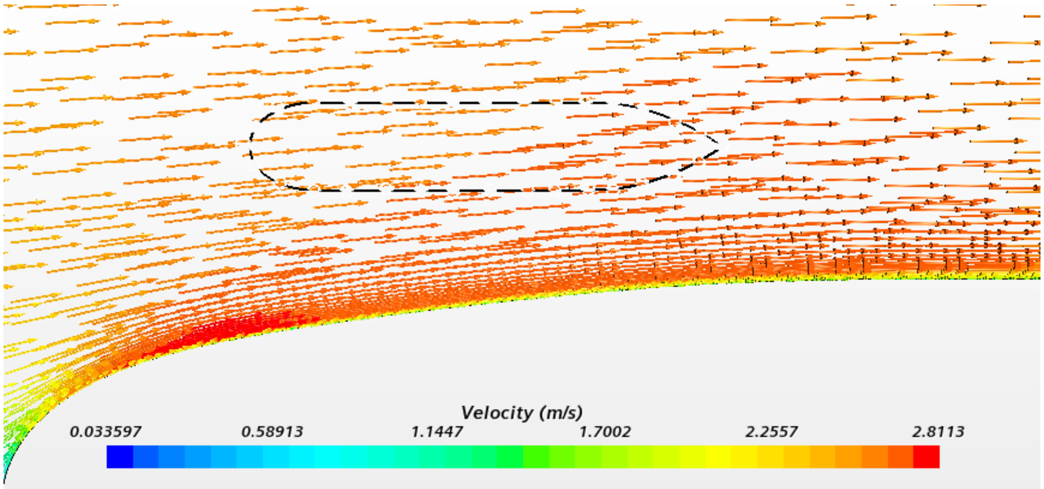

(a) Fluid velocity profile around the bow of the submarine. If the UUV is present, it experiences a non-uniform flow.

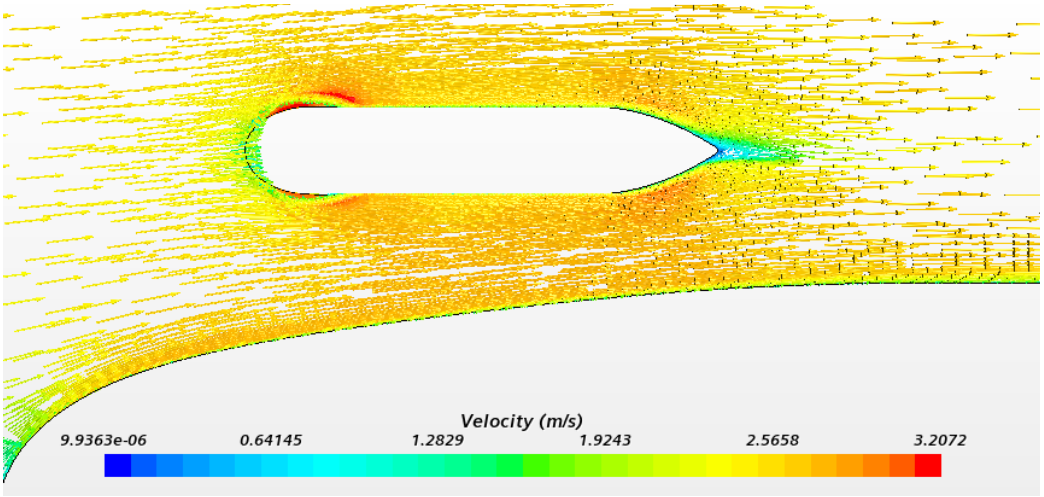

(b) Fluid velocity profile around the UUV operating near the bow of the submarine.

Figure 3-21: Fluid velocity profile of the UUV operating close to the submarine bow. The non-uniform flow and restricted water effects cause inaccuracies using the one-way assumption.

Figure 3-21 shows how the flow around the bow of the submarine is highly non-uniform. Flow velocity varies in both magnitude and direction based on the location of the flow around the bow of the submarine. If a UUV is to be positioned in the region outlined above, the bow of the UUV would experience a more tangential and slower velocity than the stern of the UUV due to how the flow moves along the bow of the submarine. Because the one-way assumption only accounts for a uniform flow, this will not be able to account for how the bow and stern of the UUV will experience different forces than if the flow is uniform. In order to illustrate the potential breakdown of the one-way assumption, a few example cases are analyzed. In each case, the surge force coefficient X', sway force coefficient Y', and yawing moment coefficient N' of the UUV are determined using CFD for both the one-way assumption and the unassumed hydrodynamic interaction. Figure 3-22 shows the different positions of the UUV for each case.

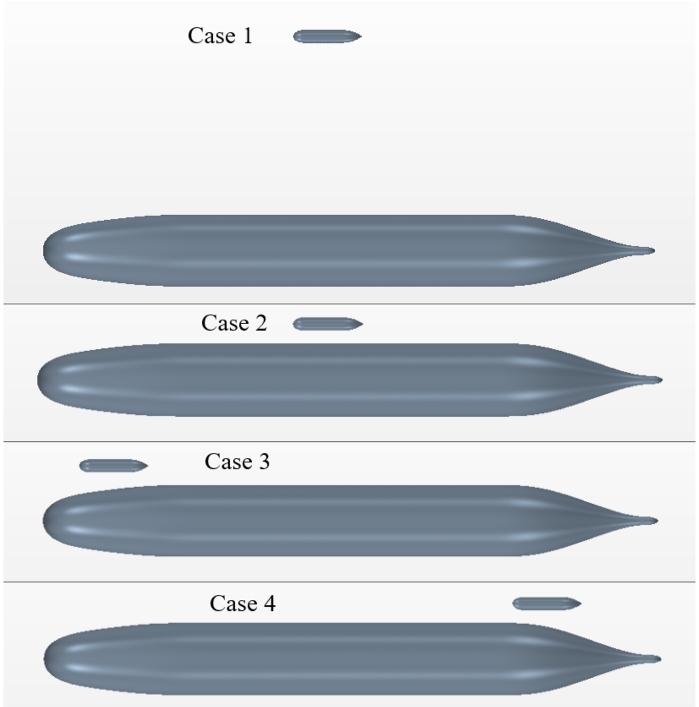

Figure 3-22: These four cases are used to evaluate the accuracy of the one-way assumption.

Table 3.3 lists the results of the one-way assumption method and the unassumed CFD simulation of the hydrodynamic interactions for the different cases outlined in figure 3-22. This table also provides the percent error of the one-way assumption from the unassumed hydrodynamic interaction.

Table 3.3: Comparison of the one-way assumption against the unassumed CFD hydrodynamic interactions.

Case	One-Way Assumption (x10^{-4})			CFD Hydrodynamic Interaction (x10^{-4})			Error (%)		
	X'	Y'	N'	X'	Y'	N'	X'	Y'	N'
1	-16.55	0.015*	0.119	-16.59	-0.857*	0.083	0.2	102*	44.5
2	-16.54	0.162*	0.369	-16.91	-4.289*	0.441	2.2	104*	16.4
3	-16.44	7.926*	20.60	-28.95	-18.77*	21.12	43.2	142*	2.5
4	-16.41*	-10.21	-25.64	8.741*	-54.87	-30.69	288*	81.4	16.5

* Denotes a change in direction of force between the two methods

The one-way assumption shows significant error in most of these cases. While case one has a large percent error in the sway force coefficient between the two methods, the magnitude of this force is relatively small so the actual motion of the UUV would not be as large as the percent error suggests. In the other cases, the percent error is very large while the magnitude of the force is also large, indicating that the difference between the UUV motion simulation using these two methods would be substantial. In many instances, the actual forces experienced by the UUV when accounting for the complete hydrodynamic interactions are an order of magnitude higher than the one-way assumption results. Not only are there large differences between these two methods, but they also frequently differ in direction, especially for sway. This means that in many circumstances, the one-way assumption would instruct the UUV to steer the rudder in one direction to overcome the impact of the flow around the submarine to stay on course while the actual hydrodynamic interaction would dictate the rudder move in the opposite direction. This provides problems for developing accurate launch and recovery simulations using the one-way assumption. In summary, by using a one-way assumption, only one CFD simulation is needed in order to completely determine the flow field around the submarine and create a UUV motion simulator. This greatly reduces the computational requirements to simulate UUV maneuvering near a submarine, but this assumption fails to model the real-world physics. To capture the actual hydrodynamic interactions between the UUV and submarine, a CFD simulation needs to be performed every time that the UUV is repositioned or reoriented. This has been the major hurdle as to why these effects have not been implemented into UUV maneuvering simulators. An infinite number of CFD solutions would be required to completely resolve the maneuvering space. One approach could be to create a library of CFD simulations that allow the UUV maneuvering simulator to look up a required solution. However, the computational effort to create a library of the necessary size to saturate the maneuvering space is unfeasible. Another approach could be to reduce CFD computational times to near real-time. UUVs go through their control loops feedback cycles multiple times per second. This means that CFD simulation times would need to be reduced from days to fractions of a second in order for this approach to be viable. This greatly exceeds the computational capacity of the hardware that can be stored on a UUV. Overall, the hydrodynamic interactions between these two vehicles need to be determined in real time in order to incorporate them into a UUV maneuvering simulator. Using machine learning to bridge this capability gap provides the most promising approach to this problem.

3.6 Conclusion

Using CFD to computationally model the hydrodynamic interactions between a submarine and UUV is a valid approach. When setting up a CFD simulation, there are many variables that need to be correctly selected in order to receive a valid result. Some of these include domain size, mesh resolution, boundary layer resolution, and various turbulence models. The CFD simulations are set up using ITTC guidelines and validated against real-world EFD tow tank experiments. The CFD is able to accurately predict the forces and moments on the real-world UUV in all of the different scenarios in which EFD validation data is available. This includes zero-degree heading angle single body UUV, non-zero degree heading angle single body UUV, and hydrodynamic interactions between a UUV and submarine. While the CFD setup has been validated, it is still much too expensive to be evaluated in real time in order to be incorporated into a UUV maneuvering simulator.

Potential flow is unable to accurately capture all of the desired forces and moments experienced by the UUV. For P-Flow, the munk moment from the potential flow results is reasonably close to the actual yawing moment of the UUV at small heading angles. Likewise, the ITTC-57 parametric equations can supplement P-Flow to predict the vehicle surge quite accurately. However, the P-Flow results are unable to capture the sway force of the UUV at small heading angles due to the d'Alembert paradox.

The one-way assumption is when the velocity profile around the submarine is completely resolved using CFD as if the UUV is not present. Next, this profile is used to predict the hydrodynamic interactions by determining the forces and moments on the UUV as if it is only experiencing this flow with no other hydrodynamic influences. This assumption produces errors that make it a poor candidate to computationally model the hydrodynamic interactions in real time for the purpose of UUV maneuvering simulation.

THIS PAGE INTENTIONALLY LEFT BLANK

Chapter 4

Reduced Order Modeling of Hydrodynamic Interactions between a UUV and Submarine

4.1 Introduction

Several efforts have been dedicated to predicting the hydrodynamic interaction forces and moments experienced by a UUV as it operates near a moving submarine [3, 19, 63, 13]. However, there is no method at the moment that allows for real-time computational modeling of all the complex hydrodynamic interaction forces and moments that a UUV experiences at different positions and orientations around the submarine. This real-time modeling of these hydrodynamic interactions is essential to simulate the motion required to launch and recover UUVs from submarines. UUV control and autonomy systems iterate multiple times a second in order to adjust the control surfaces and thrust of the vehicle based on its updated position, heading, and speed. Potential flow models are often fast enough to be used in real time, but lack the accuracy of CFD simulations, which often take hours or days to solve. The goal of this thesis is to overcome this technological gap by developing a reduced order model

(ROM) capable of predicting the UUV and submarine hydrodynamic interactions in real time using a very small number of carefully selected CFD simulations.

This chapter explains the experimental design of the ROM beginning with selecting which inputs are used to develop the surrogate model. Next, a detailed account of how the Gaussian Process (GP) regression model and non-myopic multi-fidelity (NMMF) active learning algorithm are used . This chapter concludes with the results of the ROM output, including the generation of force and moment maps, comparison to known tow tank hydrodynamic interaction results, and validation of the ROM against test data.

4.2 Input Variables

In order to simulate the motion of the UUV, a body-fixed coordinate system is established at the center of buoyancy of the UUV. The surge, sway, heave, roll, pitch, and yaw velocities and forces/moments are defined as u, v, w, p, q, r and X, Y, Z, K, M, N respectively. The position of the UUV is expressed in the inertial reference frame using x, y, and z. Likewise, the roll, pitch, and yaw angles are denoted as ϕ, θ, and ψ. The distances between the center of buoyancy and the center of gravity of the UUV in the three principle directions are defined as x_g, y_g, and z_g. This coordinate system is illustrated in figure 5-1.

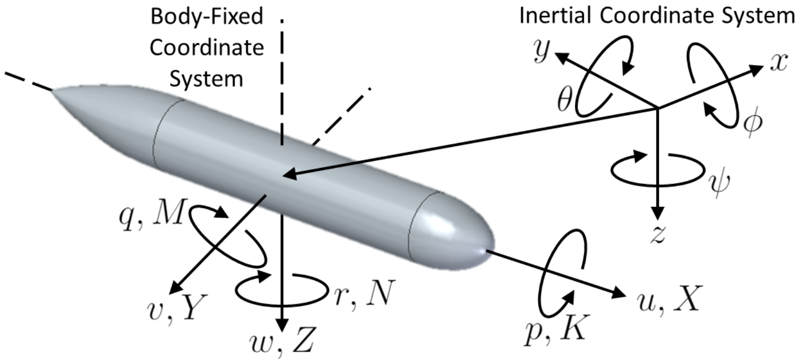

Figure 4-1: Orientation of UUV body-fixed and inertial coordinate systems with their corresponding velocities, forces, and moments [64]

.

UUV maneuvering simulators uses three different vectors to relay information between modules within the simulator. These three different vectors are the state vector $\mathbf{x}$, input vector $\mathbf{u}$, and desired state vector $\mathbf{x_d}$ and are listed in equation (5.1). The propeller thrust and torque are denoted as X_{Prop} and K_{Prop} respectively while the rudder and stern plane angles are denoted as δ_r and δ_s respectively.

$$\begin{aligned} \mathbf{x} &= [u, v, w, p, q, r, x, y, z, \phi, \theta, \psi]^T \\ \mathbf{u} &= [X_{Prop}, K_{Prop}, \delta_r, \delta_s]^T \\ \mathbf{x_d} &= [u_d, z_d, \psi_d]^T \end{aligned} \tag{4.1}$$

Existing UUV maneuvering simulators use the vectors in equation (4.1) to simulate the UUV closed-loop autonomy and control system and its impact on UUV motion [64, 65, 66]. Simulators use an autonomous behavior module which takes the state vector of the UUV at a given point $\mathbf{x_t}$ as an input and returns the desired state vector $\mathbf{x_{d,t}}$ containing the UUV desired speed, desired depth, and desired heading. This desired state vector is fed into the control module which uses control theory to determine the input vector $\mathbf{u_t}$ containing the appropriate propeller thrust and control surface angles. This input vector and the state vector is then fed to the physics module which uses the equations of motion to determine the new UUV state vector $\mathbf{x_{t+1}}$. This loop is iterated along small time steps to simulate the UUV motion.

The UUV simulators take the state vector and input vector as inputs and use non-linear maneuvering coefficients, i.e. hydrodynamic derivatives, to determine the forces and moments acing on the UUV [15, 64, 65, 66]. These forces and moments are then used in the equations of motion in order to determine the new state vector of the UUV. In order to easily be incorporated into the UUV simulators, the surrogate model also takes the same state vector as an input and return the hydrodynamic interaction forces and moments as an output. This means that the input dimension of the surrogate model relies on the state vector.

Many UUV simulations make simplifications to their state vector because it reduces the complexity and cost of both running simulations and experimentally determining maneuvering coefficients. Likewise, using fewer input dimensions to the surrogate model reduces the number of CFD simulations that need to be performed for training data. For this reason, simplifications are made to the surrogate model to reduce its dimensionality.

4.2.1 Three Degree of Freedom Simulation

Many simplifications are made to the UUV simulators to reduce the effort needed to determine all of the hydrodynamic coefficients and focus efforts on improving the simulation in the most relevant dimensions [15, 64, 66]. The full six DOF of surge, sway, heave, roll, pitch,and yaw are reduced to three by removing the that roll, pitch, and heave dimensions. Because many UUVs have similar geometry in the xy and xz plane, the heave and pitch results are the same as the sway and yaw results [64]. This means that the effect of heave and pitch can often be determined utilizing symmetry of sway and yaw rather than increasing the dimension of the simulation. Roll is also removed from the UUV simulator due to vehicle symmetry and how UUVs have no control surfaces that account for roll only [64, 66]. These simplifications drastically reduce the effort to model submarine and UUV hydrodynamic interactions while still capturing the fundamental behaviors and capabilities. The planar motion for this three DOF setup is the plane that contains both vehicle axes. For the purposes of this thesis, the inertial coordinate system is fixed to the center of bouyancy of the submarine with the bow of the submarine pointing along the positive x-axis. The UUV body-fixed coordinate system is positioned such that a positive sway v and heading angle ψ means the UUV is moving away from or rotated with its bow away from the submarine. Reducing from a six DOF to a three DOF simulation reduces the state vector to the following set of states.

$$\mathbf{x} = [u, v, r, x, y, \psi]^T \tag{4.2}$$

4.2.2 Quasi-Static Simulation

As the UUV changes position, heading, and speed, it experiences different forces and moments due to the hydrodynamic interactions between the vehicles. For this study, terms from the simplified state vector in equation (4.2) are used as inputs to the GP regression model. This allows the surrogate model to predict the hydrodynamic interactions based on changes to the UUV state vector. The x and y terms are non-dimensionalized by the submarine length L_{Sub} to in order to determine lateral and longitudinal separation ratios R_{lat} and R_{long} as shown in equations (3.4) and (3.3) and figure 3-1.

In this UUV simulation and ROM approach, the inertial reference frame is fixed to the center of buoyancy of the submarine which is moving at a constant speed through the water. This fluid flow through the inertial frame caused by the submarine moving forward can be thought of as a current in a traditional earth-fixed inertial frame. Because of this flow, the sway velocity v and the heading angle ψ are not independent. This flow means that a non-zero heading angle in the inertial frame results in a non-zero sway velocity in the UUV body-fixed reference frame, if the UUV is is in a near steady state. This relationship is valid for small heading angle differences from the flow direction because the sway velocity is so much smaller than the UUV surge velocity or submarine velocity and the heading angle has such a large impact on the sway velocity. This type of setup is referred to as quasi-static because the forces and moments exerted on the UUV for the dynamic simulation are determined by simulating the UUV in a steady state i.e. there is no transient or unsteady behaviour used in the CFD simulations so only steady CFD simulations are performed. Quasi-static approaches have been found to be accurate because these transients are relatively small so they have little impact on the hydrodynamic interactions [3, 13]. In order to analyze UUV transient behaviors, unsteady CFD simulations would need to be performed. These are much more computationally expensive and there is no EFD data against which the CFD simulations can be validated. As such, the ROM only needs to account for the heading angle and not the redundant sway velocity to model the hydrodynamic interactions. Recognizing this dependence allows the input dimension of the surrogate model to be reduced which decreases the number of CFD simulations that need to be run in order to train the model. This allows for a more accurate ROM given a fixed amount of computational resources.

For the same reason, the yaw rate r is not used as an input to the surrogate model. Because a UUV is near parallel to the submarine during launch and recovery operations with no rapid heading changes, the yaw rate is very small compared to other terms and has negligible impact on hydrodynamic interactions. Not including this input in the surrogate enables the same quasi-static assumption which allows the CFD simulations to be steady rather than unsteady. Again, this drastically simplifies the CFD simulation complexity, decreases the simulation computational time, and reduces the number of simulations needed to explore the domain. Overall, by removing the sway velocity v and yaw rate r as inputs to the ROM, the overall dimensionality of the surrogate is reduced to four for a single UUV.

4.2.3 Domain of Input Variables for Surrogate Model

Rather than creating a surrogate model for one specific UUV, this surrogate model is designed to account for different lengths and diameters of the UUV. This allows the hydrodynamic interactions between different size UUVs to be explored, rather than limiting the research to a UUV of one size. This enables better exploration of launch and recovery options and capabilities for different size UUVs. The diameter of the UUV is non-dimensionalized with the submarine diameter. This is called the submarine-to-UUV diameter ratio D_{Sub}/D_{UUV}. The length of the UUV is non-dimensionalized by the diameter of the UUV and is known as the UUV length-to-diameter ratio L/D_{UUV}. By adding these two input dimensions to the ROM, the surrogate becomes six dimensional. In summary, the six inputs to the ROM are the longitudinal separation ratio, lateral separation ratio, UUV speed, UUV heading angle, submarine-to-UUV diameter ratio, and the UUV length-to-diameter ratio.

Once the input variables to the ROM are established, the next step is to establish the bounds on these inputs. Each input variable has its own unique domain based on different criteria. The following list provides the rationale for the bounds on the domain of each input variable.

- *Longitudinal separation ratio* - In a previous ROM attempts, the bounds of this variable were set between -1.5 and 1.5 [67]. These bounds were based on the results of the hydrodynamic interaction forces and moments study from Leong [3]. However, because real world UUVs are much smaller than those studied by Leong, this domain was much larger than necessary. This meant that many CFD simulations were performed beyond the region where hydrodynamic interactions occur, which is a waste of computational resources. As such, the bounds for this ROM are set between -0.7 and 0.7 to ensure that CFD simulations better capture the hydrodynamic interactions.

- *Lateral separation ratio* - Just like the longitudinal separation ratio, the domain is reduced from a previous study of larger UUVs. The domain of the lateral separation ratio is reduced from between 0.064 and 0.65 down to between 0.059 and 0.105 in order to enable the ROM to more accurately model the hydrodynamic interactions. Focusing on areas closer to the submarine also makes the study more relevant to the L&R of UUVs.

- *UUV speed* - The speed of the UUV is varied between 2 and 5 knots ($\approx$1.03 and $\approx$2.57 m/s). These bounds are based on the maximum speed attainable by most commercially available UUVs and the minimum speed at which submarines are operated to maintain controllability [53, 19, 68, 69, 70, 71, 72].

- *UUV heading angle* - The heading angle is defined as the angle between the UUV and the axis of the submarine, i.e. the x-axis of the inertial coordinate system. A positive heading angle denotes the bow of the UUV is pointed away from the submarine. Previous efforts set the bounds of the heading angle between -10 and 10 degrees [67]. However, the magnitude of the forces and moments at these large angles resulted in inaccuracies. This is because these large angles resulted in much larger forces and moments than caused by the hydrodynamic interactions at zero degree heading angles. The error inherent in the CFD data became large compared to the magnitude of hydrodynamic interactions. This low "signal-to-noise ratio" meant that the ROM spent computational resources trying to resolve the aleatoric uncertainty of the data at large heading angles rather than reduce the epistemic uncertainty across the domain to resolve the hydrodynamic interactions. Additionally, these forces and moments at large heading angles are large enough that they make successful UUV L&R operations unlikely. As such, the domain of the heading angle is reduced to be between -2 and 2 degrees.

- *Submarine-to-UUV diameter ratio* - The following table shows a compilation of different UUV sizes taken from various sources [53, 19, 69, 70, 71, 72]. The UUV diameters are non-dimensionalized by the Virginia class and Ohio class submarine diameters.

Table 4.1: Different UUV sizes including the submarine-to-UUV diameter ratio and the UUV length-to-diameter ratio [53, 19, 69, 70, 71, 72].

Size	Name	Length (m)	Diameter (m)	L/D_{UUV}	D_{Sub}/D_{UUV} (Virginia)	D_{Sub}/D_{UUV} (Ohio)
S	REMUS 100	1.60	0.19	8.42	54.53	67.37
M	REMUS 600	3.25	0.32	10.03	31.98	39.51
L	REMUS 6000	3.84	0.71	5.41	14.59	18.03
L	HUGIN 1000	4.50	0.75	6.00	13.81	17.07
L	HUGIN 3000	5.50	1.00	5.50	10.36	12.80
L	HUGIN 4500	6.00	1.00	6.00	10.36	12.80
S	Sandshark	1.09	0.12	8.79	83.55	103.23
M	Bluefin 12	3.00	0.33	9.09	31.39	38.79
M	Bluefin 21	3.30	0.53	6.23	19.55	24.15
M	Knifefish	5.80	0.53	10.94	19.55	24.15
M	62 Sapphires	7.00	0.53	13.21	19.55	24.15

L	Autosub	7.00	0.90	7.78	11.51	14.22
S	IVER3	1.52	0.15	10.37	70.48	87.07
L	Explorer	5.36	0.74	7.24	14.00	17.30
L	Snakehead	5.25	1.22	4.30	8.49	10.49
L	VPT*	10.00	2.13	4.69	4.86	6.01

*Represents the maximum UUV size that could fit in the Virginia payload tube

In order to account for the vast majority of these submarine-to-UUV diameter ratios without spending lots of resources chasing outliers, the bounds of this parameter are set from 5 to 50.

- *UUV length-to-diameter ratio* - Table 4.1 shows various different L/D_{UUV} ratios. The bounds of this variable is set from 4.3 to 13 in order to reflect the various UUV designs.

Table 4.2 summarizes each of the six different input variables with their accompanying units and bounds.

Table 4.2: Input variables and domains for hydrodynamic interaction reduced order model

Symbol	Description	Units	Bounds
R_{Long}	Longitudinal separation ratio	None	[-0.7,0.7]
R_{Lat}	Lateral separation ratio	None	[0.059,0.105]
u	UUV speed	Knots	[2,5]
ψ	UUV heading angle	Degrees	[-2,2]
D_{Sub}/D_{UUV}	Submarine-to-UUV diameter ratio	None	[5,50]
L/D_{UUV}	UUV Length-to-diameter ratio	None	[4.3,13]

As certain bounds are increased, the magnitude of the forces and uncertainty of the CFD simulations becomes relatively large in some parts of the domain. This phenomena exemplifies the trade-off between exploration and accuracy. Exploring a large domain reduces the ability of the model to accurately capture complex hydrodynamic interactions, while having a small domain more accurate model may be to restrictive to be useful. The bounds of this domain are selected to capture the wide range of input variables necessary to simulate UUV motion while being restrictive enough to produce accurate results.

4.3 Constraints

While the selection of the size of the input domain considers the trade-off between accuracy and exploration, additional constraints are established to exclude certain unrealistic or unfeasible parts of the domain based on input variable interactions. For example, larger diameter UUVs tend to be shorter while smaller diameter UUVs tend to be longer. Two constraints are created based on real-world UUV measurements which ignore the combination of UUV lengths and diameters that are infeasible. Additionally, the relationship between lateral distance from the submarine and the UUV diameter is constrained. This enables the center of buoyancy of the small diameter UUVs to get closer to the submarine than a larger diameter UUV. If the input variables with the given bounds are varied without constraint, the submarine and UUV could overlap in the extreme parts of the domain, creating an infeasible simulation. Likewise, UUVs are constrained, based on diameter, to make sure they are not so far away as to avoid any hydrodynamic interactions. In total, four different constraints are established to remove infeasible regions of the domain and focus the ROM to explore the most relevant regions of the domain in order to improve its accuracy.

A lateral constraint is established to allow the UUV to get very close to the submarine for simulations. The necessity of a constraint could be avoided by reducing the domain so all UUVs are farther away. However, because the UUVs vary significantly in size, this wouldn't allow the small UUVs to be as close as is desired. Therefore, a lateral constraint is established that ensures there is clearance c between the vehicles as illustrated in figure 4-2.

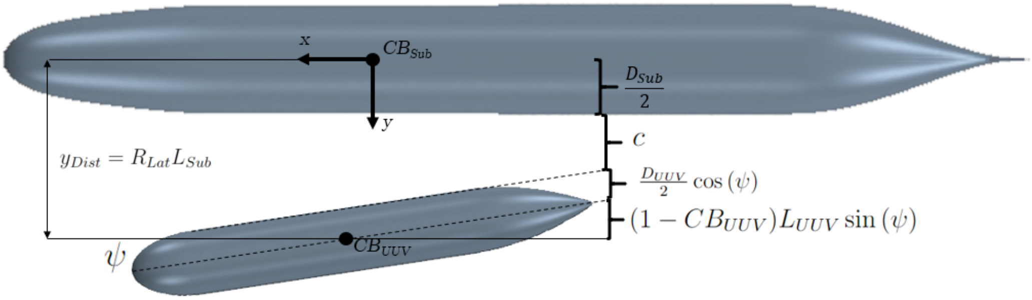

Figure 4-2: The ROM model is constrained to ensure that there lateral distance between the vehicles is far enough away to maintain a clearance.

As shown in figure 4-2, the clearance between the two vehicles can be found using the following equation.

$$c = R_{Lat}L_{Sub} - \frac{D_{Sub} - D_{UUV}\cos(\psi)}{2} - (1 - CB_{UUV})L_{UUV}\sin(\psi) \tag{4.3}$$

Rather than make the lateral constraint dependent on sinusoidal functions of one of the input variables, the maximum heading angle ψ_{max} is used to establish the clearance along with the small angle assumption $\sin(\psi) \approx \psi$ and $cos(\psi) \approx 1$ to simplify the expression. Additionally, the minimum clearance between the two vehicles is set such that $c \geq 0.05$ meters. The submarine dimensions from section 4.1 are substituted into equation (4.3) and non-dimensionalized in order to construct the following constraint in terms of the input variables in table 4.2.

$$8.575R_{Lat} - 0.5\left(\frac{D_{Sub}}{D_{UUV}}\right)^{-1} - 9.425\cdot 10^{-3}u\left(\frac{D_{Sub}}{D_{UUV}}\right)^{-1}(L/D_{UUV}) - 0.5048 \geq 0 \tag{4.4}$$

Likewise, another constraint is used in order to ensure that the UUVs are close enough to the submarine to experience a hydrodynamic interaction. If the UUVs become too laterally separated, there is no hydrodynamic interaction and the vehicles operates as it would in an unobstructed flow field. Rather than reducing the domain, a constraint is established that maintains the distance between the centers of buoyancy of the two vehicles y_{Dist} to be less than or equal to $2D_{UUV} + D_{Sub}/2$. This constraint is non-dimensionalized in terms of the input variables as shown in equation (4.5).

$$-8.575R_{Lat} + 2\left(\frac{D_{Sub}}{D_{UUV}}\right)^{-1} + 0.5 \geq 0 \tag{4.5}$$

There are also simulations that are infeasible based on the relationship between the length and diameter of the UUVs. In order to determine the viable relationship between the L/D_{UUV} and the D_{Sub}/D_{UUV}, all of the UUV architectures in table 4.1 are plotted in figure 4-3. Two constraints are developed to reflect feasible UUV designs. For example, if a large diameter UUV, like the Snakehead, had a large L/D_{UUV}, then it would be longer than the diameter of the submarine. Therefore, one constraint is established for vehicles that are too long, while another is established for vehicles that are too short for a given UUV diameter. Eliminating these kinds of configurations allows a more thorough study of the feasible design space as shown in the following figure.

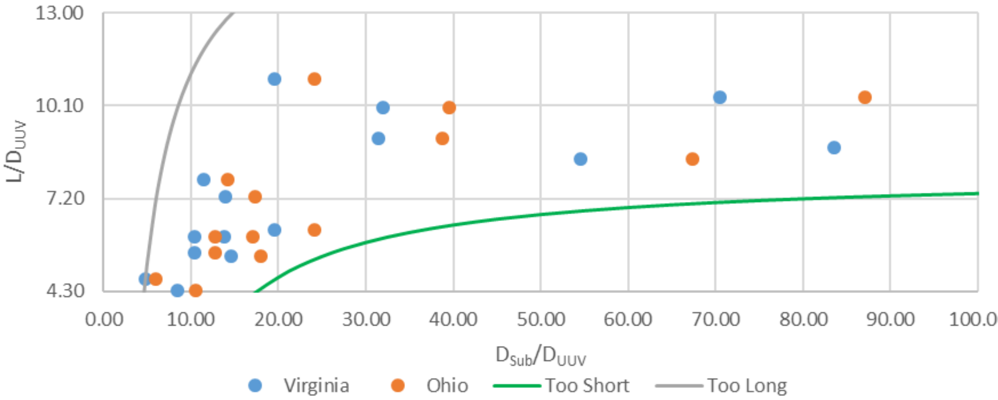

Figure 4-3: The ROM model is constrained to ensure that only the feasible UUV lengths and diameters are explored and modeled by constraining relationship between L/D_{UUV} and D_{Sub}/D_{UUV}.

The "too short" and "too long" UUV geometric constraints are once again established in terms of the input variables in table 4.2. The following equations represent these constraints based on the input variables.

$$65.44\left(\frac{D_{Sub}}{D_{UUV}}\right)^{-1}+(L/D_{UUV})-8\geq 0 \tag{4.6}$$

$$-58.81\left(\frac{D_{Sub}}{D_{UUV}}\right)^{-1}-(L/D_{UUV})+17\geq 0 \tag{4.7}$$

4.4 Reduced Order Model Approach

In order to simulate how hydrodynamic interactions impact the maneuvering of a UUV as it operates in close proximity to a moving submarine, these hydrodynamic interactions need to be predicted in real time as the at the UUV changes position, heading, and speed. Potential flow simulators may be fast enough to be solved in real time, but their oversimplified physical assumptions lead to inaccuracies. CFD simulations are often accurate in their ability to replicate real-world results, but they are several orders of magnitude to slow to be able to be incorporated into UUV autonomy and control systems. As such, a surrogate model is developed in order to bridge this gap.

GP regression is selected as the surrogate method because it is non-parametric and well suited to determine the form of any sufficiently smooth output function, like the problem studied in this thesis. Additionally, GP regression does not require large amounts of data for accurate predictions, which makes this method ideal due to the expensive computational cost to acquire CFD simulation data [20]. A GP regression model is trained on a data set of CFD simulations in order to reflect the accurate physics of the CFD while being able to be solved in real time. Further details about the GP regression fundamental equations, kernels, hyperparameter selection, and uncertainty are found in section 2.2.1.

Due to the expensive nature of performing CFD simulation, careful consideration is used to determine the next location in the domain where the CFD simulation ought to be performed. This is known as active learning. The non-myopic multi-fidelity (NMMF) active learning algorithm is used with GP regression to model the hydrodynamic interactions between a UUV and submarine. This algorithm is discussed in detail in section 2.3. This algorithm exploits the exploration benefit of performing low fidelity simulations with the accuracy benefits of high fidelity simulations. For this thesis, the low fidelity simulator is a potential flow solver known as FS-Flow [27]. Low fidelity potential flow solvers use simplified physics which neglects viscosity, skin friction, boundary layer development, flow separation, and leads to the d'Alembert paradox, which predicts zero drag on a UUV moving at constant velocity [14]. In order to combat these physical limitations, potential flow solvers are often supplemented with a simple parametric model to help predict the effects of viscosity on the moving body. FS-Flow uses the panel method to resolve the flow around a moving body and supplements the solution with one of four different viscous correlation lines. The frictional resistance can be estimated using the International Towing Tank Conference (ITTC) 57, Hughes, Grigson, or Katsui viscous correlation lines [27]. The ITTC-57 correction line is used to develop this ROM. Likewise, the high fidelity simulator is a commercially available CFD software known as Siemens Star-CCM+. The CFD simulation setup is the same as shown in chapter 3. This setup accurately predicted the hydrodynamic interactions between the UUV and submarine as shown by the validated results. In chapter 3, the submarine is the Explorer hull while the UUV is the SUBOFF hull in order to be validated against tow tank experiments found in literature [3]. For the development of this ROM, the submarine is a 34 foot (≈10.36 m) diameter SUBOFF hull while the UUV is the Explorer hull in order to more accurately represent the vehicles used in real-world L&R operations.

The surrogate model needs to be able to determine the surge, sway, and yaw coefficients for the UUV, i.e. it requires a vector output. This requires additional complexity than is found in typical single output GP regression. This multiple output surrogate model is developed by simply making three separate single output GP regression models, one for each output. However, multiple output active learning is much more problematic because there are numerous ways in which each output could be used to select the next optimal sampling location. As discussed in much more detail found in section 2.5, the maximum variance criteria is used to develop this GP regression model because it outperformed other sampling methods.

The NMMF active learning algorithm is iterated until 100 high fidelity CFD simulations are performed. At this point, new high CFD simulations have little improvement on the accuracy of the surrogate model. The GP regression model is trained on these 100 data points, and can now be used to predict surge, sway, and yaw coefficients for any UUV position, heading, speed, or size within the input domain.

4.5 Results

As discussed in section 4.2,this ROM has six input parameters. There is no straightforward way to illustrate a six-dimensional parameter space, but to help visualize the results, a series of two-dimensional plots are generated while keeping the other four input dimensions constant. This allows the impact of each dimension to be assessed while also displaying some interactions between input variables.

Figure 4-4 shows how the sway and yaw coefficients for the UUV vary as the UUV is in different lateral and longitudinal positions from the submarine. A positive sway coefficient pushes the UUV away from the submarine and a positive yaw moment causes the bow of the UUV to be rotated away from the submarine.

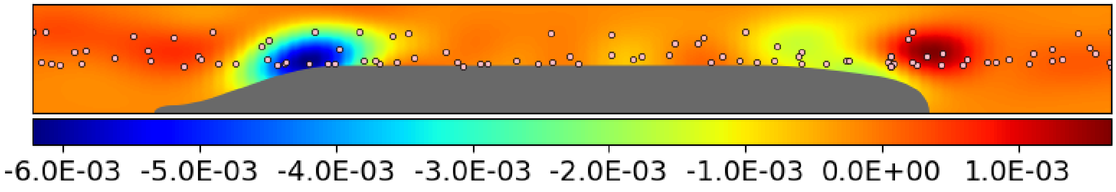

(a) Colormap of sway coefficient Y' at various locations around the submarine at a fixed $u = 3.5$ knots, $\psi = 0°$, $D_{Sub}/D_{UUV} = 10$, and $L/D_{UUV} = 8$. Regions around the bow of the submarine push the UUV away from the submarine while regions around the stern of the submarine pull the UUV toward the submarine.

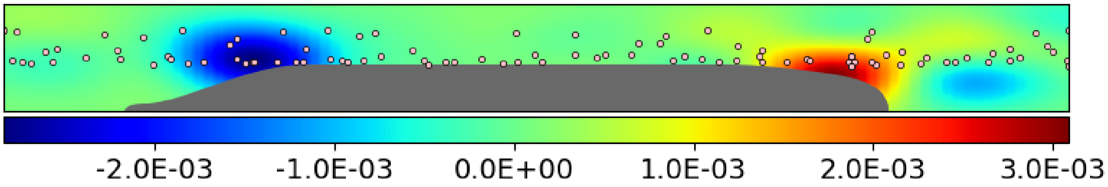

(b) Colormap of yaw coefficient N' at various locations around the submarine at a fixed $u = 3.5$ knots, $\psi = 0°$, $D_{Sub}/D_{UUV} = 10$, and $L/D_{UUV} = 8$. Regions around the bow of the submarine rotate the bow of the UUV away from the submarine while regions around the stern of the submarine rotate the UUV bow toward the submarine.

Figure 4-4: Colormaps of the hydrodynamic interaction sway and yaw coefficients Y' and N' at different lateral and longitudinal positions with respect to the submarine. The dots represent the locations selected using the NMMF algorithm to perform a high fidelity CFD simulation [73].

Each high fidelity CFD simulation is represented as a dot in figure 4-4. The domain is constrained such that the UUV will not be positioned directly in front of or behind the submarine in order to avoid the risk of a collision. This figure illustrates how there are large sway and yaw oscillations as a UUV changes its position longitudinally along the submarine. Near the bow of the submarine, the UUV experiences a sway and yaw force and moment that push the vehicle away and cause the UUV bow to rotate away from the submarine. However, near the stern of the submarine, the UUV is pulled toward and the UUV bow is rotated toward the submarine. The magnitude of these forces and moments decreases as the UUV is positioned laterally farther from the submarine. The oscillations in sway and yaw based on UUV location that are captured by this surrogate model are observed in tow tank experiments between a model submarine and UUV [3]. However, these tow tank experiments are greatly limited in the size of the UUV that they can evaluate. In order to have similitude of the diameter ratios between the real world vehicles, the model UUV would have to be too small to capture any accurate EFD data of the hydrodynamic interactions.

These large sway and yaw coefficients with steep gradients near the bow and stern of the submarine provide an obstacle for the launch and recovery of UUVs from submarines. Accurately modeling these forces and moments and incorporating them into the UUV control and autonomy systems could enable UUVs to predict these large hydrodynamic interactions and accurately navigate through these regions. Another option would be to develop launch and recovery architectures that avoid these regions altogether. This surrogate model could also be used to establish operating envelopes. These are regions in which the UUV should not operate in order to avoid forces or moments large enough to interfere with launch and recovery operations.

The surge force coefficient also experiences unique hydrodynamic interactions near the bow and stern of the submarine. Figure 4-5 shows how the surge force coefficient varies along the length of the submarine.

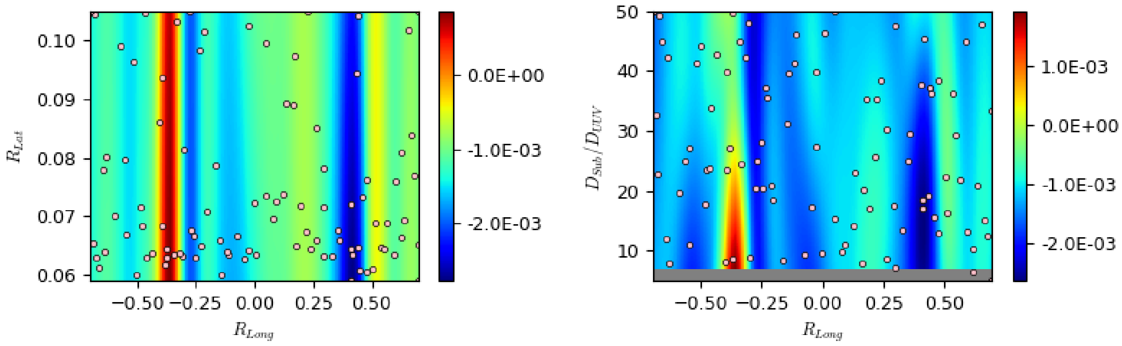

(a) Surge coefficient X' at various R_{Lat} and R_{Long} locations around the submarine at a fixed $u = 3.5$ knots, $\psi = 0°$, $D_{Sub}/D_{UUV} = 20$, and $L/D_{UUV} = 8$. Near the stern of the submarine, the reduced order model predicts a positive surge experienced by the UUV.

(b) Surge coefficient X' at various D_{Sub}/D_{UUV} and R_{Long} locations around the submarine at a fixed $R_{Lat} = 0.08$, $u = 3.5$ knots, $\psi = 0°$, and $L/D_{UUV} = 8$. The reduced order model predicts the positive surge experienced near the stern of the submarine decreases for smaller diameter UUVs.

Figure 4-5: UUV hydrodynamic interaction surge coefficient X' at various longitudinal separation ratios R_{Long} from the submarine

Figure 4-5 shows that the UUV experiences a substantial drop in the surge that opposes forward UUV motion near the stern of the submarine at about $R_{Long} \approx -0.4$. In fact, this hydrodynamic interaction causes the surge force to become positive. This means that this hydrodynamic interaction overcomes the drag of the vehicle, which would cause it to accelerate forward, even with no thrust from the UUV propeller.

There is a low pressure region and the end of the parallel mid-body of the submarine as it transitions to the stern. There is also a high pressure region farther down the stern of the submarine. The UUV experiences this positive surge when it encounters the steep pressure gradient between these two regions. Also, as the fluid flows along the stern of the submarine and passes the bow of the UUV, it accelerates between the two vehicles due to the flow restriction. This restricted flow results in higher fluid velocities between the vehicles, which causes an additional drop in pressure due to the Bernoulli effect. The drop in pressure near the bow of the UUV also contributes to the drop in surge and causes the UUV to get pulled forward. Additionally, the flow around the stern of the submarine meets the UUV at an angle that causes a large lift. This lift is perpendicular to the flow and causes the resultant total force vector to have a component in the forward direction of the UUV. Figure 4-6 summarizes this complex interaction.

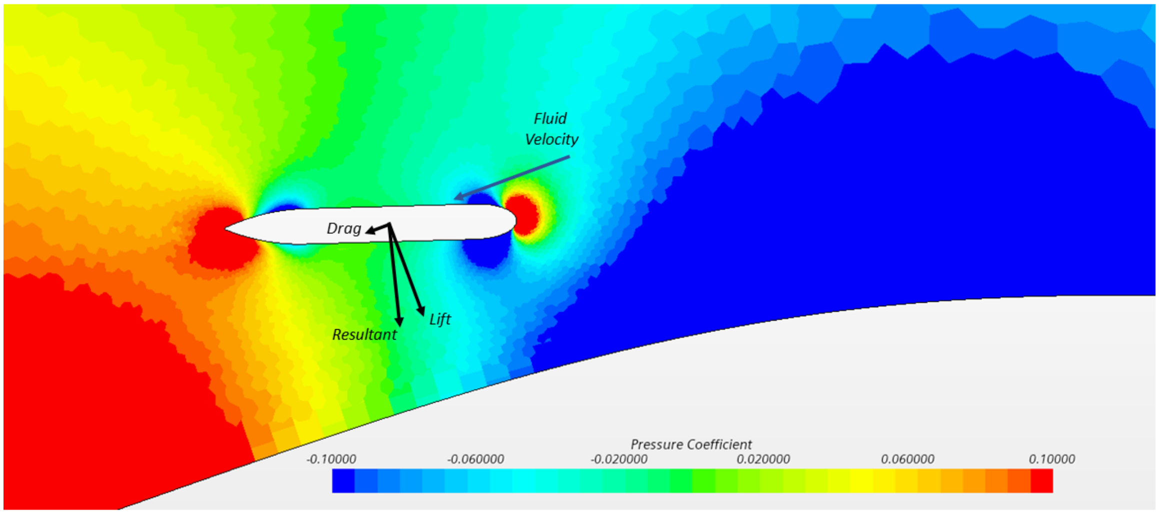

Figure 4-6: Pressure field of the hydrodynamic interactions near the stern of the submarine. The steep pressure gradient and flow field result in the UUV experiencing a positive surge.

This specific hydrodynamic interaction could make UUV launch and recovery operations particularly challenging because it is so far outside of the normal UUV operating window. Figure 4-5b shows that the magnitude of this hydrodynamic interaction decreases as the diameter of the UUV decreases. This means that smaller UUVs would be better equipped to overcome this specific hydrodynamic interaction.

A long slender body without control fins experiences a destabilizing effect when in steady translation. This is known as the munk moment [14]. Also, the sway force increases as the heading angle increases, just like lift increases when the angle of attack increases on an airfoil. Figure 4-7 shows how the sway and yaw coefficients vary based on the heading angle and speed of the UUV.

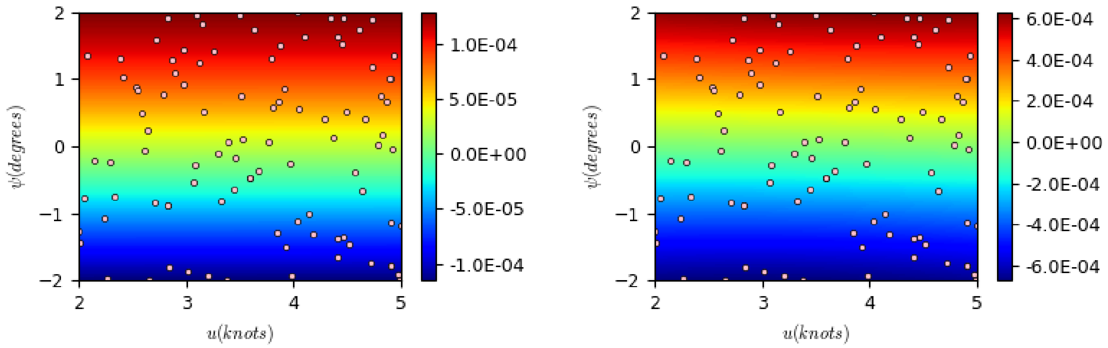

(a) Sway coefficient Y' of a UUV at various heading angles ψ and speeds u with a fixed $R_{Long} = 0$, $R_{Lat} = 0.08$, $D_{Sub}/D_{UUV} = 20$, and $L/D_{UUV} = 8$. The reduced order model predicts a near-linear relationship been the sway and heading angle.

(b) Yaw coefficient N' of a UUV at various heading angles ψ and speeds u with a fixed $R_{Long} = 0$, $R_{Lat} = 0.08$, $D_{Sub}/D_{UUV} = 20$, and $L/D_{UUV} = 8$. The reduced order model predicts a near-linear relationship been the yaw and heading angle.

Figure 4-7: Maps of the sway and yaw coefficients Y' and N' at various heading angles ψ and speeds u for a UUV with a fixed $R_{Long} = 0$, $R_{Lat} = 0.08$, $D_{Sub}/D_{UUV} = 20$, and $L/D_{UUV} = 8$.

Figure 4-7 shows that if the vehicle is at a non-zero heading angle, there is a resulting moment that will cause the vehicle to rotate in the direction in which it is angled. The surrogate model is able to accurately predict the munk moment of the UUV and the expected behavior of how it increases nearly linearly with heading angle [15]. The same relationship between heading angle and sway exists and the reduced order model accurately captures this phenomenon as well. Additionally, because the sway and yaw coefficients are non-dimensionalized using the velocity of the vehicle, these non-dimensional coefficients are expected to be relatively independent of the speed [14, 15]. The surrogate model is also able to capture this effect.

The total drag on a submarine or UUV is a combination of its pressure (form) drag, caused by wake formation and boundary layer separation, and its viscous (skin) drag, caused by the fluid friction on the wetted surface of the vehicle. Vehicles have an optimal length to diameter ratio that reduces the drag on the vehicle [6]. When vehicles are very short, they are more like bluff bodies and have a lot of pressure drag. As the vehicle becomes longer, the form drag decreases. However, when they become too long, the increase in viscous drag due to the increase in wetted surface area outweighs the loss in pressure drag. This means that a UUV has an optimal length to diameter ratio L/D_{UUV} for reducing drag. The optimal L/D_{UUV} is dependent on the shape and speed of the vehicle and is usually in the range of 8 to 12. Figure 4-8 shows how the surge coefficient varies with L/D_{UUV}.

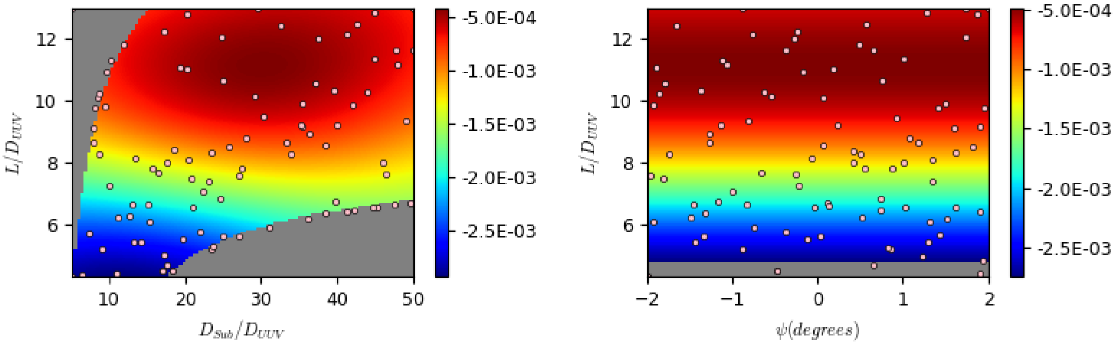

(a) Surge coefficient X' of a UUV with various L/D_{UUV} and D_{Sub}/D_{UUV} for a fixed $R_{Long} = 0$, $R_{Lat} = 0.08$, $u = 3.5$ knots, and $\psi = 0°$. UUVs with a small L/D_{UUV} experience more pressure drag so optimal $L/D_{UUV} \approx 10 - 12$.

(b) Surge coefficient X' of a UUV at various L/D_{UUV} and ψ for a fixed $R_{Long} = 0$, $R_{Lat} = 0.08$, $u = 3.5$ knots, and $D_{Sub}/D_{UUV} = 20$. UUVs with a small L/D_{UUV} experience more pressure drag so optimal $L/D_{UUV} \approx 10 - 12$.

Figure 4-8: Maps of the surge coefficient X' at various L/D_{UUV} for a UUV with a fixed $R_{Long} = 0$, $R_{Lat} = 0.08$, and $u = 3.5$ knots. This demonstrates the prediction of optimal L/D_{UUV}.

This illustrates how the surrogate model is able to identify the trade-off between pressure drag and viscous drag for different UUV lengths. The surrogate identified the optimal length to diameter ratio of the UUV to be between about 10 and 12 for the given UUV shape and speed. Additionally, the surrogate also found that the surge is relatively independent of small changes in heading angles. This is consistent with real world results [51]. The gray region in figure 4-8a represents a constraint within the domain that is unexplored due to UUV infeasibility as shown in equations (4.6) and (4.7) and figure 4-3.

Another benefit of the NMMF active learning GP regression process is that the process models the difference between the high fidelity CFD and low fidelity potential flow simulations. This means that the results of the model can be used to identify scenarios in which the low fidelity simulations fail to capture the accuracy of the high fidelity simulations. Figure 4-9 compares the sway and yaw coefficients for the high fidelity surrogate model with the low fidelity model surrogate.

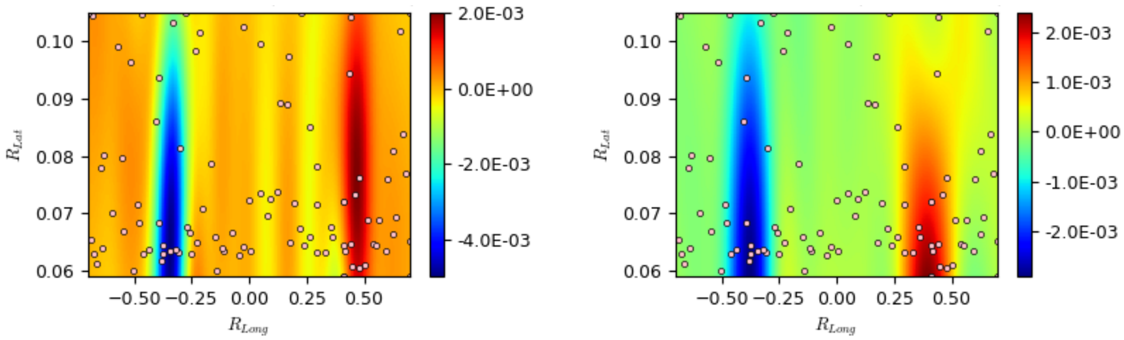

(a) High fidelity surrogate model prediction of the sway coefficient Y' of a UUV at various R_{Lat} and R_{Long} for a fixed $u = 3.5$ knots, $\psi = 0°$, $D_{Sub}/D_{UUV} = 20$ and $L/D_{UUV} = 8$.

(b) High fidelity surrogate model prediction of the yaw coefficient N' of a UUV at various R_{Lat} and R_{Long} for a fixed $u = 3.5$ knots, $\psi = 0°$, $D_{Sub}/D_{UUV} = 20$ and $L/D_{UUV} = 8$.

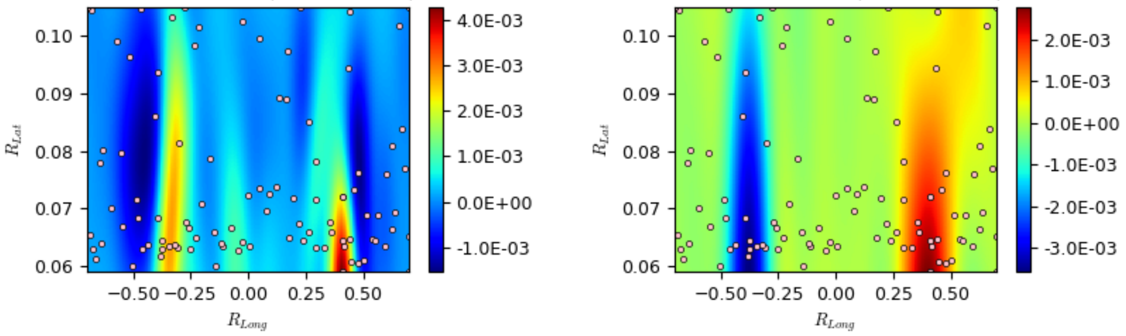

(c) Low fidelity surrogate model prediction of the sway coefficient Y' of a UUV at various R_{Lat} and R_{Long} for a fixed $u = 3.5$ knots, $\psi = 0°$, $D_{Sub}/D_{UUV} = 20$ and $L/D_{UUV} = 8$.

(d) Low fidelity surrogate model prediction of the yaw coefficient N' of a UUV at various R_{Lat} and R_{Long} for a fixed $u = 3.5$ knots, $\psi = 0°$, $D_{Sub}/D_{UUV} = 20$ and $L/D_{UUV} = 8$.

Figure 4-9: Comparison of sway and yaw coefficients of the high and low fidelity surrogate models of a UUV at various R_{Lat} and R_{Long} for a fixed $u = 3.5$ knots, $\psi = 0°$, $D_{Sub}/D_{UUV} = 20$ and $/D_{UUV} = 8$. Low fidelity cannot accurately predict sway coefficient Y', but performs well for yaw coefficient N'.

Figure 4-9 shows that the low fidelity potential flow model is quite accurate at predicting the yaw coefficient, but has major limitations on predicting the sway coefficient due to the d'Alembert paradox [14, 15]. Another example of this limitation is the inability of the low fidelity potential flow solver to determine the change in sway at various heading angles. Figure 4-10 compares heading angles from the potential flow model with the high fidelity CFD model. This shows how potential flow is not able to accurately capture how the sway coefficient varies with changes to the heading angle. In fact, the low fidelity model predicts an almost constant near zero value which is about the midpoint of the actual CFD results. This is the best that the low fidelity model can do because of the d'Alembert paradox of potential flow.

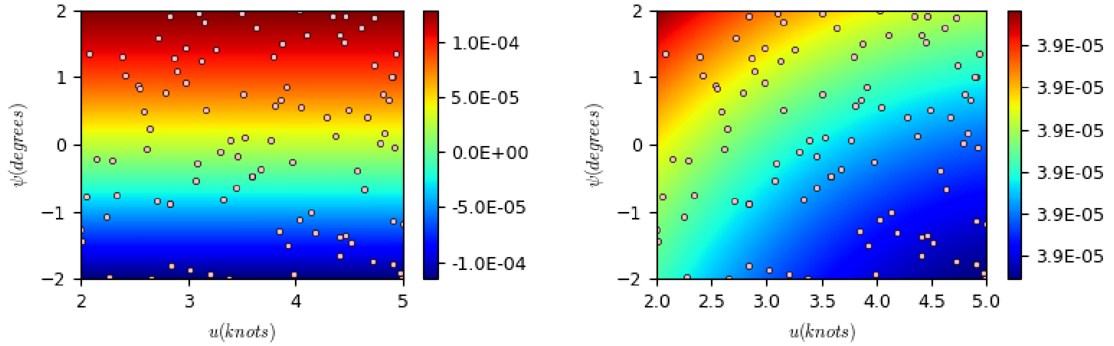

(a) High fidelity surrogate model prediction of the sway coefficient Y' of a UUV at various heading angles ψ and speeds u with a fixed $R_{Long} = 0$, $R_{Lat} = 0.08$, $D_{Sub}/D_{UUV} = 20$, and $L/D_{UUV} = 8$. This accurately reflects expected the near-linear relationship between sway and heading angle.

(b) Low fidelity surrogate model prediction of the sway coefficient Y' of a UUV at various heading angles ψ and speeds u with a fixed $R_{Long} = 0$, $R_{Lat} = 0.08$, $D_{Sub}/D_{UUV} = 20$, and $L/D_{UUV} = 8$. This predicts a constant near-zero value as expected by the d'Alembert paradox.

Figure 4-10: Comparison of sway and yaw coefficients of the high and low fidelity surrogate models of a UUV at various heading angles ψ and speeds u with a fixed $R_{Long} = 0$, $R_{Lat} = 0.08$, $D_{Sub}/D_{UUV} = 20$, and $L/D_{UUV} = 8$. Low fidelity cannot to accurately predict sway coefficient Y' due to the d'Alembert paradox.

Because the d'Alembert paradox is a known limitation of potential solvers, many of them have built-in parametric models that augment the results. The d'Alembert paradox results in potential flow predicting zero drag around the UUV in steady state translation. In order to provide more accurate results, the FS-Flow potential flow solver uses the ITTC-57 parametric equations to estimate the drag of the UUV [27]. Figure 4-11 compares the surge coefficients of the high fidelity CFD surrogate model and the low fidelity potential flow surrogate model at various UUV length to diameter ratios.

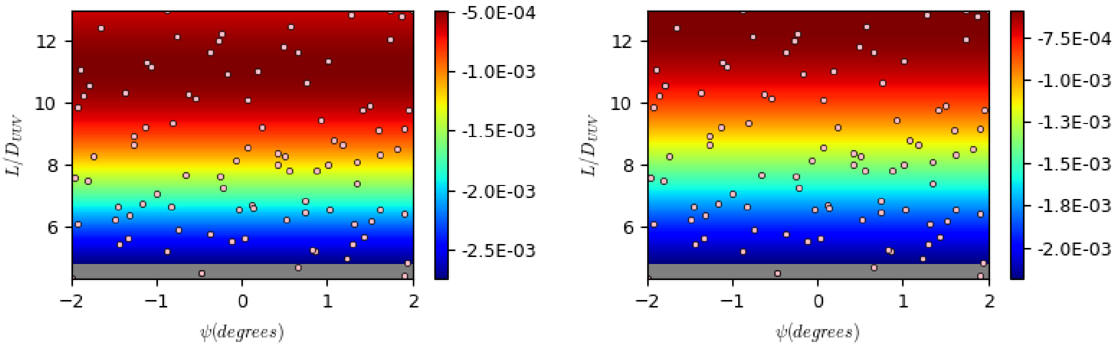

(a) High fidelity surrogate model prediction of the surge coefficient X' of a UUV at various L/D_{UUV} and heading angles ψ with a fixed $R_{Long} = 0$, $R_{Lat} = 0.08$, $u = 3.5$ knots, and $D_{Sub}/D_{UUV} = 20$.

(b) Low fidelity surrogate model prediction of the surge coefficient X' of a UUV at various L/D_{UUV} and heading angles ψ with a fixed $R_{Long} = 0$, $R_{Lat} = 0.08$, $u = 3.5$ knots, and $D_{Sub}/D_{UUV} = 20$.

Figure 4-11: Comparison of surge coefficient X' of the high and low fidelity surrogate models of a UUV at various L/D_{UUV} and heading angles ψ with a fixed $R_{Long} = 0$, $R_{Lat} = 0.08$, $u = 3.5$ knots, and $D_{Sub}/D_{UUV} = 20$. The ITTC-57 parametric equations of the low fidelity potential flow simulations are similar to the results of the high fidelity CFD simulations.

Overall, the built-in ITTC-57 parametric equations of the low fidelity potential flow model are very similar to the model trained on CFD data. This allows the potential flow model to predict the surge coefficient much better than the sway coefficient.

4.6 Validation

In order to test the accuracy of the model, a total of 500 Latin hypercube samples are used as test data for the GP regression model. The mean absolute error (MAE) between the predicted and actual results of the test data is determined for each of the three outputs. Because these values are hard to conceptualize, MAE can be thought of in terms of the control system of the UUV and how these errors translate into UUV control values. The MAE of the sway and yaw coefficients can be represented as an equivalent rudder angle difference $\Delta\delta_{eq,Y}$ or $\Delta\delta_{eq,N}$. This is how much the rudder angle would need to change to produce the force or moment equivalent to the MAE. Likewise, the surge coefficient MAE can be thought of as a percentage of the propulsive force of the UUV ($\%X_{Prop}$). The hydrodynamic coefficients in use to determine these error equivalents are taken from the Remus 100 [74].

Table 4.3: Mean absolute error and error equivalents of the various model outputs

Output	Mean Absolute Error	Error Equivalents
X'	7.492E-04	10.26% X_{prop}
Y'	7.220E-04	$\Delta\delta_{eq,Y} = 1.78$ degrees
N'	7.629E-04	$\Delta\delta_{eq,N} = 3.95$ degrees

4.7 Conclusion

Overall, the reduced order model is able to predict the complex surge, sway, and yaw hydrodynamic interactions that are determined using the CFD simulations and validated against tow tank experiments. By refining the input domain, utilizing the NMMF active learning algorithm, and implementing the maximum variance multiple output criteria, this ROM is able to capture the known hydrodynamic interactions much better than previous modeling attempts [67]. This reduced order model can be used to determine the hydrodynamic interactions in within milliseconds. This is several orders of magnitude faster than performing a CFD simulation, which usually takes several hours to complete. This allows for the development of force and moment colormaps, as seen in section 4.5, as well as enabling the hydrodynamic interactions to be incorporated into UUV maneuvering simulators.

THIS PAGE INTENTIONALLY LEFT BLANK

Chapter 5

Simulating UUV Motion with Hydrodynamic Interactions

5.1 Introduction

Several efforts have been made to model the hydrodynamic interaction forces and moments acting on a UUV when it operates near a moving submarine [3, 19, 75]. These unwanted hydrodynamic interactions push and rotate the UUV and may cause it to become uncontrollable or collide with the submarine [3]. Real-time modeling of these hydrodynamic interactions is essential to simulate the motion required to launch and recover UUVs from submarines because the UUV control surfaces and propeller respond to real-time changes in the state of the UUV [15, 64]. There is no method or tool that enables the real-time accurate modeling of these complex hydrodynamic interaction forces and moments that a UUV experiences when operating in close proximity to a moving submarine. In chapter 4, a surrogate reduced-order model (ROM) of the hydrodynamic interactions between a UUV and submarine is developed that is capable of predicting these forces and moments in real time. This thesis explores incorporating this surrogate model into a UUV motion simulator in order to explore how the hydrodynamic interactions impact the ability of the UUV to maneuver around the submarine.

Integrating this surrogate model into UUV motion simulators enables a better understanding of the current UUV autonomy and control capabilities. This is accomplished by using the forces and moments of the surrogate model in the equations of motion in order to determine how they impact the UUV. As the UUV position, speed, and heading change, the surrogate is capable of predicting the hydrodynamic interactions in real-time to see how the autonomy and control systems respond to these forces and moments. This allows for the rapid exploration of which UUV maneuvers can be successfully performed around a submarine. This can be used to develop safe operating envelopes around the submarine for UUV L&R operations. Additionally, this allows for the rapid testing of new autonomous behaviors designed to overcome unwanted hydrodynamic interactions and improve launch and recovery maneuvering.

This chapter describes the method to incorporate the Gaussian Process (GP) regression model into the UUV motion simulator. This starts with an overview of the UUV autonomy architecture and how each component is used to simulate UUV motion. Next, a detailed account is provided of the equations of motion, control theory, and autonomous behaviors which are used to develop the UUV maneuvering simulator. This includes details about how the ROM is incorporated into the equations of motion and UUV autonomy architecture. Ocean waves are also incorporated into the UUV maneuvering simulator in order to analyze the robustness of the UUV to overcome perturbations. Lastly, the results of the UUV maneuvering simulations with the ROM hydrodynamic interactions are presented, including the development of safe operating envelopes for the UUV under various conditions as it maneuvers around the submarine.

5.2 Approach

As explained in section 4.2, a body-fixed coordinate system located at the center of buoyancy of the UUV is used to simulate the motion of the UUV. The surge, sway, heave, roll, pitch, and yaw velocities and forces/moments are defined as u, v, w, p, q, r and X, Y, Z, K, M, N respectively. The position of the UUV is expressed in the inertial reference frame using x, y, and z. Likewise, the roll, pitch, and yaw angles are denoted as ϕ, θ, and ψ. The forces and moments can also be non-dimensionalized by the fluid density ρ, UUV speed u, and UUV length L_{UUV}, e.g. $X' = X/(0.5\rho u^2 L_{UUV}^2)$ or $N' = N/(0.5\rho u^2 L_{UUV}^3)$. The distances between the center of buoyancy and the center of gravity of the UUV in the three principle directions are defined as x_g, y_g, and z_g. This coordinate system is illustrated in figure 5-1.

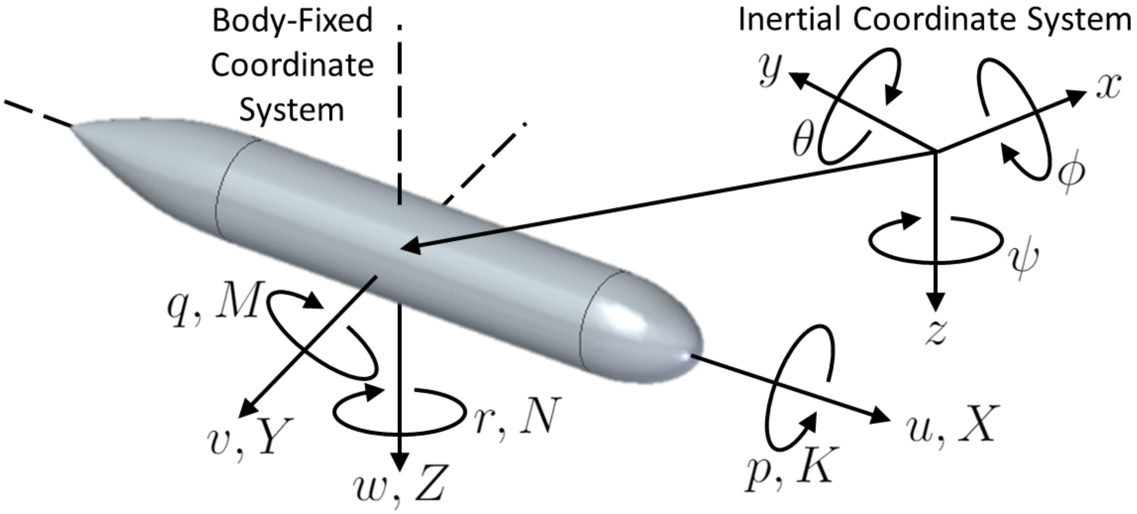

Figure 5-1: Orientation of UUV body-fixed and inertial coordinate systems with their corresponding velocities, forces, and moments [64]

.

Because experimentally attempting to study the hydrodynamic interactions between a submarine and UUV is both costly and has the risk of collision between the vehicles, a simulator is used to model the behavior and motion of a UUV. This simulator is designed using the framework outlined in the open-source UUV autonomy simulator known as MOOS-IvP [65]. This framework uses three different vectors to relay information between apps within the simulator. These three different vectors are the state vector $\mathbf{x}$, input vector $\mathbf{u}$, and desired state vector $\mathbf{x_d}$ and are listed in equation (5.1). The propeller thrust and torque are denoted as X_{Prop} and K_{Prop} respectively while the rudder and stern plane angles are denoted as δ_r and δ_s respectively.

$$
\begin{aligned}
\mathbf{x} &= [u, v, w, p, q, r, x, y, z, \phi, \theta, \psi]^T \\
\mathbf{u} &= [X_{Prop}, K_{Prop}, \delta_r, \delta_s]^T \qquad (5.1) \\
\mathbf{x_d} &= [u_d, ..., \psi_d]^T
\end{aligned}
$$

MOOS-IvP is an open-source C++ UUV simulator that uses three basic apps to model the UUV control system and its impact on UUV motion. The pHelmIvP app takes in the state vector of the vehicle position and motion and uses an autonomous behavior to compute a new desired input vector containing the new desired speed and heading. This desired input vector is passed to the pMarinePID app which simulates a proportional integral derivative (PID) controller to determine the input vector of the propeller thrust and torque, as well as the angle of the stern planes and rudder. This input vector, as well as the state vector, is then passed to the uSimMarine app which updates vehicle state, position and trajectory, based on propeller thrust and control surface positions from the input vector in order to determine the new state vector of the UUV. The process is iterated continually throughout the simulation. Figure 5-2 shows an overview of the simulation architecture.

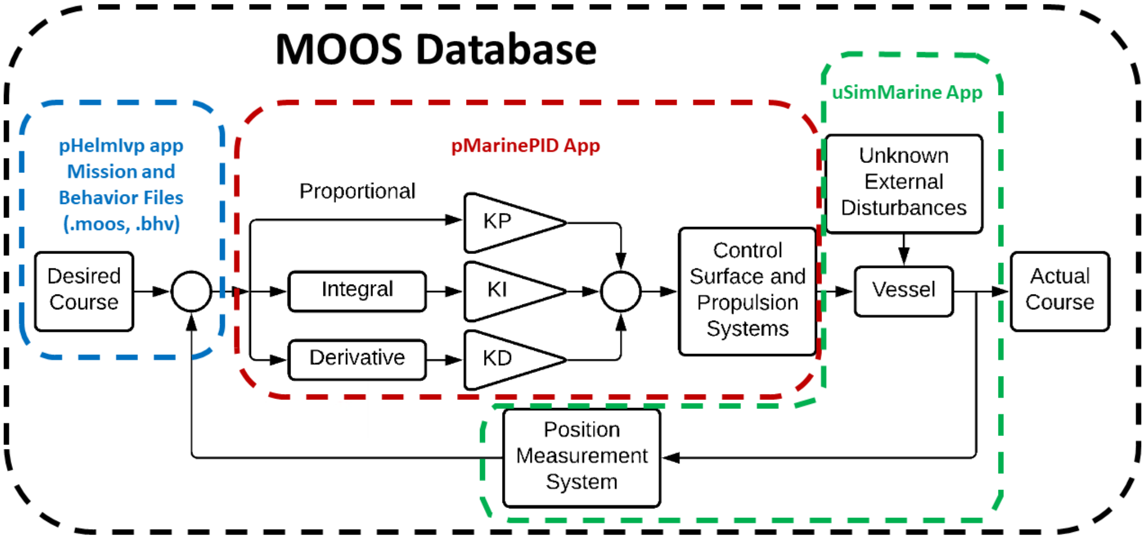

Figure 5-2: Overlay of standard UUV control system block diagram with the MOOS-IvP architecture. This outlines the role of each app to fulfill its purpose of the control system [65].

While UUV simulators have been used extensively to model UUV missions, there are no known simulators that are able to model the hydrodynamic interactions between a UUV and a moving submarine with the accuracy of CFD [3]. This is because the forces and moments felt by the UUV need to be determined in real-time in order to determine how the UUV and submarine hydrodynamic interactions impact the UUV motion. Real-time determination of these hydrodynamic interactions is beyond current CFD capability. However, the ROM discussed in chapter 4 is capable of performing real-time predictions of the hydrodynamic interaction forces and moments on the UUV based on the state vector of the UUV. In this thesis, this new surrogate model is used to simulate how these hydrodynamic interactions impact the motion of a UUV as it maneuvers near a moving submarine.

5.3 Deviations from MOOS-IvP

While MOOS-IvP is an extremely robust and capable open-source UUV simulation tool, there are certain areas of its architecture that present challenges for the integration of hydrodynamic interaction ROM. MOOS-IvP is exceptional at using multi-objective optimization in order to reconcile behaviors that are in competition with each other for the influence of the vehicle. For example, say a UUV is using a "Loiter" behavior that directs the UUV to repeatedly transverse around a square course. The UUV is also using the "Avoid Collision" behavior to ensure that it does not collide with another vehicle. If another vehicle is to enter the course of the UUV, these two behaviors provide different headings in which the UUV should travel. MOOS-IvP reconciles these competing behaviors in order to determine the best course for the vehicle. Additionally, the pHelmIvP app within MOOS-IvP has many preexisting behaviors that can be leveraged to accomplish various missions. For example, the "Shadow" behavior, which adjusts the UUV heading to match the trajectory of another specified vehicle, can be used with the "Cut Range" behavior, which reduces the UUVs range from a specified vehicle, in order to create a "Track and Trail" behavior. The resources used to develop MOOS-IvP have been primarily focused on these capabilities.

As for the uSimMarine app, which updates UUV state, position, speed, and heading based on the UUV state and actuator inputs, the MOOS-IvP uses what is known as a kinematic simulation method. This means that instead of using the forces and moments exerted on the UUV to determine the new vehicle state, the uSimMarine app uses a correlation between the actuator inputs and the corresponding state. For example, the uSimMarine app uses a measured and validated series of correlations between the thrust X_{Prop} and rudder angle δ_r in order to determine the new vehicle speed u and heading ψ respectively. Because this does not use the forces and moments acting on the vehicle to determine the new state of the vehicle, this does not allow the hydrodynamic interaction forces and moments predicted by the ROM to be easily integrated directly into the MOOS-IvP simulator. To overcome this challenge, a dynamic physics simulator using the equations of motion is developed for the UUV simulator. This is the same dynamic simulation approach used in other UUV simulators [64, 66, 15].

Overall, there are two possible system integration approaches to allow the hydrodynamic interaction ROM to be incorporated into the UUV simulator. The first is to create a new uSimMarine app that incorporates the equations of motion in order to perform dynamic simulations, rather than kinematic simulations. The ROM is developed in python using robust open-source GPy libraries. Because the ROM is written in python, it would have to be embedded into C++ using a python interpreter in order to be used by the new uSimMarine app and the pHelmIvp app of the MOOS-IvP architecture. The second method is to create a separate dynamic simulator in python. Next, the code and architecture of MOOS-IvP are leveraged to convert the necessary components into python in order to be compatible with the ROM. In either scenario, the dynamic simulator using the UUV equations of motion needs to be developed. For this thesis, the second approach was taken because it presented less integration risk.

5.4 Equations of Motion

The six degree-of-freedom rigid body equations of motion for a UUV are listed in equation (5.2) in terms of the coordinate system in figure 5-1.

$$
\begin{aligned}
m[\dot{u} - vr + wq - x_g(q^2 + r^2) + y_g(pq - \dot{r}) \\
+z_g(pr + \dot{q}) = \sum X_{ext} \\
m[\dot{v} - wp + ur - y_g(r^2 + p^2) + z_g(qr - \dot{p}) \\
+x_g(qp + \dot{r})] = \sum Y_{ext} \\
m[\dot{w} - uq + vp - z_g(p^2 + q^2) + x_g(rp - \dot{q}) \\
+y_g(rq + \dot{p})] = \sum Z_{ext} \\
I_{xx}\dot{p} + (I_{zz} - I_{yy})qr - I_{xz}(\dot{r} + pq) \\
+I_{yz}(r^2 - q^2) + I_{xy}(pr - \dot{q}) \\
+m[y_g(\dot{w} - uq + vp) \\
-z_g(\dot{v} - wp + ur)] = \sum K_{ext} \\
I_{yy}\dot{q} + (I_{xx} - I_{zz})rp - I_{xy}(\dot{p} + qr) \\
+I_{xz}(p^2 - r^2) + I_{yz}(qp - \dot{r}) \\
+m[z_g(\dot{u} - vr + wq) \\
-x_g(\dot{w} - uq + vp)] = \sum M_{ext} \\
I_{zz}\dot{r} + (I_{yy} - I_{xx})pq - I_{yz}(\dot{q} + rp) \\
+I_{xy}(q^2 - p^2) + I_{xz}(rq - \dot{p}) \\
+m[x_g(\dot{v} - wp + ur) \\
-y_g(\dot{u} - vr + wq)] = \sum N_{ext}
\end{aligned}
\tag{5.2}
$$

The *ext* subscript denotes the external forces and moments that the vehicle experiences as to moves through the water.

The total of each one of the principle forces or moments acting on the UUV equals the sum of the hydrostatic forces F_{HS}, hydrodynamic forces on the UUV body due to hydrodynamic damping and added mass F_B, and the hydrodynamic forces due to the control surfaces and propeller F_C. This is shown in equation (5.3).

$$\sum F_{ext} = F_{HS} + F_B + F_C \tag{5.3}$$

Equation (5.4) provides each one of the hydrostatic forces and moments of the UUV in the principle directions where W is the vehicle weight and B is the vehicle buoyancy.

$$\begin{aligned} X_{HS} &= -(W - B)\sin\theta \\ Y_{HS} &= (W - B)\cos\theta\sin\phi \\ Z_{HS} &= (W - B)\cos\theta\cos\phi \\ K_{HS} &= -(y_g W - y_b B)\cos\theta\cos\phi \\ &\quad -(z_g W - z_b B)\cos\theta\sin\phi \\ M_{HS} &= -(z_g W - z_b B)\sin\theta \\ &\quad -(x_g W - x_b B)\cos\theta\cos\phi \\ N_{HS} &= -(x_g W - x_b B)\cos\theta\sin\phi \\ &\quad -(y_g W - y_b B)\sin\theta \end{aligned} \tag{5.4}$$

The hydrodynamics forces and moments on the UUV body F_B include a sum of the damping forces F_d and moments M_d and the added mass forces F_a and moments M_a [15, 14]. The hydrodynamics of a UUV moving at a high speed in six degrees of freedom is coupled and highly non-linear [76]. As such, a standard method of capturing this non-linear behavior is by using hydrodynamic coefficients, which are often referred to as hydrodynamic derivatives. The force or moment that a vehicle experiences when moving at a constant velocity is known as hydrodynamic damping. The hydrodynamic damping coefficients are summarized in equation (5.5) where $i_1, i_2 = 1, 2, 3, 4, 5, 6$ represent the six degrees of freedom. $F_{d,1}$, $F_{d,2}$, $F_{d,3}$ and $M_{d,1}$, $M_{d,2}$, $M_{d,3}$ represent the surge X_d, sway Y_d, heave Z_d damping forces, and the roll K_d, pitch M_d, and yaw N_d damping moments respectively where $j = 1, 2, 3$.

$$\begin{aligned} F_{d,j} &= \sum_{i_1=1}^{6} \sum_{i_2=1}^{6} F_{j,u_{i_1}u_{i_2}} u_{i_1} u_{i_2} \\ M_{d,j} &= \sum_{i_1=1}^{6} \sum_{i_2=1}^{6} M_{j,u_{i_1}u_{i_2}} u_{i_1} u_{i_2} \\ & where \\ F_{j,u_{i_1}u_{i_2}} = M_{j,u_{i_1}u_{i_2}} &= 0 \; for \; all \; i_1 > i_2 \end{aligned} \tag{5.5}$$

Each force or moment accounts for the damping effect of 21 different independent combinations of flow velocities through the use of hydrodynamic coefficients. For example, N_{uv} represents the hydrodynamic coefficient that when multiplied by the surge and sway velocities u and v returns the yaw moment that the vehicle experiences due to moving at those two velocities. Also, when the i_1 and i_2 indices account for the same velocity, the absolute value of one of the velocities is used in order to account for the direction of the force. For example, $X_{u|u|}u|u|$ accounts for the surge force experienced by the UUV as it moves in the forward direction. This approach allows for the modeling of the coupled and non-linear behavior of the UUV hydrodynamics. Terms higher than second order are neglected because they have been found to have little impact on the equations of motion [76].

When a vehicle accelerates through a fluid of non-negligible mass, the presence of the fluid around the body acts as an added mass to the body. When a force is exerted on the body, the mass of the body will be accelerated as well as the mass of the fluid that is displaced and flows around the accelerating body. As such, this additional inertial effect is often referred to as the added mass of a vehicle and is denoted as F_a and M_a for the forces and moments respectively. Because the added mass is dependent on the direction of acceleration, an added mass tensor $m_{i_1 i_2}$ may be formed by determining the added mass associated with the force experienced in the i_1 direction due to accelerating the vehicle in the i_2 direction. These added mass terms $m_{i_1 i_2}$ can also be represented as coefficients just like the damping forces and moments, where i_1 is the force and i_2 is the direction of acceleration, i.e. $m_{11} = -X_{\dot{u}}$ and $m_{62} = -N_{\dot{v}}$ [15, 64, 14, 76]. The forces and moments due to the added mass are found in equation (5.6) where once again $i = 1, 2, 3, 4, 5, 6$ and $j, k, l = 1, 2, 3$ [14, 15]. The equation uses the alternating tensor from Einstein summation notation which is denoted as ϵ_{jkl}.

$$\begin{aligned} F_{a,j} &= -\dot{u}_i m_{ji} - \epsilon_{jkl} u_i u_{k+3} m_{li} \\ M_{a,j} &= -\dot{u}_i m_{j+3,i} - \epsilon_{jkl} u_i u_{k+3} m_{l+3,i} \\ &\quad - \epsilon_{jkl} u_k u_i m_{li} \end{aligned} \tag{5.6}$$

The hydrodynamic forces and moments due to the control surfaces and propeller F_C are also represented using hydrodynamic coefficients. Due to symmetry, the propeller only has an effect on surge and roll and the control surfaces have no effect on the roll. Also, the control surfaces are assumed to have negligible drag compared to the rest of the vehicle, due to their slender profile and small surface area. The thrust and torque of the propeller are denoted as X_{Prop} and K_{Prop} respectively. The rudder and stern plane angles are denoted as δ_r and δ_s respectively and measured in radians. Equation (5.7) shows each of the six principle forces and moments due to the control surfaces and propeller.

$$\begin{aligned}
X_C &= X_{Prop} \\
Y_C &= Y_{uu\delta_r} u^2 \delta_r \\
Z_C &= Z_{uu\delta_s} u^2 \delta_s \\
K_C &= K_{Prop} \\
M_C &= M_{uu\delta_s} u^2 \delta_s \\
N_C &= N_{uu\delta_r} u^2 \delta_r
\end{aligned} \tag{5.7}$$

The total forces and moments exerted on the vehicle is the sum of the hydrostatic, damping, added mass, and control forces and moments outlined in equations (5.4, 5.5, 5.6, 5.7). There are a large number of terms for each force and moment, but many of them are zero or negligible. Determining hydrodynamic coefficients can be performed using potential flow, slender body strip theory, computational fluid dynamics, or physical experiments on models [15, 64, 14]. The following simplifications are made to the overall equations of motion in order to reduce the effort needed to determine all of the hydrodynamic coefficients and reduce the computational cost of performing CFD simulations for training data for the ROM [15, 64, 66].

- Three Degrees of Freedom - For simplicity, the full six degree of freedom equations are reduced to three by assuming that roll, pitch, and heave are zero. Because many UUVs have similar geometry in the xy and xz plane, the heave and pitch results are the same as the sway and yaw results [64]. Roll is also assumed to have negligible impact on UUV motion due to vehicle symmetry [64, 66]. This simplification drastically reduces the effort to model submarine and UUV hydrodynamic interactions while still capturing the fundamental behaviors and capabilities. This is because the computational cost of a CFD simulation is reduced by utilizing symmetry and the number of CFD simulations needed to train the ROM is drastically reduced by reducing its input dimension.

- Hydrostatics - UUVs are usually designed to be neutrally buoyant so the vehicle weight and buoyancy offset. Additionally, the center of gravity is located in approximately the same location in the xy plane as the center of buoyancy so all hydrostatic terms cancel out [64, 66].

- Body Damping Forces - The sway and yaw hydrodynamic coefficients for the coupled linear cross flow and angular velocity terms are found to be negligible [64]. This includes Y_{vr} and N_{vr}. Also, assuming xy plane symmetry allows for the neglecting of drag-induced forces and moments like $Y_{u|u|}$ and $N_{u|u|}$.

- Added Mass - By assuming xy and xz plane symmetry, the added mass tensor simplifies to zero except on the diagonal terms and for the $m_{26} = m_{62}$ and $m_{35} = m_{53}$ terms.

Applying these assumptions to the state, input, and desired input vectors results in the simplified vectors found in equation (5.8).

$$\begin{aligned} \mathbf{x} &= [u, v, r, x, y, \psi]^T \\ \mathbf{u} &= [X_{Prop}, \delta_r]^T \\ \mathbf{x_d} &= [u_d, \psi_d]^T \end{aligned} \tag{5.8}$$

After applying these same simplifications to equations (5.3) through (5.6), the following equation represents the simplified forces and moments experienced on the UUV.

$$
\begin{aligned}
\sum X_{ext} &= X_{\dot{u}}\dot{u} + X_{u|u|}u|u| + X_{vr}vr \\
&\quad + X_{rr}rr + X_{Prop} \\
\sum Y_{ext} &= Y_{\dot{v}}\dot{v} + Y_{\dot{r}}\dot{r} + Y_{v|v|}v|v| + Y_{r|r|}r|r| \\
&\quad + Y_{uv}uv + Y_{ur}ur + Y_{uu\delta_r}u^2\delta_r \\
\sum N_{ext} &= N_{\dot{v}}\dot{v} + N_{\dot{r}}\dot{r} + N_{v|v|}v|v| + N_{r|r|}r|r| \\
&\quad + N_{uv}uv + N_{ur}ur + N_{uu\delta_r}u^2\delta_r
\end{aligned}
\tag{5.9}
$$

By combining equation (5.2) and (5.9) and moving the added mass terms to the left-hand side of the equation, the simplified equations of motion are developed and listed in equation (5.10).

$$
\begin{bmatrix} m - X_{\dot{u}} & 0 & 0 \\ 0 & m - Y_{\dot{v}} & -Y_{\dot{r}} \\ 0 & -N_{\dot{v}} & I_{zz} - N_{\dot{r}} \end{bmatrix}
\begin{bmatrix} \dot{u} \\ \dot{v} \\ \dot{r} \end{bmatrix} =
\begin{bmatrix} X_{u|u|}u|u| + \left(X_{vr} + m\right)vr \\ + X_{rr}rr + X_{Prop} \\ Y_{v|v|}v|v| + Y_{r|r|}r|r| + Y_{uv}uv \\ + \left(Y_{ur} - m\right)ur + Y_{uu\delta_r}u^2\delta_r \\ N_{v|v|}v|v| + N_{r|r|}r|r| + N_{uv}uv \\ + N_{ur}ur + N_{uu\delta_r}u^2\delta_r \end{bmatrix}
\tag{5.10}
$$

The accelerations are then computed by inverting the inertial matrix and multiplying it by the force vector as shown in equation (5.11).

$$\begin{bmatrix} \dot{u} \\ \dot{v} \\ \dot{r} \end{bmatrix} = \begin{bmatrix} m - X_{\dot{u}} & 0 & 0 \\ 0 & m - Y_{\dot{v}} & -Y_{\dot{r}} \\ 0 & -N_{\dot{v}} & I_{zz} - N_{\dot{r}} \end{bmatrix}^{-1} \begin{bmatrix} X_{u|u|}u|u| + (X_{vr} + m)\, vr \\ +X_{rr}rr + X_{Prop} \\ Y_{v|v|}v|v| + Y_{r|r|}r|r| + Y_{uv}uv \\ + (Y_{ur} - m)\, ur + Y_{uu\delta_r}u^2\delta_r \\ N_{v|v|}v|v| + N_{r|r|}r|r| + N_{uv}uv \\ +N_{ur}ur + N_{uu\delta_r}u^2\delta_r \end{bmatrix} \tag{5.11}$$

These accelerations are then numerically integrated along a small time interval Δt to determine the UUV linear and angular velocities, and then integrated again to find the UUV position and heading. Equation (5.12) is Euler's method for numerical integration and is the method used for this research.

$$\begin{aligned} u_{t+1} &= u_t + \dot{u}_t\Delta t \\ v_{t+1} &= v_t + \dot{v}_t\Delta t \\ r_{t+1} &= r_t + \dot{r}_t\Delta t \\ x_{t+1} &= x_t + [u_t \cos\psi - v_t \sin\psi]\Delta t \\ y_{t+1} &= y_t + [u_t \sin\psi + v_t \cos\psi]\Delta t \\ \psi_{t+1} &= \psi_t + r_t\Delta t \end{aligned} \tag{5.12}$$

These equations are ultimately used to determine the new state of the UUV based on the forces and moments acting on the vehicle. This is performed by the uSimMarine app which takes as an input the previous state vector $\mathbf{x}$ and the input vector $\mathbf{u}$ with the propeller thrust X_{Prop} and rudder angle δ_r and returns the new position, speed, and heading of the UUV as a new state vector. The $\sin\psi$ and $\cos\psi$ terms appear in equation (5.12) to convert from the body-fixed coordinate system of the UUV to the inertial coordinate system, which for this study, is fixed to the center of buoyancy of the submarine.

When a UUV operates in close proximity to a moving submarine, the submarine creates a wake and flow field that affects the motion of the UUV. These equations of motion in equation (5.10) that use standard hydrodynamic coefficients do not account for these hydrodynamic interactions between a UUV and a submarine. In order to simulate the UUV motion near a submarine, the equations of motion need to be modified by replacing the UUV body forces and moments with the GP regression surrogate model forces and moments.

5.5 Gaussian Process Regression

To simulate UUV motion near a moving submarine, the hydrodynamic interaction forces and moments acting on the UUV need to be determined each time it changes position, heading, or speed. This means that these hydrodynamic interactions need to be predicted in real time as the UUV maneuvers around the submarine. Because CFD usually takes hours or days to complete a simulation for one specific UUV in one particular position, heading, or speed, a ROM is used to predict these hydrodynamic interactions in real time. GP regression is used to create a surrogate ROM that predicts the surge, sway, and yaw hydrodynamic interaction forces and moments based on the state of the UUV. GP regression also provides estimates for the epistemic uncertainty or errors due to a lack of data. The GP regression model can be expressed as a random function,

$$y = f(x) + \epsilon \tag{5.13}$$

where $x \in \mathbb{R}^d$, $\epsilon \sim \mathcal{N}(0, \sigma^2)$ represents the noise of the model. The function f follows a Gaussian distribution with prescribed mean and covariance function [20]:

$$f(x) \sim \mathcal{GP}(\mu(x), k(x,x')), \tag{5.14}$$

where $\mu(x)$ is the mean and $k(x,x')$ the covariance:

$$\mu(x) = \mathbb{E}[f(x)] \tag{5.15}$$

$$k(x,x') = \mathbb{E}[(f(x) - \mu(x))(f(x') - \mu(x'))] \tag{5.16}$$

GP regression can use one of many different covariance functions, which are also known as kernels. This study uses the popular radial basis function (RBF) kernel with automatic relevance determination:

$$k(x,x') = \exp\left(\frac{-(x-x')^T \lambda^{-1}(x-x')}{2}\right) \tag{5.17}$$

where λ is the diagonal matrix containing the length scales of each input dimension. This kernel is selected because it mimics a Bayesian linear regression model with an infinite number of basis functions [20], which can take the form of any sufficiently smooth output function. Because the output function of the hydrodynamic interaction is unknown and complex, this kernel is opportune to map the output. Automatic relevance determination allows each input dimension to have a different length scale. This is necessary to implement in this GP regression model given the nature of the inputs of the UUV location, speed, size, and heading.

The objective of GP regression is to determine the predicted mean $y(\mathbf{X}_*)$ and covariance $K_{yy}(\mathbf{X}_*, \mathbf{X}'_*)$ for a given set of input-output data. The data set $\mathcal{D}$ =$\{x_i, y_i\}_{i=1}^n$ is used to train the GP regression model where n is the number of samples in the data set. The input and output pairs are notated as $\mathbf{X} = [x_1, ..., x_n] \in \mathbb{R}^{d \times n}$ and $\mathbf{y} = [y_1, ..., y_n] \in \mathbb{R}^n$ where d is the dimension of the input domain. Likewise,

$\mathbf{X}_* = [x_{*1}, ..., x_{*m}] \in \mathbb{R}^{d\times m}$ is a set of m locations for which a prediction is desired. The predicted mean and covariance at a set of points $\mathbf{X}_*$ are listed below as equations (5.18) and (5.19) [20]:

$$y(\mathbf{X}_*) = K(\mathbf{X}_*, \mathbf{X})[K(\mathbf{X}, \mathbf{X}) + \sigma_n^2\mathbf{I}]^{-1}\mathbf{y} \tag{5.18}$$

$$\begin{aligned} K_{yy}(\mathbf{X}_*, \mathbf{X}'_*) = K(\mathbf{X}_*, \mathbf{X}'_*) \\ -K(\mathbf{X}_*, \mathbf{X})[K(\mathbf{X}, \mathbf{X}) + \sigma_n^2\mathbf{I}]^{-1}K(\mathbf{X}, \mathbf{X}'_*) \end{aligned} \tag{5.19}$$

The term σ_n^2 represents the aleatoric uncertainty in the training samples. This is a hyperparameter optimized by gradient descent methods to improve the performance of the GP regression [20]. Additionally, it helps ensure the matrix in brackets in equations (5.18) and (5.19) is well conditioned.

As the UUV changes position, heading, and speed, it experiences different forces and moments due to the hydrodynamic interactions between the vehicles. For this study, terms from the simplified state vector in equation (5.8) are used as inputs to the GP regression model. This allows the surrogate model to predict the hydrodynamic interactions based on changes to the UUV state vector. Much more detail about the setup and development of the GP regression model is provided in chapter 4. Put simply, the GP regression surrogate model takes the state vector, as well as the length and diameter of the UUV, and predicts the UUV surge, sway, and yaw body forces and moments due to the hydrodynamics interactions, which are denoted as X_s, Y_s, and N_s respectively. This is performed by non-dimensionalizing the state vector and UUV length to match the input variables in table 4.2. These are then placed into $\mathbf{X}_*$ from equation (5.18), representing the location for which a prediction of the hydrodynamic interactions is desired. The 100 CFD simulation locations are organized into the data set $\mathbf{X}$ with three distinct labels $\mathbf{y}$, one for each of the surge, sway, and yaw forces and moments. Equation (5.18) is then used to solve for the predicted surge, sway, and yaw body forces and moments due to the hydrodynamics interactions X_s, Y_s, and N_s. These GP regression outputs are incorporated into the equations of motion by replacing the body forces with those predicted by the surrogate. Equation (5.20) shows the modified version of the simplified equations of motion that account for the hydrodynamic interactions.

$$\begin{bmatrix} m - X_{\dot{u}} & 0 & 0 \\ 0 & m - Y_{\dot{v}} & -Y_{\dot{r}} \\ 0 & -N_{\dot{v}} & I_{zz} - N_{\dot{r}} \end{bmatrix} \begin{bmatrix} \dot{u} \\ \dot{v} \\ \dot{r} \end{bmatrix} = \begin{bmatrix} X_s + X_{Prop} \\ Y_s + Y_{uu\delta_r} u^2 \delta_r \\ N_s + N_{uu\delta_r} u^2 \delta_r \end{bmatrix} \tag{5.20}$$

These equations of motion are solved in the uSimMarine app of the MOOS-IvP architecture. Because these equations of motion are embedded in the uSimMarine app, the GP surrogate model also needs to be embedded into this app. This enables the simulator to determine how the hydrodynamic interactions impact the UUV motion and the ability of the UUV autonomy and control systems to overcome these hydrodynamic interactions. Figure 5-3 shows how the GP surrogate model of the hydrodynamic interactions is integrated into the MOOS-IvP simulation architecture.

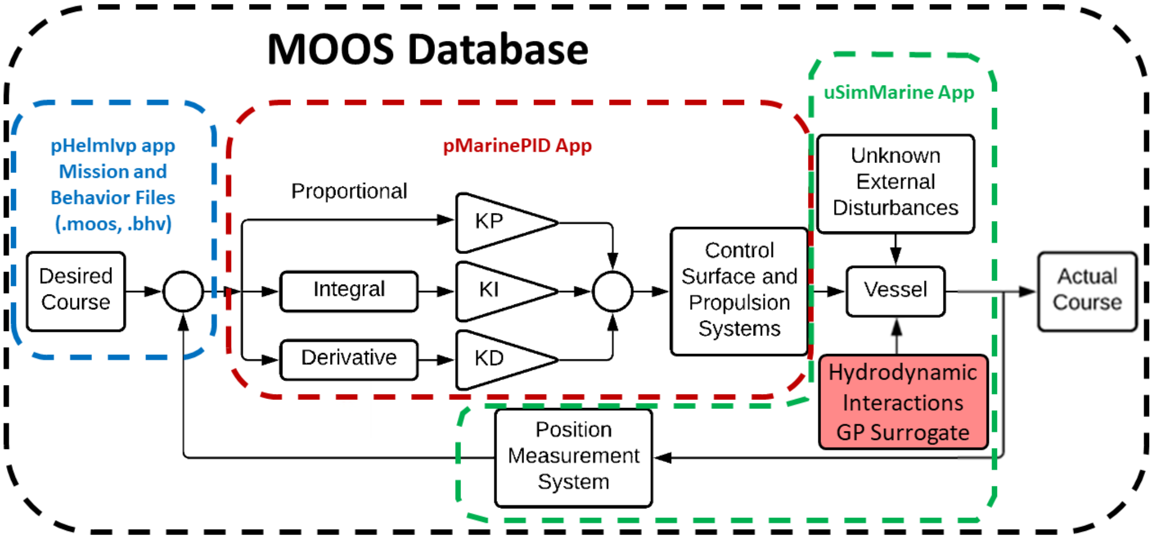

Figure 5-3: Integration of the hydrodynamic interactions GP surrogate into the MOOS-IvP architecture. The GP surrogate is embedded in the uSimMarine app to determine how the hydrodynamic interactions impact the UUV motion.

Now that the hydrodynamic interactions GP regression model has been incorporated into the equations of motion of the uSimMarine app, the UUV control system and autonomous behaviors can be analyzed to evaluate their robustness against these unwanted hydrodynamic interactions.

5.6 Control Theory

The pMarinePID app simulates the UUV PID controller. This app takes in the desired speed and heading from the pHelmIvP app and returns the input vector, which contains the propeller thrust X_{Prop} and rudder angle δ_r necessary to achieve the desired speed and heading. The thrust and rudder angle also depend on the current state of the vehicle. The difference between the desired and current state is known as the error, denoted as $e_u(t)$ and $e_\psi(t)$. The standard PID controller calculates the sum of some proportion of the error, its derivative, and integral as shown in equation (5.21) [15]. The resulting $\tau_{X_{Prop}}$ and τ_{δ_r} represent the necessary change in thrust or rudder angle from the current state. These changes are added to the current thrust and rudder angle to determine new thrust $X_{Prop,t+1}$ and rudder angle $\delta_{r,t+1}$ as outlined in equation (5.21).

$$\begin{aligned}
e_u(t) &= u_d - u \\
e_\psi(t) &= \psi_d - \psi \\
\tau_{X_{Prop}} &= K_{p,X_{Prop}} e_u(t) + K_{d,X_{Prop}} \dot{e_u}(t) \\
&\quad + K_{i,X_{Prop}} \int_0^t e_u(\tau) d\tau \\
\tau_{\delta_r} &= K_{p,\delta_r} e_\psi(t) + K_{d,\delta_r} \dot{e_\psi}(t) \\
&\quad + K_{i,\delta_r} \int_0^t e_\psi(\tau) d\tau \\
X_{Prop,t+1} &= X_{Prop,t} + \tau_{X_{Prop,t}} \\
\delta_{r,t+1} &= \delta_{r,t} + \tau_{\delta_{r,t}}
\end{aligned} \tag{5.21}$$

Each of the K_p, K_d, and K_i constants are often referred to as gains and represent how much the proportional, derivative, and integral terms impact the change to the thrust or rudder angle. The thrust and rudder angles each have their own set of gains. These gains are determined for each vehicle using the Ziegler Nichols method [77]. Ultimately, the pMarinePID app has the input of the desired speed and heading from the desired state vector $\mathbf{x_d}$ along with the UUV state vector $\mathbf{x}$. The app returns the input vector u containing the new propeller thrust $X_{Prop,t+1}$ and rudder angle $\delta_{r,t+1}$.

5.7 Autonomous Behaviors

The autonomous behavior of the UUV is modeled after the MOOS pHelm-IvP waypoint behavior [65]. This waypoint behavior takes the current state of the UUV and determines the desired speed and desired heading. The desired speed specified for a simulation is held constant. However, the desired heading is determined by establishing a series of waypoints, or locations, that the UUV will pass through. Once the UUV passes through a waypoint, it maneuvers toward the next waypoint. An imaginary track-line is established between the previous waypoint and the next waypoint. A perpendicular line between the UUV and the track-line is established. Once this perpendicular intersection point on the track-line is known, a lead point is determined by finding the point at a predetermined distance from the perpendicular intersection point on the track-line in the direction of the next waypoint. This distance is known as the lead distance d_{lead}. The desired heading is then computed by determining the heading of the lead point with respect to the UUV so that the UUV always desires to head toward the lead point. If the lead point extends beyond the next waypoint, the next waypoint becomes the lead point. Figure 5-4 illustrates the waypoints behavior.

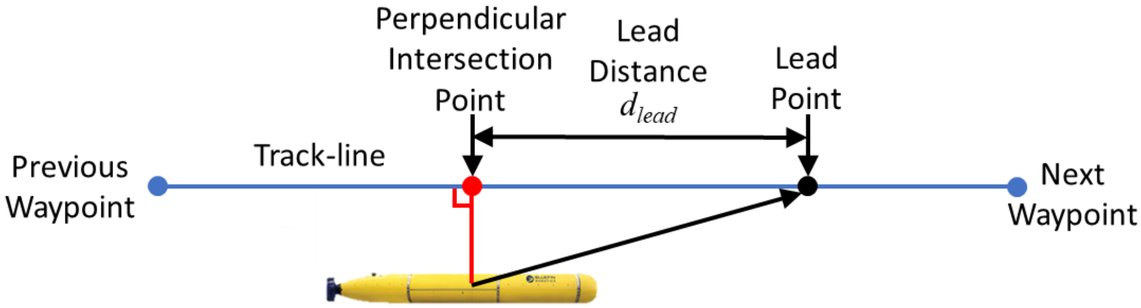

Figure 5-4: Waypoints Behavior: The purpose of this behavior is to traverse a set of waypoints along a track-line. The vehicle steers toward the lead point on the track-line rather than toward the next waypoint. [65]

The waypoints behavior is simulated in the pHelmIvP app. In summary, the pHelmIvP app, which uses the waypoints behavior, takes the state vector of the UUV at a given point $\mathbf{x_t}$ as an input and returns the desired state vector $\mathbf{x_{d,t}}$ containing the desired speed and desired heading. This desired state vector is fed into the pMarinePID app which uses control theory to determine the input vector $\mathbf{u_t}$, which contains the appropriate propeller thrust and rudder angle. This input vector is then fed to the uSimMarine app which uses the equations of motion to determine a new UUV state vector $\mathbf{x_{t+1}}$. This loop is iterated along a small time step Δt to simulate the UUV motion. This process is summarized in figure 5-2.

By incorporating the GP surrogate model into the equations of motion as shown in equation (5.20), a simulation can be performed that accounts for the submarine and UUV hydrodynamic interactions. Figure 5-5 provides an example simulation of a large UUV performing a simple overtaking maneuver near the stern of the submarine with an overtaking velocity of $U_{ot} = 0.25$ m/s and a submarine velocity of $U_{sub} = 1.5$ m/s (≈3 knots).

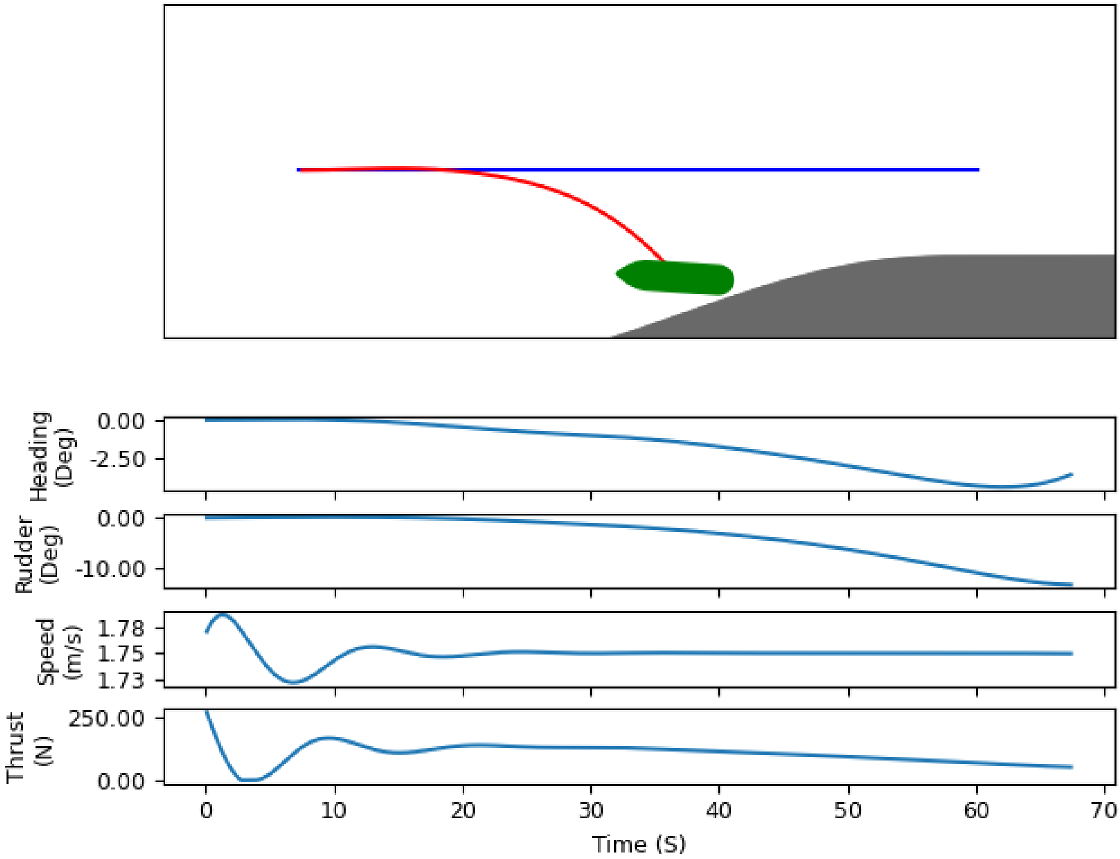

Figure 5-5: The large UUV is unable to overcome the hydrodynamic interactions near the stern of the submarine. This results in a collision.

As the UUV approaches the stern of the submarine, the sway and yaw hydrodynamic interactions cause the UUV to be pulled and rotated toward the submarine which ultimately results in a collision. As the UUV starts to be pulled off course, it responds by positioning the rudder to maneuver the UUV away from the submarine. However, the standard behavior is not responsive enough to overcome these hydrodynamic interactions so the UUV ultimately collides with the submarine.

5.8 Robustness

The main reason for implementing a UUV control system is to allow it to make course corrections from perturbations that take the UUV off course. In addition to the hydrodynamic interactions, there are other sources of perturbation that exist when a UUV is maneuvering. Determining the robustness of the UUV against these perturbations is vital to assess the feasibility of launch and recovery operations. Large-scale perturbations due to ocean eddies and currents occur at large enough time scales and length scales that they do not have a large impact on UUV launch and recovery operations [78]. If a submarine and UUV are operating in an ocean cross current, over time they will drift with the current. Any changes to the current are slow enough and over large length scales that they will not have a large impact on UUV maneuverability. Likewise, small-scale turbulence caused by the vehicles moving through the water will have small enough time and length scales that they will not impact UUV motion [79]. However, the perturbations caused by surface waves are in the time and length scales that may have large impacts on UUV maneuverability.

Ocean waves are often described as being stochastic, meaning that they are random or unpredictable. These waves can be considered stochastic in terms of their amplitude or wave height. The height of ocean waves can vary widely, depending on wind speed, the distance over which the wind blows on the wave, and the sea state of the ocean surface. Ocean waves can also be considered stochastic in terms of their period, or time between waves. Due to this stochastic nature, waves are often described using probability distribution functions or wave spectra. As such, ocean waves are often categorized into different sea states as shown in table 5.1 [80].

Table 5.1: Sea states for the general North Atlantic [80].

Sea State	Significant Wave Height (m)	Period Range (s)	Most Probable Period (s)
0-1	0-0.1	-	-
2	0.1-0.5	3.3-12.8	7.5
3	0.5-1.25	5.0-14.8	7.5
4	1.25-2.5	6.1-15.2	8.8
5	2.5-4.0	8.3-15.5	9.7
6	4.0-6.0	9.8-16.2	12.4

The solution space of the impact of waves on different combinations of UUV size, location, speed, heading, and depth is very large. In order to fully explore this solution space and develop operating envelopes, a large number of UUV simulations needs to be performed. If the waves are modeled as a probability distribution function or spectra, then the impact of the waves on the motion of the UUV is also probabilistic. Implementing the waves in this matter is complex and computationally expensive. Ultimately, the results need to be simplified to a non-probabilistic representation when developing operating envelopes. As such, the waves are implemented in a deterministic manner and modeled as a plane progressive wave using linear wave potential theory. Modeling the waves in this way is common and is also often considered as having the greatest practical significance [14]. This is cheaper and easier to implement and allows for the creation of simpler operating envelopes.

The 2D fluid velocity components due to the waves are defined as u_w and v_w [14]. These fluid velocities are in the inertial coordinate system where u_w is in the direction in which the wave is progressing and v_w is in the direction pointed down toward deeper depths. The significant wave height is defined as the average of the highest 1/3 of the wave heights over a time history. The amplitude A of a wave is 1/2 of the wave height. As such, A is set for each sea state as 1/2 of the largest value in the range of significant wave heights listed in table 5.1 in order to be conservative. The angular frequency $\omega = 2\pi/T$ is also found for each sea state using the most probable period. The wave number $k = 2\pi/\lambda$ is found using the wavelength λ.

The wavelength λ depends on the angular frequency ω of the wave, as well as the dispersion relationship, which depends on the depth to the ocean floor. In this case, the deep water assumption is made meaning that the ocean floor is deeper than $\lambda/2$. This is a safe assumption given the range of possible wavelengths and the requirements for the minimum charted depth of water [68]. This means the dispersion relationship is $k = \omega^2/g$ and the wavelength is found using $\lambda = g\omega^2/(2\pi)$ where g is the acceleration due to gravity. Lastly, x and y represent the location in the flow field where y is the depth.

$$u_w = \omega A e^{ky} \cos(kx - \omega t) \tag{5.22}$$

$$v_w = \omega A e^{ky} \sin(kx - \omega t) \tag{5.23}$$

This flow field is ultimately incorporated into the UUV simulator by converting the flow field into the UUV body-fixed coordinate system and then combining the UUV velocities with these velocities due to the waves from equation (5.22) and (5.23). The following figure is an example illustration of a small UUV traversing a 10 meter trackline operating 50 meters deep in sea state 5 conditions. The UUV is operating at 1.75 m/s (≈3.5 knots) with the inertial frame moving 3 knots, meaning the $U_{ot} = 0.25$ m/s

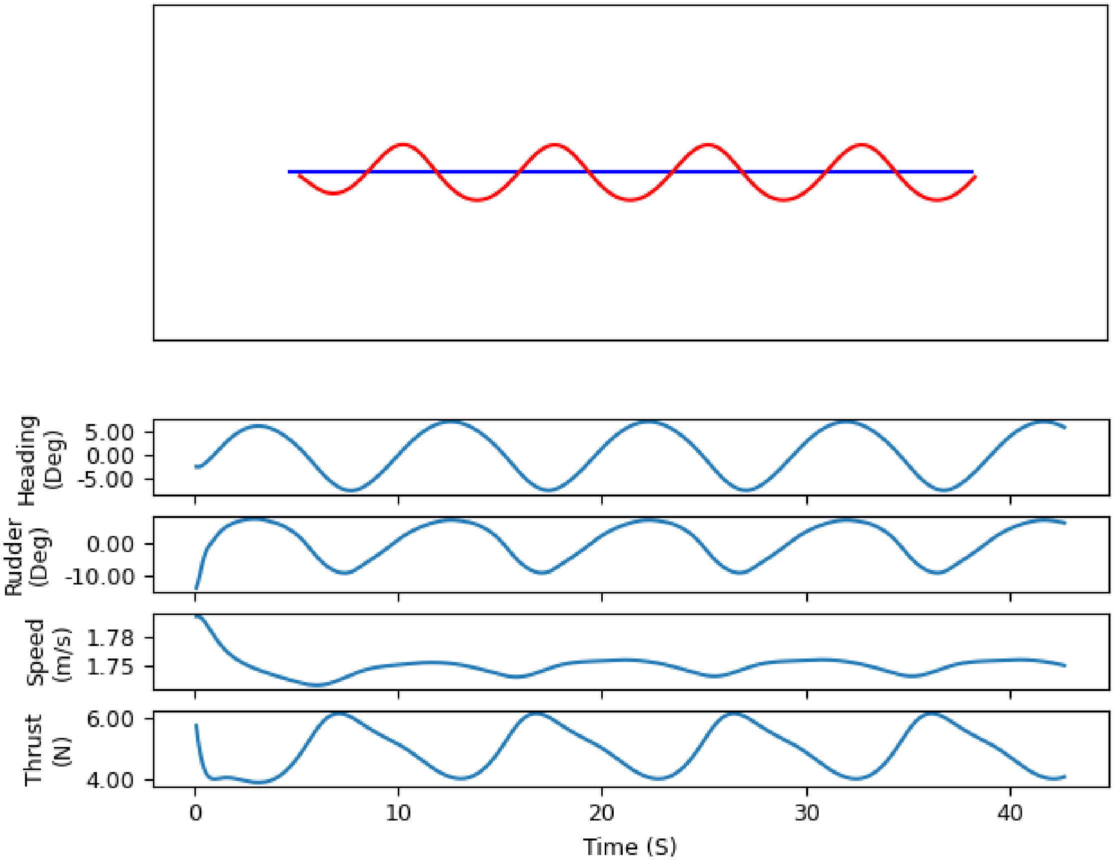

Figure 5-6: A small UUV in sea state 5 at 50 meters deep is pushed by the waves and oscillates around the track-line.

In this high sea state, the UUV is pushed off course by the wave flow field even at 50 meters deep. The autonomous behavior and control system allows for the UUV to course correct, but the waves repeatedly push the UUV off course.

The UUV simulator only uses three degrees of freedom. In order to be conservative, the perturbations caused by the waves are assumed to be in the same plane as the UUV velocities. This causes the UUV to be pushed toward or away from the submarine. This is a conservative approach because it models the worst-case scenario of the direction of fluid velocities due to the wave. This would be analogous to having a UUV operate above a submarine. The waves would push it up or down toward the submarine. If the UUV were to the side of the submarine, these perturbations would cause the UUV to move in a direction orthogonal to the plane between the vehicle axes. Additionally, the submarine is assumed to have no impact on damping the fluid velocity due to the waves. This assumption is made for ease of implementation, but it is a conservative approach representing a worst-case scenario.

5.9 UUV Simulation Setup

This study examined three different UUV sizes: small, medium, and large. The small UUV uses the inertial properties and hydrodynamic coefficients of the Remus 100 [64]. The medium and large UUVs use the corresponding inertial properties and hydrodynamic coefficients of the Naval Postgraduate School (NPS) Autonomous Underwater Vehicle (AUV) II and the Swimmer Delivery Vehicle (SDV) respectively [66, 81, 15]. The submarine in this simulation is the Defense Advanced Research Projects Agency (DARPA) SUBOFF hull that has been scaled up to have a diameter of 34 feet (10.363 meters) [49]. The submarine is simulated at speeds between two and five knots. This is based on the minimum speed a submarine needs to move to have enough flow over the control surfaces to stay controllable and the maximum speed of several UUVs [19].

5.10 UUV Simulation Validation

The UUV simulator is validated against UUV experimental runs to ensure that it is accurately reflecting the real-world physics [64, 66]. One of these real-world experiments is of a Remus 100 UUV performing a step change in rudder angle of four degrees. This scenario is simulated using the process outlined in this research and compared with real-world results. The following figure shows the simulated UUV motion versus the actual Remus 100 motion during a four-degree rudder angle maneuver.

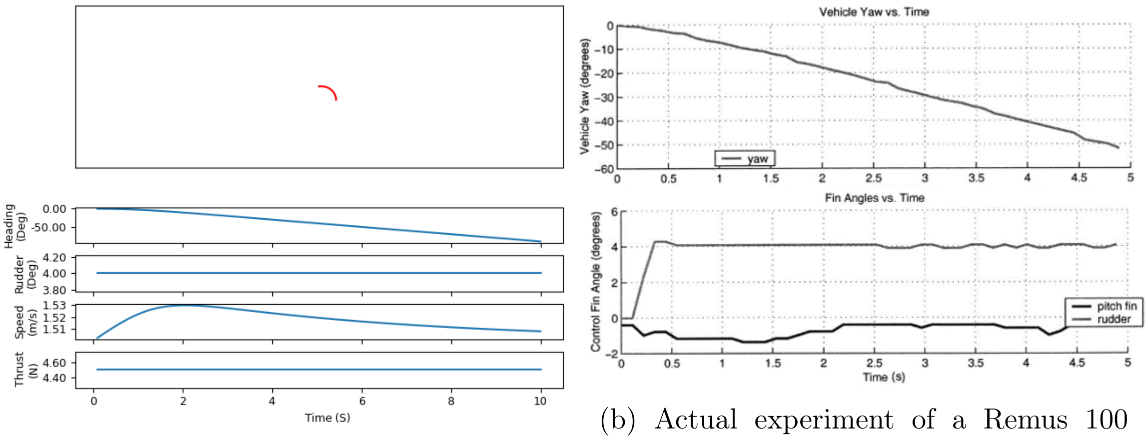

(a) UUV simulation of a Remus 100 with a four-degree step change in rudder angle.

(b) Actual experiment of a Remus 100 with a four-degree step change in rudder angle [64].

Figure 5-7: Validation of the UUV simulator against real-world experiment of a Remus 100 with a four-degree step change in rudder angle. The simulated and actual yaw rates r are nearly identical.

As seen in figure 5-7, the experiment of the Remus 100 UUV performing a step change in rudder angle of four degrees found that the yaw rate is about -10 degrees per second [64]. The UUV simulator predicts a yaw rate of -10.04 degrees per second.

Similarly, an experiment on the Naval Postgraduate School (NPS) Autonomous Underwater Vehicle (AUV) II was performed using rudder commands that alternated by ±15 degrees every 45 seconds [66]. These rudder commands resulted in a yaw rate of about ±7.5 degrees per second. The UUV simulator predicted a yaw rate of about ±7.24 degrees per second. This demonstrates that the UUV simulator is able to replicate the results experienced by real-world UUVs.

In order to validate the autonomy and control functions of the UUV simulator, a simulation is performed and compared against a standard "alpha" mission in the MOOS-IvP simulator [65]. This mission is a series of waypoints in a pentagon shape. The following figure shows the performance of the UUV simulator against the validated MOOS-IvP simulator.

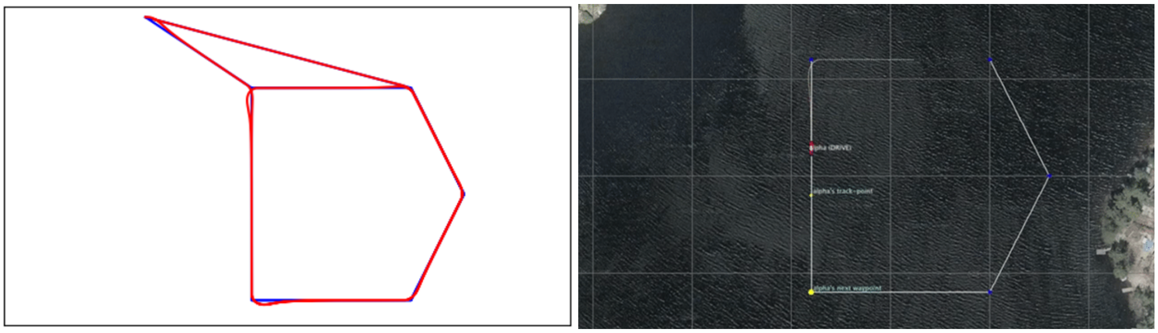

(a) UUV simulation of the alpha mission.

(b) MOOS-IvP simulation of the alpha mission [65].

Figure 5-8: Validation of the UUV simulator against the MOOS-IvP simulator for a series of waypoints known as the alpha mission.

The UUV simulator is able to perform the alpha mission just like the MOOS-IvP simulator. Both simulators have the UUV navigate through the series of waypoints with the UUV slightly overshooting the track-line as it goes around the corners, but then quickly realigns with the track-line. This validates the autonomy and control functions of the UUV simulator.

5.11 Results

5.11.1 Force and Moment Maps

The GP regression surrogate model shows that the regions with the largest hydrodynamic interactions are near the bow and stern of the submarine [73]. When a UUV operates in these regions, there is a high risk of collision. Figure 5-9 shows the non-dimensional hydrodynamic interaction surrogate sway and yaw coefficients Y_s' and N_s' experienced by the UUV in various locations around the submarine. A negative sway and yaw cause the UUV to be sucked toward and the UUV bow to be rotated toward the submarine respectively. This figure is for a large UUV that is one meter in diameter and eight meters long traveling at 1.75 m/s (≈3.5 knots) parallel to the submarine. The surrogate model is capable of altering these additional parameters and generating new maps, but the added dimensionality is not shown in order to be concise and simply illustrate regions with large hydrodynamic interactions.

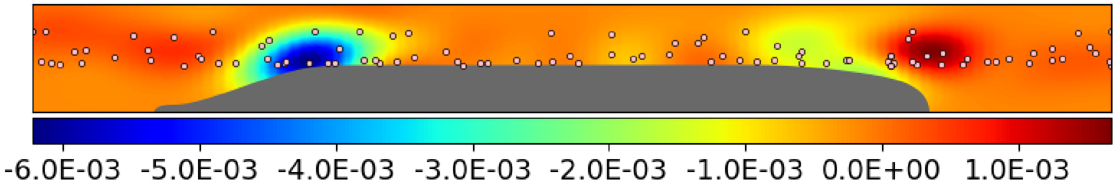

(a) Colormap of sway coefficient Y_s' at various locations around the submarine at a fixed $U = 3.5$ knots, $\phi = 0°$, $D_{Sub}/D_{UUV} = 10$, and $L/D_{UUV} = 8$. Regions around the bow of the submarine push the UUV away from the submarine while regions around the stern of the submarine pull the UUV toward the submarine.

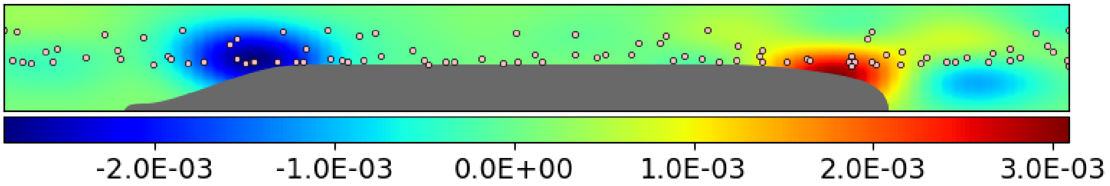

(b) Colormap of yaw coefficient N_s' at various locations around the submarine at a fixed $U = 3.5$ knots, $\phi = 0°$, $D_{Sub}/D_{UUV} = 10$, and $L/D_{UUV} = 8$. Regions around the bow of the submarine rotate the bow of the UUV away from the submarine while regions around the stern of the submarine rotate the UUV bow toward the submarine.

Figure 5-9: Colormaps of the hydrodynamic interaction sway and yaw coefficients Y_s' and N_s' at different lateral and longitudinal positions with respect to the submarine. The dots represent the locations of a CFD simulation [73].

5.11.2 Results for Standard UUV

Due to the low cost of running the GP surrogate model, many simulations may be performed in various positions around the submarine and under various conditions. This allows for the creation of a safe operating envelope, a region under specified conditions in which the UUV is capable of overcoming the hydrodynamic interactions. Likewise, a region can be identified in which a collision is predicted. A close call is defined as a case in which the UUV comes within one UUV diameter of the submarine without a collision, or when the UUV is directly in front of or behind the submarine.

A large stray is defined as the case when the hydrodynamic interactions cause the UUV to stray away from its track-line by more than one meter. Figure 5-10 illustrates the operating envelope for the small, medium, and large UUV that are traveling at the same speed as the submarine at $U_{sub} = 1.5$ m/s ($\approx$3 knots) with $d_{lead} = 3L_{UUV}$ and no waves.

(a) Small UUV operating envelope

(b) Medium UUV operating envelope

(c) Large UUV operating envelope

Figure 5-10: Operating envelope for the small, medium, and large UUVs that are traveling at the same speed as the submarine at $U_{sub} = 1.5$ m/s ($\approx$3 knots) with $d_{lead} = 3L_{UUV}$ and no waves.

Figure 5-10 shows that all three of the UUVs have issues overcoming the hydrodynamic interactions illustrated in figure 5-9. All three different size UUVs have large operating regions near the stern of the submarine that result in collisions. Additionally, the large hydrodynamic interactions near the bow of the submarine cause all three size UUVs to stray large distances from the track-line, even though they do not result in a collision with the submarine. This means that UUVs operating with the standard waypoint behavior will struggle to perform overtaking maneuvers without experiencing large strays or collisions. As such, launch and recovery architectures and schemes may be more successful if implementing a lateral approach to the parallel mid-body section of the submarine.

There are several parameters, such as U_{ot}, U_{sub}, and d_{lead}, which have an influence on how the hydrodynamic interactions impact the UUV. As such, many more operating envelopes could be created for a range of different scenarios. However, after sampling several different scenarios, varying the U_{ot} and U_{sub} had a very small impact on the operating envelope compared to d_{lead}. This is likely because U_{ot} and U_{sub} have narrow ranges for launch and recovery operations and the vehicle maneuverability is relatively constant over this range. However, d_{lead} influences the vehicle behavior, rather than making small adjustments to the underlying physical simulation setup. Figure 5-11 shows how different values of d_{lead} influence the operating envelope for the small UUV. These operating envelopes are for UUVs at the same speed as the submarine at $U_{sub} = 1.5$ m/s (≈3 knots) and no waves, just like figure 5-10.

(a) Small UUV operating envelope with $d_{lead} = L_{UUV}$

(b) Small UUV Operating Envelope with $d_{lead} = 3L_{UUV}$

(c) Small UUV Operating Envelope with $d_{lead} = 5L_{UUV}$

Figure 5-11: Impact of d_{lead} on the operating envelopes for the small UUV traveling at the same speed as the submarine at $U_{sub} = 1.5$ m/s (≈3 knots) with no waves. A smaller d_{lead} results in a larger safe operating envelopes.

As the d_{lead} decreases, the unsafe regions around the submarine decrease in size. Placing the lead point closer to the UUV allows the UUV to more aggressively pursue the track-line, perform better against the hydrodynamic interactions, and expand the safe operating region. This trend also exists for medium and large UUVs. However, the unsafe regions are still large enough to present problems with launch and recovery operations especially if overtaking maneuvers are involved. Adjusting d_{lead} alone is not enough to overcome the hydrodynamic interactions.

5.11.3 Effects of Waves

Determining the robustness of the UUV against perturbations is important to the investigation of the UUV maneuvering capability during launch and recovery. Ocean waves provide the most applicable means of large perturbations experienced by the UUV. These perturbations caused by ocean waves are incorporated into the UUV motion simulator. In order to be conservative, these perturbations are assumed to be in the worse case direction that pushes the UUV toward or away from the submarine, rather than in an orthogonal direction. These perturbations also vary in magnitude based on the sea state and operating depth of the UUV. The following figure shows how the operating envelopes of the different size UUVs are affected by the ocean waves. The waves are sea state 6 and the UUV operating depth is 50 meters. The lead distance is $d_{lead} = 3L_{UUV}$ just like figure 5-10.

(a) Small UUV operating envelope in sea state 6 at 50 meters deep.

(b) Medium UUV operating envelope in sea state 6 at 50 meters deep.

(c) Large UUV operating envelope in sea state 6 at 50 meters deep.

Figure 5-12: Operating envelopes for different size UUVs in sea state 6 at a depth of 50 meters.

When compared to the no-wave condition in figure 5-10, the operating envelope at sea state 6 at 50 meters is drastically reduced. For the small UUV, the operating region that results in a collision with the submarine is very large and entirely encompasses the submarine. This drastically reduces the chance of a successful launch or recovery operation. The medium UUV also has an increase in the size of the collision regions around the submarine, but the remainder of the area results in large strays. This means that the medium UUV may not collide with the submarine but will stray by more than one meter from the track-line due to the waves. The large UUV has a reduction of the safe operating region compared to figure 5-10, but is much more robust to the wave perturbations than the smaller UUVs. This is a good demonstration of the square-cube law. Fortunately, sea states of 6 or above occur less than 27% of the time, and vessels try to avoid such rough seas so this case represents a relatively strong perturbation [82]. Additionally, 50 meters in depth is likely near the minimum depth at which launch and recovery operations will take place in order to maintain vertical separation from surface vessels [68]. However, UUV launch and recovery can be performed at deeper depths based on the maximum depth of the UUV in order to reduce the impact of the waves. The Remus 100 has a maximum rated depth of 100 meters so operating below this is unfeasible. The following figure illustrates the same sea state 6 and other parameters as figure 5-12, but the UUV is now operating at a depth of 90 meters.

(a) Small UUV operating envelope in sea state 6 at 90 meters deep.

(b) Medium UUV operating envelope in sea state 6 at 90 meters deep.

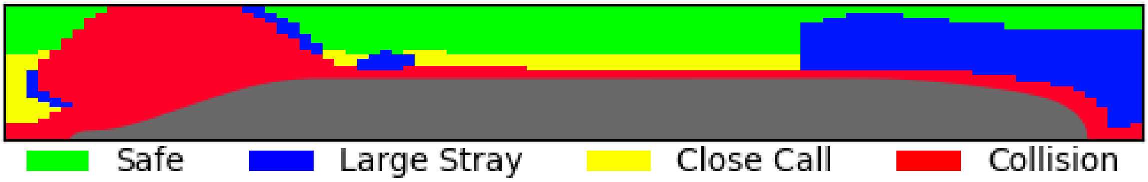

(c) Large UUV operating envelope in sea state 6 at 90 meters deep.

Figure 5-13: Operating envelopes for different size UUVs in sea state 6 at a depth of 90 meters.

Figure 5-13 shows a large increase in the safe operating regions for the small and medium size UUV compared to figure 5-12. By operating 40 meters deeper, the waves have much less of an impact on the UUV motion and make the chances of successful launch or recovery much more likely.

At lower sea states, the vehicles are much more capable of overcoming the perturbations due to the ocean waves. Even at sea state 5 with a depth of 50 meters, the operating envelopes of the UUVs are much better than those at sea state 6. Figure 5-14 shows the operating envelopes for the different size UUVs at sea state 5 and 50 meters deep.

(a) Small UUV operating envelope in sea state 5 at 50 meters deep.

(b) Medium UUV operating envelope in sea state 5 at 50 meters deep.

(c) Large UUV operating envelope in sea state 5 at 50 meters deep.

Figure 5-14: Operating envelopes for different size UUVs in sea state 5 at a depth of 50 meters.

These operating envelopes look much more like the case with no waves in figure 5-10 than the case in sea state 6 at 50 meters deep, especially for the small and medium UUVs. The UUVs are much more capable of overcoming these perturbations than those of sea state 6 at 50 meters. The ocean waves are at sea state 5 or lower more than 73% of the time.

Overall, the UUV autonomous behaviors and control system are relatively robust to ocean waves. At the minimum likely operating depth for launch and recovery operations in sea state 5, the UUVs have similar operating envelopes as those with no waves. Once sea state 6 is reached, the small and medium UUV experience large strays or collisions, but this can be drastically mitigated by operating at lower depths where the impacts of the waves decay away.

5.12 Conclusion

Determining the hydrodynamic interaction forces and moments between a UUV and submarine in real time is essential to simulate UUV motion during launch and recovery operations. Simplified potential flow simulators can be solved very quickly, but fail to capture the accurate physics of CFD simulations, which are too computationally expensive to be solved in real-time. A GP regression surrogate model is developed that is capable of predicting the UUV and submarine hydrodynamic interactions in real time. A method of incorporating a GP surrogate model into a UUV motion simulator is developed in order to simulate the impact of the hydrodynamic interactions between the two vehicles. This enables the use and evaluation of the UUV autonomous behavior and control system against the hydrodynamic interactions. Because this can be simulated rapidly, this allows for the creation of safe operating envelopes in which the UUV is capable of overcoming the hydrodynamic interactions. Because to its low computational cost and high simulation speed, this simulation approach may also be further leveraged to develop new UUV autonomous behaviors that incorporate the GP surrogate model and become capable of overcoming the adverse predicted hydrodynamic interactions.

The simulations of how the hydrodynamic interactions impact the UUV motion show that there are regions near the bow and stern of the submarine just beyond the parallel mid-body section that result in either a large straying from the track-line or in collisions between the two vehicles. These unsafe operating regions extend laterally from the bow and stern of the submarine so certain overtaking maneuvers may not be feasible with standard UUV autonomous behaviors. Also, lateral approaches prove problematic to standard UUV autonomous behaviors because they do not account for the moving inertial frame of the submarine so the UUV has large strays from the track-line. While waves provide perturbations that have the potential to be problematic, it is not until sea state 6 at the minimum likely depth of 50 meters deep that these perturbations have a significant impact on the safe operating envelopes of the vehicles. Sea states of 5 or lower have little impact on the operating envelope at this depth. Also, at sea state 6, operating deeper around 90 meters causes the UUV to experience significantly less impact from the waves so the safe operating envelope is comparable to that of lower sea states.

THIS PAGE INTENTIONALLY LEFT BLANK

Chapter 6

Developing Autonomous Behaviors to Overcome Hydrodynamic Interactions

6.1 Introduction

In chapter 4, a GP surrogate model is created that predicts the hydrodynamic interactions between a UUV and a moving submarine. In chapter 5, this GP surrogate model is integrated into the equations of motion of a UUV simulator in order to determine how these hydrodynamic interactions impact the motion of the UUV as it maneuvers around the submarine. This UUV simulator is used to develop safe operating envelopes around the submarine. There are regions around the submarine in which the existing UUV autonomous behaviors and control system are capable of overcoming the hydrodynamic interactions. However, these safe operating regions are restrictive, especially in overtaking maneuvers where the UUV is near the bow or stern of the submarine.

In an attempt to expand the safe operating region around the submarine, the GP surrogate model can also be integrated into the autonomous behaviors of the UUV and not just the equations of motion. Because the GP surrogate can resolve the hydrodynamic interactions in real-time, the UUV can determine the forces and moments fast enough to allow the control system to account for these unwanted forces and moments. The UUV can be enabled to determine new a new desired heading or speed that compensates for the hydrodynamic interactions. By using the GP surrogate to anticipate the unwanted hydrodynamic interactions, new autonomous behaviors may be developed that are better at overcoming these hydrodynamic interactions and staying on course. These new behaviors have the potential to expand the safe operating regions around the submarine and better enable the launch and recovery of UUVs from submarines.

6.2 Approach

Section 5.5 and figure 5-3 show how the GP surrogate of the hydrodynamic interactions is integrated into the UUV autonomy and control architecture. To review, the hydrodynamic interactions GP surrogate was only incorporated into the equations of motion and not into the autonomous behaviors. This approach taken in section 5.5 allows the simulation of how the UUV responds to these hydrodynamic interactions. In order for the UUV to anticipate the unwanted hydrodynamic interactions, the GP surrogate model needs to be embedded into the autonomous behaviors to allow the UUV to adjust its desired course and speed based on these hydrodynamic interactions. This enables the development of new autonomous behaviors capable of better overcoming these unwanted hydrodynamic interactions. Building off of figure 5-3, figure 6-1 shows how the GP surrogate model of the hydrodynamic interactions is integrated into the autonomous behavior pHelmIvP app of the MOOS-IvP simulation architecture.

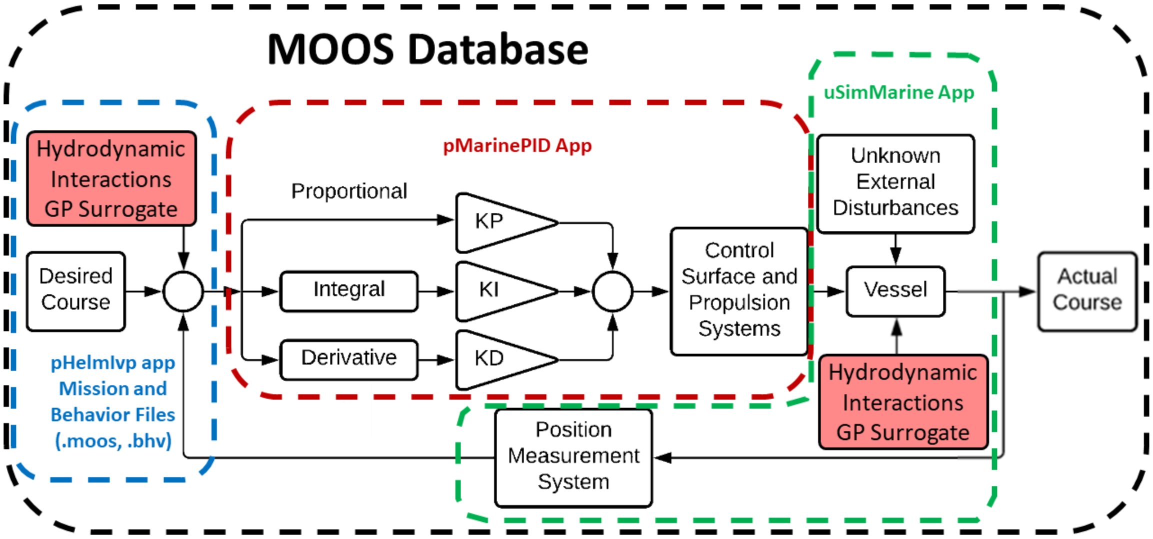

Figure 6-1: Integration of the hydrodynamic interactions GP surrogate into the autonomous behaviors of the MOOS-IvP architecture. The GP surrogate is also embedded in the pHelmIvP app to enable the development of new autonomous behaviors capable of better overcoming unwanted hydrodynamic interactions.

6.3 Autonomous Behaviors

6.3.1 N_{uv} Compensating Behavior

The GP regression surrogate model is capable of determining the hydrodynamic interaction forces and moments in real time. This real-time modeling enables the hydrodynamic interactions to be incorporated into the equations of motion to determine how a UUV responds to these unwanted forces and moments. Additionally, this real-time modeling capability can be incorporated into the autonomous behaviors of the UUVs. If the UUV can anticipate the unwanted hydrodynamic forces and moments, new autonomous behaviors may be developed that determine a new desired heading and speed capable of better overcoming the hydrodynamic interactions and staying on course.

Figure 5-5 shows how the UUV is not responsive enough to overcome the hydrodynamic interactions between the submarine and UUV, which results in a collision. The UUV is inherently reactive because it only begins to course correct after it is pulled away from the track-line. By the time the UUV begins to stray significantly from the track-line, the standard waypoints behavior and UUV control system do not produce a strong enough response to prevent a collision. Rather than being reactive to the hydrodynamic interactions, the autonomous behavior can be altered to be proactive. Because the surrogate model is capable of predicting the hydrodynamic interaction forces and moments based on the current state of the UUV, the forces and moments can be anticipated before waiting for the UUV to stray off course and then try to recover.

In order to allow the UUV to anticipate hydrodynamic interactions, the GP surrogate model is integrated into the pHelmIvP app, as shown in figure 6-1. This app simulates the autonomous behavior of the UUV and is responsible for computing its desired speed and heading. The GP surrogate model computes the predicted hydrodynamic interaction surge, sway, and yaw forces and moments on the vehicle based on its current state. If the UUV knows what hydrodynamic interaction forces and moments it will experience, it can adjust its desired speed and/or heading appropriately in order to stay on course. This enables the desired heading or desired speed to take into account the predicted impact of these forces and moments and keep the UUV on course.

Because there are multiple hydrodynamic interaction forces and moments acting on the UUV, there is no single UUV state that can offset all of the surge, sway, and yaw forces and moments at the same time. Additionally, there are multiple ways in which the GP surrogate could be used to develop an autonomous behavior for the UUV. By exploring which of these forces or moments has the largest impact on the ability of the UUV to stay the course, the surge force is consistently the least influential force and the yaw moment has the largest influence. After exploring many different potential autonomous behaviors, the best case for which the UUV could overcome the hydrodynamic interactions and stay on course is by adjusting the desired heading to offset the hydrodynamic interaction yaw moment. The scheme by which this offset is determined will be referred to as N_{uv} compensation. This scheme is founded on the concept of the munk moment. The munk moment is a destabilizing moment experienced by a UUV in steady translation. When the flow is at a slight angle from the forward direction of the vehicle, this results in a munk moment [14, 15]. This moment is destabilizing because the resulting munk moment will cause the UUV to want to rotate away from being parallel with the flow. This destabilizing moment usually means that a long slender object, like a UUV, is only stable when moving with its broadside to the flow. As such, the control surfaces are necessary to keep a UUV directionally stable.

The idea behind N_{uv} compensation is to place the UUV in such a desired state that the yaw moment of the UUV in this state offsets the hydrodynamic interaction yaw moment predicted by the GP model N_s at this location near the submarine. This means that a new compensated desired heading needs to be determined. This is found by using the N_{uv} coefficient of the UUV to solve for a compensated desired heading angle $\psi_{d,comp}$. This is achieved by first solving for a theoretical compensated sway velocity v_{comp} and then determining the theoretical heading angle that would produce this sway velocity. The derivation of this compensated desired heading angle is as follows

$$\begin{aligned} \gamma N_s &= N_{uv} u_d v_{comp} \\ \therefore v_{comp} &= \frac{\gamma N_s}{N_{uv} u_d} \\ \Delta\psi = \tan^{-1}\left(\frac{u_d}{v_{comp}}\right) &= \tan^{-1}\left(\frac{\gamma N_s}{N_{uv} u_d^2}\right) \\ \psi_{d,comp} &= \psi_d + \Delta\psi \end{aligned} \tag{6.1}$$

where γ is a factor that can be tuned as necessary and the desired speed u_d and desired heading ψ_d are the outputs from the standard waypoints behavior of the pHelmIvP app. Figure 6-2 is the same simulation setup as figure 5-5 and shows a comparison of the standard waypoints behavior and a UUV that is using N_{uv} compensation with

$\gamma = 1$.

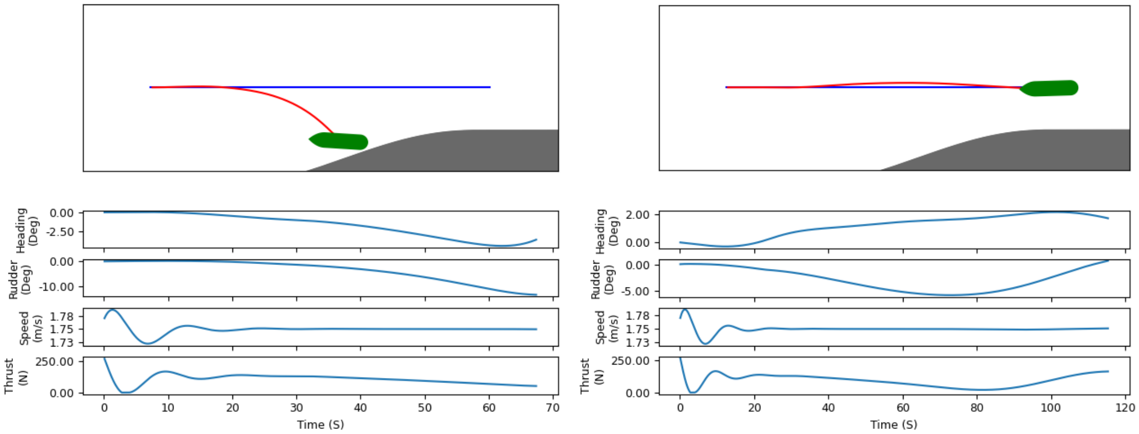

(a) Standard Waypoints Behavior: The large UUV using the standard waypoints behavior is unable to overcome the hydrodynamic interactions near the stern of the submarine. This results in a collision.

(b) N_{uv} Compensating Behavior: Due to the N_{uv} compensation, the large UUV is now able to anticipate and overcome the hydrodynamic interactions near the stern of the submarine and avoid the impending collision.

Figure 6-2: Comparison of standard waypoint behavior and the N_{uv} compensating behavior of a large UUV performing a simple overtaking maneuver near the stern of the submarine with an overtaking velocity of $U_{ot} = 0.25$ m/s and a submarine velocity of $U_{sub} = 1.5$ m/s (≈3 knots). The standard waypoints behavior results in a collision while the N_{uv} compensating behavior results in success.

By using N_{uv} compensation, the UUV adjusts the desired heading to be rotated farther away from the submarine. This new heading overcomes the hydrodynamic interaction that wants to rotate the bow of the UUV toward the submarine. Because N_{uv} compensation anticipates this hydrodynamic interaction, the UUV is able to overcome it and avoid the impending collision. Rather than waiting for the UUV to drift off course and then trying to course correct, the N_{uv} compensating behavior changes the desired heading so that the yawing moment at that desired heading offsets the yaw moment of the hydrodynamic interaction. This allows the UUV to begin to adjust its course much earlier and ultimately successfully stay on course.

6.3.2 Modified Waypoints Behavior

The standard waypoints behavior establishes the inertial reference frame as an earth-fixed coordinate system. However, in order to study the hydrodynamic interactions between a submarine and UUV, the inertial reference frame is fixed to the center of buoyancy of the submarine. Because the submarine is constantly moving to maintain flow across the control surfaces in order to stay in control, the waypoints are not fixed to the earth and have significant flow through them. This submarine velocity U_{sub} has a significant impact on the UUV as it tries to navigate to a waypoint. This is analogous to having an earth-fixed waypoint with a strong current passing through it. The standard waypoint behavior is not designed to handle a significant current passing through the waypoints. In the event that the track-line is parallel to U_{sub}, like in an overtaking maneuver, the standard waypoint behavior performs well. However, when there is flow that crosses the track-line, the UUV is taken way off course. Figure 6-3 illustrates how a UUV behaves near a submarine moving forward. The blue line is the track-line between waypoints while the red line tracks the position of the UUV over time. Initially, the UUV is traveling parallel to the submarine. As the UUV desires to head down along the vertical track-line, it changes its heading to a maximum of about 60 degrees toward the submarine to advance toward the next waypoint. When the UUV is at this heading, the large cross-flow causes the UUV to get pushed significantly off of the track-line. When the track-line is parallel to U_{sub}, the UUV is able to stay on the track-line.

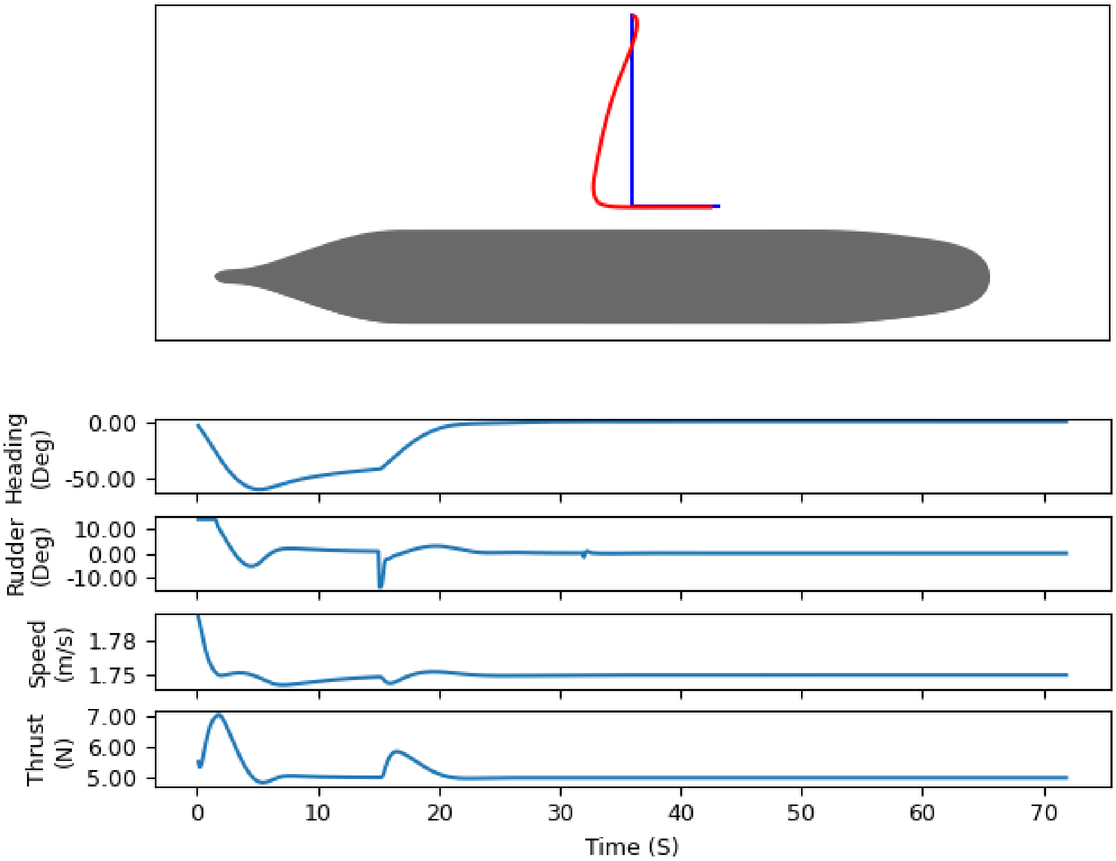

Figure 6-3: Demonstration of the standard waypoints behavior with a moving submarine. The large cross flow pushes the UUV off course when not moving parallel to the submarine.

This problem is addressed by creating a modified waypoint behavior. The modified waypoint behavior adjusts the position of the lead point based on the submarine speed. This can also be thought of in an earth-fixed coordinate system as adjusting the lead point based on a known constant current through the waypoints. Rather than place the lead point on the track-line at d_{lead} from the perpendicular intersection point, a new position is calculated for the lead point. This location is calculated by moving the lead point by d_{lead} from the perpendicular intersection point in the direction of U_{sub}. Additionally, the lead point is moved in the direction perpendicular to U_{sub} towards the next waypoint by a distance known as the lead offset d_{off}. Figure 6-4 shows how the lead point is determined. The angle between U_{sub} and the track-line is denoted as β.

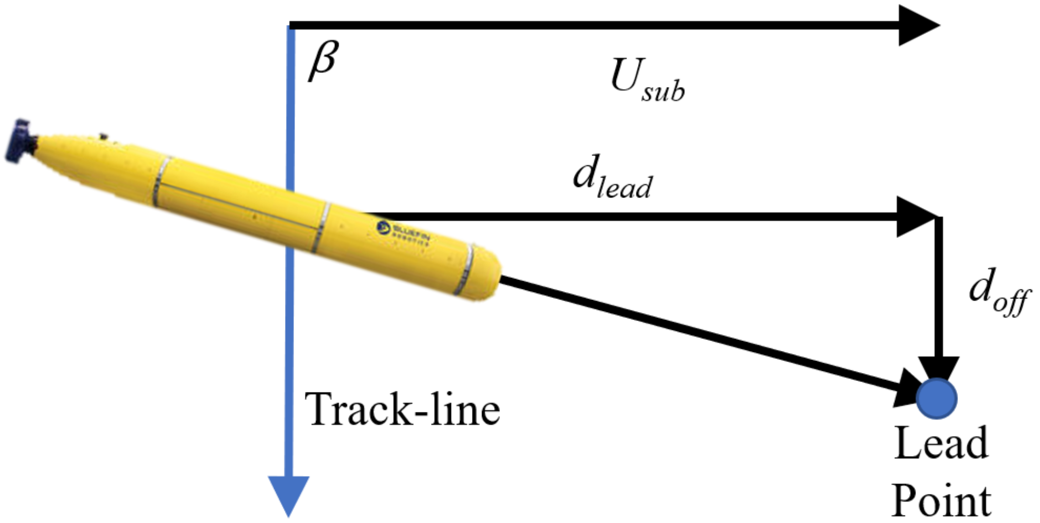

Figure 6-4: Modified Waypoints Behavior: The position of the lead point is changed from the standard waypoint behavior. This enables the UUV to stay on the track-line despite having a large cross flow that overwhelms the standard waypoint behavior.

This lead offset d_{off} is determined using equation (6.2).

$$d_{off} = \frac{\alpha d_{lead} U_{ot} \sin(\beta)}{U_{sub}} \tag{6.2}$$

where α is a parameter between zero and one that specifies how quickly the UUV transverses the track-line in the direction perpendicular to the cross flow. Also, recall that the relative speed between the UUV and submarine is denoted as $U_{ot} = U_{UUV} - U_{sub}$.

While modifying the position of the lead point appropriately adjusts the desired heading, it does not account for the desired speed of the UUV and fails to allow the UUV to accelerate or decelerate to follow the track-line. This ability is added by developing a speed policy behavior for the UUV where the speed policy correction factor is denoted as ε in equation (6.3).

$$U_{UUV} = U_{sub} + U_{ot} \cos(\beta) + \varepsilon \tag{6.3}$$

If the UUV lags behind the track-line in the direction of U_{sub}, then the U_{UUV} increases.

If the UUV leads the track-line, U_{UUV} decreases. The amount by which the U_{UUV} is adjusted is the speed policy correction factor ε, which is outlined in equation (6.3). The ε is established according to the U_{ot}, the length of the UUV L_{UUV}, and the distance between the UUV and the perpendicular intersection point d_{perp}. The policy is analogous to a saturated proportional gain and is set such that the maximum ε is achieved when the UUV lags the track-line in the direction of U_{sub} by a distance of L_{UUV}. Figure 6-5 shows this non-dimensionalized speed policy correction factor.

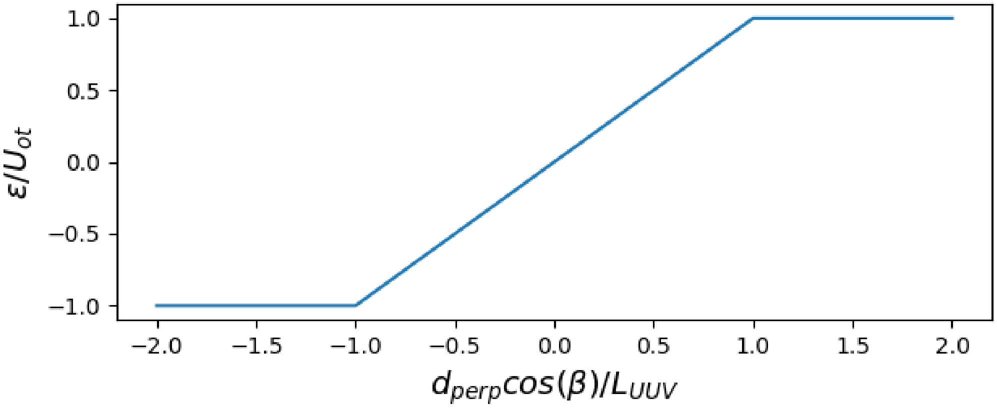

Figure 6-5: Speed Policy: This policy shown in non-dimensional terms allows the UUV to accelerate or decelerate when the cross flow causes the UUV to fall behind or overshoot the track-line.

In order to compare the standard and the modified waypoints behavior, a test simulation is conducted for a small UUV, i.e. the REMUS 100. The course is to maneuver around a series of octagonally arranged waypoints with a U_{sub} of 1.5 m/s (≈3 knots), U_{ot} of 0.25 m/s, and α of 1. Figure 6-6 shows a comparison of the standard and modified waypoints behavior.

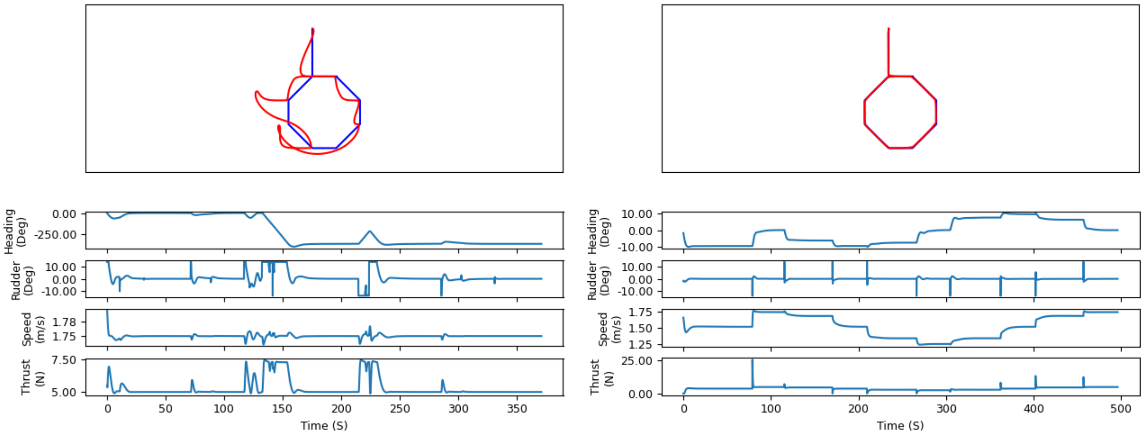

(a) Standard Waypoints Behavior: This behavior is not resistant to the cross flow. This causes the UUV to be pushed off course and even get turned around.

(b) Modified Waypoints Behavior: This behavior is resistant to the cross flow, even at all of the different course trajectories.

Figure 6-6: Comparison of standard and modified waypoints behavior. Unlike the standard waypoints behavior, the modified waypoint behavior enables the UUV to stay on course across all course trajectories despite the large cross flow.

The standard waypoints behavior is significantly affected by the cross-flow. The simulation using the standard waypoints behavior even resulted in the UUV missing one of the waypoints and having to circle back and get it. However, the modified waypoints behavior shows how the UUV is able to account for the cross flow and stay on its track-line. The UUV only needs to orient between ±10 degrees in order to utilize the cross flow to move laterally. This approach prevents the UUV from experiencing the large strays seen by the standard waypoints behavior.

6.4 Results

6.4.1 Results for N_{uv} Compensating Behavior

As discussed previously, N_{uv} compensation is a method by which the GP surrogate model of the hydrodynamic interactions is used to influence the UUV autonomous behavior by determining a new heading angle $\psi_{d,comp}$ that compensates for the hydrodynamic interactions. Figure 6-2 provide an example of how this N_{uv} compensation is able to allow the UUV to account for and overcome the hydrodynamic interactions. This results in the UUV staying on track and avoiding the impending collision with the submarine.

This approach also enables the N_{uv} compensation to be simulated very rapidly for UUVs at various locations around the submarine, which allows for the development of new operating envelopes. Figure 6-7 represents the new N_{uv} compensated operating envelopes. These are for UUVs at the same speed as the submarine at $U_{sub} = 1.5$ m/s (≈3 knots) with $d_{lead} = 3L_{UUV}$ and no waves, just like figure 5-10.

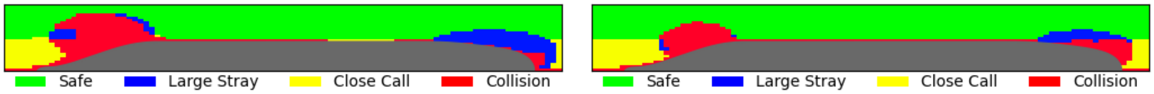

(a) Small UUV operating envelope *without* N_{uv} compensation

(b) Small UUV operating envelope *with* N_{uv} compensation

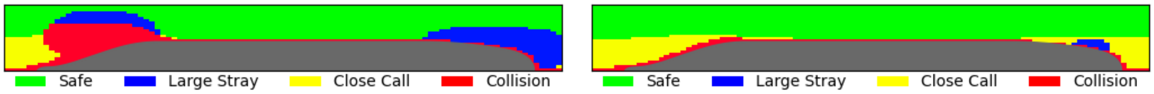

(c) Medium UUV operating envelope *without* N_{uv} compensation

(d) Medium UUV operating envelope *with* N_{uv} compensation

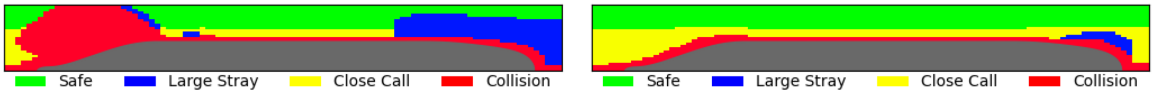

(e) Large UUV operating envelope *without* N_{uv} compensation

(f) Large UUV operating envelope *with* N_{uv} compensation

Figure 6-7: Operating envelopes for the small, medium, and large UUVs with and without N_{uv} compensation. The UUVs are traveling at the same speed as the submarine at $U_{sub} = 1.5$ m/s (≈3 knots) with $d_{lead} = 3L_{UUV}$ and no waves. The N_{uv} compensation increases the safe operating region around the submarine.

The use of N_{uv} compensation drastically reduces the collision and large stray regions for the UUVs. This N_{uv} compensation also provides a significant increase to the size of the safe operating regions compared to changing the d_{lead}. This demonstrates the effectiveness of the N_{uv} compensation to anticipate the hydrodynamic interactions and to appropriately adjust the desired heading angle. The N_{uv} compensation outlined in equation (6.1) is especially beneficial for the medium and large UUVs. This is largely because of the square-cube law. This law states that the forces and moments experienced by the UUVs increase in proportion to the surface area, or square of the characteristic length. However, the mass and inertial properties of the UUV increase in proportion to the volume, or the cube of the characteristic length. As such, as a UUV becomes larger, its inertial properties increase faster than the forces and moments it experiences, so the vehicle is more resistant to accelerations. Also, there is no single UUV heading and speed that can balance all of the different hydrodynamic interactions acting on the vehicle. As such, the small UUV experiences larger deviations from its course due to the other uncompensated hydrodynamic interactions when compared to the larger UUVs. Larger UUVs have enough inertia to be resistant to these uncompensated forces.

In equation (6.1), the γ parameter is present to allow for the tuning of the N_{uv} compensation. If the moment from the N_{uv} exactly offsets the moment predicted by the GP surrogate N_s, then $\gamma = 1$. For the medium and large UUVs, $\gamma = 1$ works very well. However, for the small UUV with smaller inertial properties, this value is too low. The new compensated heading angle is not aggressive enough to overcome the hydrodynamic interactions. However, by selecting a γ that is too large, the UUV is too aggressive and overcorrects from the hydrodynamic interactions. The following figure illustrates the impact of γ on the compensated operating envelope of the small UUV.

(a) N_{uv} compensation for small UUV with $\gamma = 1$

(b) N_{uv} compensation for small UUV with $\gamma = 5$

(c) N_{uv} compensation for small UUV with $\gamma = 10$

Figure 6-8: Impact of γ on the N_{uv} compensated operating envelopes for a small UUV that is traveling at the same speed as the submarine at $U_{sub} = 1.5$ m/s (≈3 knots) with $d_{lead} = 3L_{UUV}$ and no waves. The γ parameter can cause the UUV to undercorrect and overcorrect for the hydrodynamic interactions.

Figure 6-8 shows how the N_{uv} compensated small UUV with $\gamma = 1$ has a smaller safe operating region than when $\gamma = 5$. However, when the parameter is increased to $\gamma = 10$, the vehicle overcorrects which reduces the safe operating envelope of the vehicle. As such, there is a γ for each vehicle which maximizes the size of the safe operating envelope.

Due to the square-cube law, the medium and large UUVs perform much better when the yaw moment from the hydrodynamic interaction surrogate N_s equals the yaw moment from the N_{uv} coefficient. This means that the γ values for these vehicles are much closer to one. The final values identified for γ for the small, medium, and large UUVs respectively are 5.22, 1.30, and 1.03. An empirical equation is developed to predict the γ parameter based on the combined mass and added mass $\mathbf{M_{11}}$ of the

UUV moving in the forward direction. This is the term in the first row and column of the inertial matrix $\mathbf{M}$ in equations (5.10) and (5.20). The values of $\mathbf{M_{11}}$ for the small, medium, and large UUVs are 33.6 kg, 212.9 kg, and 6020 kg respectively. Equation (6.4) provides a means of determining γ based on the $\mathbf{M_{11}}$ term of the UUV.

$$\gamma(M_{11}) = 10^{4.538(\log_{10}(\mathbf{M_{11}}))^{-4.364}} \tag{6.4}$$

Because these values of γ provided the largest safe regions in the operating envelopes, they are used as the default values throughout this study. This includes the operating envelopes in figure 6-7.

6.4.2 Effects of Waves

Determining the robustness of the UUV against perturbations is important to the investigation of the UUV maneuvering capability during launch and recovery. Ocean waves provide the most applicable means of large perturbations experienced by the UUV. These perturbations caused by ocean waves are incorporated into the UUV motion simulator as discussed in section 5.8. In order to be conservative, these perturbations are assumed to be in the worse case direction that pushes the UUV toward or away from the submarine, rather than in an orthogonal direction. These perturbations also vary in magnitude based on the sea state and operating depth of the UUV. The following figure shows how the operating envelopes of the different size UUVs with and without N_{uv} compensation are affected by the ocean waves. The waves are sea state 5 and the UUV operating depth is 50 meters with a lead distance of $d_{lead} = 3L_{UUV}$.

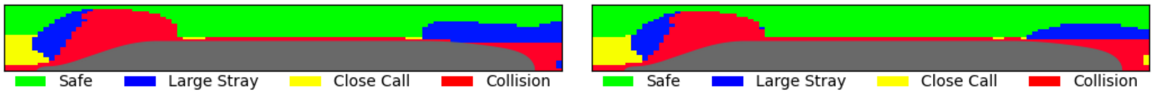

(a) Small UUV operating envelope *without* N_{uv} compensation in sea state 5 at 50 meters deep.

(b) Small UUV operating envelope *with* N_{uv} compensation in sea state 5 at 50 meters deep.

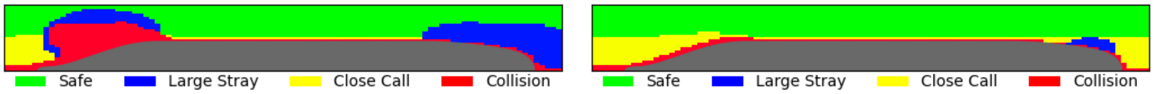

(c) Medium UUV operating envelope *without* N_{uv} compensation in sea state 5 at 50 meters deep.

(d) Medium UUV operating envelope *with* N_{uv} compensation in sea state 5 at 50 meters deep.

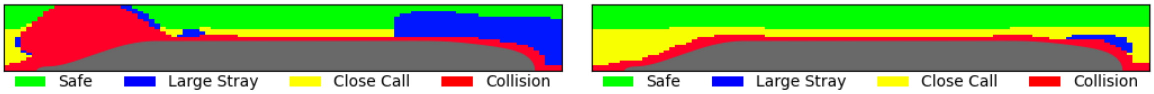

(e) Large UUV operating envelope *without* N_{uv} compensation in sea state 5 at 50 meters deep.

(f) Large UUV operating envelope *with* N_{uv} compensation in sea state 5 at 50 meters deep.

Figure 6-9: Operating envelopes for different size UUVs with and without N_{uv} compensation in sea state 5 at a depth of 50 meters. The UUVs are traveling at the same speed as the submarine at $U_{sub} = 1.5$ m/s ($\approx$3 knots) with $d_{lead} = 3L_{UUV}$. Providing N_{uv} compensation increases the size of the safe operating envelope.

Figure 6-9 shows how using the N_{uv} compensating behavior dramatically increases the safe operating envelope for the medium and large UUV. However, due to the square-cube law, the small UUV is not able to overcome the perturbations and hydrodynamic interactions as easily, so the improvements on the safe operating envelope are minimal.

Figure 6-10 provides another scenario of different size UUVs at sea state 6 with the UUV operating depth is 90 meters with a lead distance of $d_{lead} = 3L_{UUV}$. This figure compares the safe operating envelopes for UUVs with and without N_{uv} compensation.

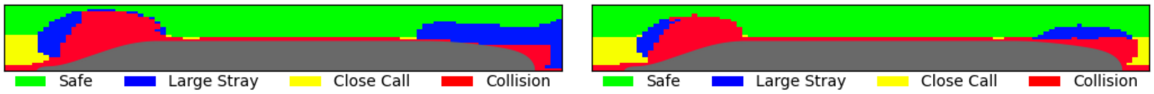

(a) Small UUV operating envelope *without* N_{uv} compensation in sea state 6 at 90 meters deep.

(b) Small UUV operating envelope *with* N_{uv} compensation in sea state 6 at 90 meters deep.

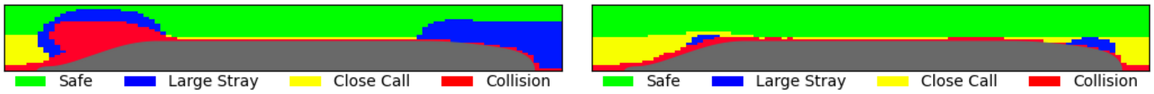

(c) Medium UUV operating envelope *without* N_{uv} compensation in sea state 6 at 90 meters deep.

(d) Medium UUV operating envelope *with* N_{uv} compensation in sea state 6 at 90 meters deep.

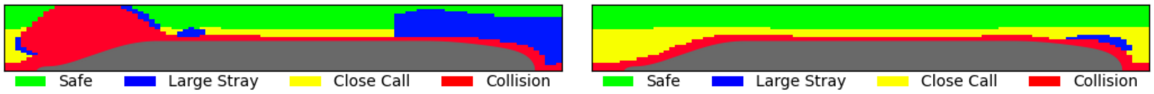

(e) Large UUV operating envelope *without* N_{uv} compensation in sea state 6 at 90 meters deep.

(f) Large UUV operating envelope *with* N_{uv} compensation in sea state 6 at 90 meters deep.

Figure 6-10: Operating envelopes for different size UUVs with and without N_{uv} compensation in sea state 6 at a depth of 90 meters. The UUVs are traveling at the same speed as the submarine at $U_{sub} = 1.5$ m/s ($\approx$3 knots) with $d_{lead} = 3L_{UUV}$. Providing N_{uv} compensation increases the size of the safe operating envelope.

By providing N_{uv} compensation, the safe operating envelopes are able to drastically increase in size for the medium and large UUV. The N_{uv} compensation provides an improvement in the operating envelope of the small UUV, but it still has regions near the bow and stern of the submarine which result in a collision, similar to figures 6-7, 6-8, and 6-9. Again, this is due to the square-cube law.

There is a limit to the improvement that N_{uv} compensation can provide. The following figure compares the operating envelopes for UUVs with and without N_{uv} compensation at sea state 6, 50 meters deep, with a lead distance of $d_{lead} = 3L_{UUV}$.

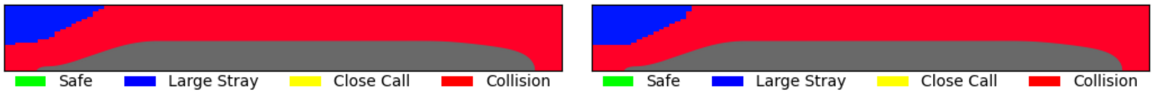

(a) Small UUV operating envelope *without* N_{uv} compensation in sea state 6 at 50 meters deep.

(b) Small UUV operating envelope *with* N_{uv} compensation in sea state 6 at 50 meters deep.

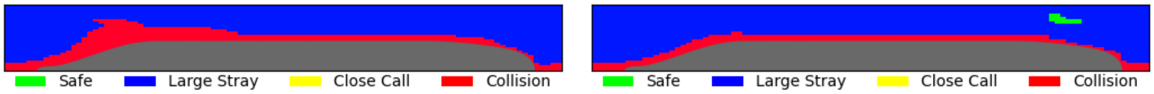

(c) Medium UUV operating envelope *without* N_{uv} compensation in sea state 6 at 50 meters deep.

(d) Medium UUV operating envelope *with* N_{uv} compensation in sea state 6 at 50 meters deep.

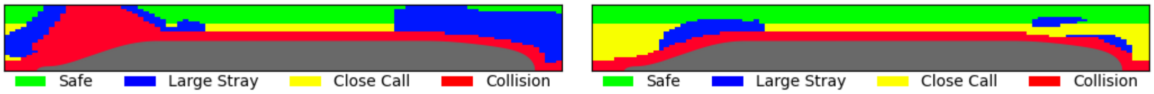

(e) Large UUV operating envelope *without* N_{uv} compensation in sea state 6 at 50 meters deep.

(f) Large UUV operating envelope *with* N_{uv} compensation in sea state 6 at 50 meters deep.

Figure 6-11: Operating envelopes for different size UUVs with and without N_{uv} compensation in sea state 6 at a depth of 50 meters. The UUVs are traveling at the same speed as the submarine at $U_{sub} = 1.5$ m/s (≈3 knots) with $d_{lead} = 3L_{UUV}$. Providing N_{uv} compensation improved the operating envelope for the large UUV, but not the small and medium.

Figure 6-11 shows that the N_{uv} compensated small and medium UUVs have little to no improvement for their operating envelopes. At sea state 6 and 50 meters deep, the perturbations are too large to allow a safe operating region, even with N_{uv} compensation. The N_{uv} behavior does provide some improvement to the large UUV because the unsafe operating regions are caused by the hydrodynamic interactions rather than the wave perturbations.

In summary, there are two forces that reduce the safe operating regions of the UUV around the submarine. These are the wave perturbations and the hydrodynamic interaction. The N_{uv} compensating behavior does well at overcoming the hydrodynamic interactions and maintains the same robustness against the perturbations of the ocean waves inherent in the UUV control system. As discussed in section 5.11.3, in sea state 5 at 50 meters deep, the UUVs have similar operating envelopes as the no wave condition. However, at higher sea states or shallower depths, the UUVs may experience large increases in the size of the regions where large strays or collisions occur. The N_{uv} compensation provides little improvement to the operating envelopes in these conditions because the effects of the wave perturbations dominate the hydrodynamic interactions.

6.5 Conclusions

A GP surrogate model of the hydrodynamic interaction forces and moments between a UUV and a submarine is used to simulate UUV motion during launch and recovery operations. A method is developed to incorporate this GP surrogate model of the hydrodynamic interactions into the autonomous behaviors of the UUV. This enables the UUV autonomous behaviors to anticipate the hydrodynamic interactions and appropriately adjust the desired heading and speed.

As discussed in section 5.12, there are regions near the bow and stern of the submarine that result in large strays from the track-line or collisions between the two vehicles. Also, lateral approaches prove problematic to standard UUV autonomous behaviors because they do not account for the moving inertial frame of the submarine. This means that the standard waypoints behavior causes the UUV to experience large strays from the track-line when there are strong cross-flows. In order to account for these two problems, two separate UUV autonomous behaviors are developed. The first is known as N_{uv} compensation. This behavior adjusts the desired heading so that the hydrodynamic interaction yaw moment N_s offsets the moment caused by the incident flow. This N_{uv} compensating behavior is shown to allow the UUV to overcome the hydrodynamic interactions well beyond the capability of the standard waypoints behavior. The second behavior is known as the modified waypoints behavior. This behavior accounts for the fact that the inertial reference frame is fixed to a moving submarine as opposed to an earth-fixed reference frame like the standard waypoints behavior. This modified waypoints behavior enables the UUV to stay on course, even when there is a large flow that crosses the UUV track line. These new behaviors increase the safe operating envelopes during launch and recovery operations.

Chapter 7

Conclusion

7.1 Summary

The objective of this study is to develop a methodology for simulating UUV maneuvering around a moving submarine by accurately predicting the complex hydrodynamic interactions in real time using actively sampled Gaussian Process regression as a surrogate model. A Non-Myopic Multi-Fidelity active sampling method has been developed that utilizes the low cost of a low fidelity potential flow model to explore the design space while leveraging the high accuracy of a high fidelity CFD simulator to create a surrogate model. The new approach outperforms other benchmark methods and improves the efficiency of computing reduced order models due to its non-myopic active search properties. This method is also generalizable to actively sample data points across other problems using a multi-fidelity framework.

This GP regression surrogate enables the real-time prediction of the UUV hydrodynamic interactions based on the accurate CFD training data. Real-time modeling of these hydrodynamic interactions is essential to simulate UUV autonomy and control around moving submarines. Using CFD to computationally model the hydrodynamic interactions between a submarine and UUV is an approach that has been validated by tow tank experiments. Although the CFD setup has been validated, it is still too computationally expensive to be evaluated in real time in order to be incorporated into a UUV maneuvering simulator. Other hydrodynamic approaches like potential flow or the "one-way" assumption are fast enough to be evaluated in real time, but lack the necessary accuracy of CFD. The GP regression surrogate bridges this gap between speed and accuracy by using the actively sampled CFD data as training data to predict the hydrodynamic interactions in real time. This enables the simulation of UUV maneuvering around moving submarines.

A method of incorporating a GP surrogate model into the equations of motion of a UUV motion simulator is developed in order to evaluate the impact of the hydrodynamic interactions between the two vehicles. This enables the evaluation of the UUV autonomous behavior and control system against the hydrodynamic interactions. Because this can be simulated rapidly, this allows for the creation of safe operating envelopes in which the UUV is capable of overcoming the hydrodynamic interactions. The simulations of how the hydrodynamic interactions impact the UUV motion show that there are regions near the bow and stern of the submarine just beyond the parallel mid-body section that result in either a large straying from the track-line or in collisions between the two vehicles. These unsafe operating regions extend laterally from the bow and stern of the submarine so certain overtaking maneuvers may not be feasible with standard UUV autonomous behaviors. Also, lateral approaches prove problematic to standard UUV autonomous behaviors because they do not account for the moving inertial frame of the submarine so the UUV has large strays from the track-line. While waves provide perturbations that have the potential to be problematic, it is not until sea state 6 at the minimum likely depth of 50 meters deep that these perturbations have a significant impact on the safe operating envelopes of the vehicles.

Additionally, a method is developed to incorporate this GP surrogate model of the hydrodynamic interactions into the autonomous behaviors of the UUV. This enables the UUV autonomous behaviors to anticipate the hydrodynamic interactions and appropriately adjust the desired heading and speed in order to stay on course. Lateral approaches and regions near the bow and stern of the submarine are problematic for current UUV autonomous behaviors. In order to account for these two problems, two separate UUV autonomous behaviors are developed. The first is known as N_{uv} compensation which adjusts the desired heading so that the hydrodynamic interaction yaw moment offsets the moment caused by the incident flow. This N_{uv} compensating behavior is shown to allow the UUV to overcome the hydrodynamic interactions well beyond the capability of the standard waypoints behavior in the bow and stern regions near the submarine. The second behavior, known as the modified waypoints behavior, accounts for the fact that the inertial reference frame is fixed to a moving submarine as opposed to an earth-fixed reference frame like the standard waypoints behavior. This modified waypoints behavior enables the UUV to stay on course during lateral approaches. These new behaviors increase the safe operating envelopes during launch and recovery operations and are just as robust to waves as existing behaviors.

7.2 Future Work

Future work for this research may include increasing the dimensionality of the input space by considering more parameters, i.e. more complex and realistic setups. This would require more complex and higher dimension surrogate models, and may even require those based on neural networks or operators [83]. This additional complexity could include introducing movable control surfaces on the UUV, modeling transient UUV behavior, accounting for six degrees of freedom motion by allowing the axes of the two vehicles to be non-planar, or simulating the hydrodynamic interactions near a submarine appendage like the sail or a dry deck shelter. This added complexity could also reduce the need for some of the assumptions made for this research. For example, by modeling the UUV transient behavior, the quasi-static assumption could be removed.

Additionally, the application of the non-myopic multi-fidelity sampling algorithm is currently formulated for only two levels of fidelity. An extension to more levels of fidelity is straightforward and may be beneficial for other CFD problems, like using variable-resolution CFD models. This is also left to be explored in future work.

More work could be performed in validating the UUV simulator with the incorporated hydrodynamic interactions surrogate. While the individual components have been validated, there has been no system-level validation of the simulations because there is no real-world data available for comparison. Collecting this data with real-world UUVs and submarines would provide a means of validating the UUV simulations.

This research also used generic hull forms for the submarine and UUV. While these hull forms are generally applicable to UUVs and submarines, vehicles with slightly different hull shapes will experience slightly different hydrodynamic interactions. This research could be expanded to explore the viability of the L&R operations of specific vehicles.

This study did not explore any UUV positions that are directly in front of or behind the submarine due to the possibility of collisions and design space priority from project sponsors. However, L&R of UUVs from torpedo tubes is also a real option so exploring the hydrodynamic interactions in front of the bow of the submarine is valuable.

Appendix A

Code Documentation

A.1 Overview

In order to perform the UUV motion simulation, a collection of Python code is developed which combines Gaussian Process Regression code built using the GPy library and custom code that is modeled off of the MOOS-IvP architecture which is an open-source C++ simulator for autonomous underwater vehicles. However, the MOOS-IvP architecture uses a kinematic simulator so forces and moments are never used to determine the UUV motion.

There are two possible system integration approaches to allow the python based hydrodynamic interaction surrogate to be incorporated into the C++ UUV simulator. The first is to create a new uSimMarine app that incorporates the equations of motion in order to perform dynamic simulations, rather than kinematic simulations. The surrogate is developed in python using robust open-source GPy libraries. Because the surrogate is written in python, it would have to be embedded into C++ using a python interpreter in order to be used by the new uSimMarine app and the pHelmIvp app of the MOOS-IvP architecture. The second method is to create a separate dynamic simulator in python. Next, the code and architecture of MOOS-IvP are leveraged to convert the necessary components into python in order to be compatible with the surrogate. In either scenario, the dynamic simulator using the UUV equations of motion needs to be developed because MOOS-IvP lacks this functionality. The second approach is taken because it presented less integration risk.

This framework uses three different vectors to relay information between apps within the simulator. These three different vectors are the state vector $\mathbf{x}$, input vector $\mathbf{u}$, and desired state vector $\mathbf{x_d}$ and are listed in equation (5.1) and repeated below for convenience. The propeller thrust and torque are denoted as X_{Prop} and K_{Prop} respectively while the rudder and stern plane angles are denoted as δ_r and δ_s respectively.

$$\begin{aligned} \mathbf{x} &= [u, v, w, p, q, r, x, y, z, \phi, \theta, \psi]^T \\ \mathbf{u} &= [X_{Prop}, K_{Prop}, \delta_r, \delta_s]^T \\ \mathbf{x_d} &= [u_d, ..., \psi_d]^T \end{aligned} \tag{A.1}$$

MOOS-IvP is an open-source C++ UUV simulator that uses three basic apps to model the UUV control system and its impact on UUV motion. The pHelmIvP app takes in the state vector of the vehicle position and motion and uses an autonomous behavior to compute a new desired input vector containing the new desired speed and heading. The autonomous behaviors may be the standard waypoints behavior, modified waypoints behavior, ot it may use the surrogate to adjust the desired speed and heading using the N_{uv} compensating behavior detailed in section 6.3.1. This desired input vector is then passed to the pMarinePID app which simulates a PID controller using equation (5.21) in order to determine the input vector of the propeller thrust and torque, as well as the angle of the stern planes and rudder. This input vector, as well as the state vector, is then passed to the uSimMarine app which updates the vehicle state, position, and trajectory using the equations of motion. These equations of motion incorporate the hydrodynamic interactions from the surrogate model as outlined in equations (5.20). This creates a new state vector for the UUV. The process is iterated continually throughout the simulation and simulations are iterated to create operating envelopes. Figure 5-2 shows an overview of the simulation architecture.

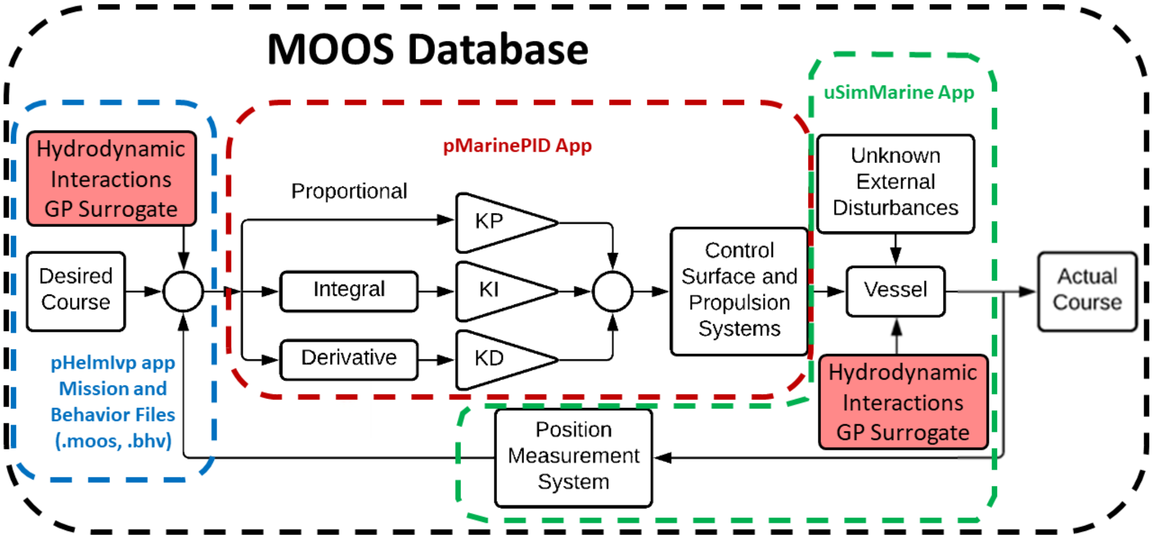

Figure A-1: Integration of the hydrodynamic interactions surrogate into the MOOS-IvP architecture. The GP surrogate is embedded in the pHelmIvP app to enable the implementation of new autonomous behaviors as well as the uSimMarine app to allow the surrogate to impact the equations of motion.

The code for this research is too long to be included in this appendix but may be made available at the request of the author. Chapters 2, 4, 5, and 6 provide a detailed description of all of the methods and equations used to create this UUV simulator.

THIS PAGE INTENTIONALLY LEFT BLANK

Bibliography

[1] Joseph A. Walsh and Roger M. Smith. *The Navy Unmanned Undersea Vehicle (UUV) Master Plan*. Nov. 9, 2004.

[2] Pete Small. “Unmanned Maritime System Update”. Jan. 15, 2019.

[3] Zhi Quan Leong. “Effects of Hydrodynamic Interaction on an AUV Operating Close to a Moving Submarine”. In: *Australian Maritime College, University of Tasmania* (Nov. 2014).

[4] K S Varyani’ and M Vantorre’. “New Generic Equation for Interaction Effects on a Moored Containership Due to a Passing Tanker”. In: *JOURNAL OF SHIP RESEARCH* (2006), p. 11.

[5] Kevin Michael Byrne. “Real-time modeling of cross-body flow for torpedo tube recovery of the Phoenix Autonomous Underwater Vehicle (AUV)”. In: *Naval Postgraduate School* (1998), p. 241.

[6] Roy Burcher and Louis J. Rydill. *Concepts in Submarine Design*. Cambridge University Press, Oct. 1995. ISBN: 978-1-139-92723-9.

[7] L. Eça and M. Hoekstra. “A procedure for the estimation of the numerical uncertainty of CFD calculations based on grid refinement studies”. In: *Journal of Computational Physics* 262 (Apr. 2014), pp. 104–130. ISSN: 00219991. DOI: `10.1016/j.jcp.2014.01.006`.

[8] Jin-Yeong Park et al. “Development of Test-Bed AUV ’ISiMI’ and Underwater Experiments on Free Running and Vision Guided Docking”. In: *Underwater Vehicles*. Ed. by Alexander V. InTech, Jan. 1, 2009. ISBN: 978-953-7619-49-7. DOI: `10.5772/6712`.

[9] M Mackay. “Estimation of Submarine Near-Bottom Hydrodynamic Loads and Squat”. In: *Defence Research and Development Canada Technical Memorandum* (2003), p. 54.

[10] “Report of the Resistance and Flow Committee”. In: *Proceedings Volume 1: 19th ITTC*. ITTC, Sept. 1990.

[11] “Captive Model Test Procedures”. In: ITTC, Sept. 2014.

[12] Ronald O’Rourke. “Navy Columbia (SSBN-826) Class Ballistic Missile Submarine Program: Background and Issues for Congress”. In: *Congressional Research Summary Report* (2020), p. 60.

[13] Tristan Perez, Alejandro Donaire, and Francis Valentinis. “Parametric Modelling of Interacting Hydrodynamic Forces in Underwater Vehicles Operating in Close Proximity”. In: *IFAC-PapersOnLine* 51.29 (2018), pp. 92–97. ISSN: 24058963. DOI: `10.1016/j.ifacol.2018.09.475`.

[14] J N Newman. *Marine Hydrodynamics*. 40th Anniversary. MIT Press, 2017. ISBN: 978-0-262-53482-6.

[15] Thor I Fossen. *Handbook of Marine Craft Hydrodynamics and Motion Control*. John Wiley & Sons, Ltd, 2011. ISBN: 978-1-119-99149-6.

[16] B. Nirman Jayarathne et al. “Accuracy of Potential Flow Methods to Solve Real-time Ship-Tug Interaction Effects within Ship Handling Simulators”. In: *TransNav, the International Journal on Marine Navigation and Safety of Sea Transportation* 8.4 (2014), pp. 497–504. ISSN: 2083-6473. DOI: `10.12716/1001.08.04.03`.

[17] Arthur M Jaffe. “The Millennium Grand Challenge in Mathematics”. In: *Notices of the AMS* 53.6 (2006), p. 9.

[18] Parviz Moin and Krishnan Mahesh. “Direct Numerical Simulation: A Tool in Turbulence Research”. In: *Annual Review of Fluid Mechanics* 30.1 (1998), pp. 539–578. DOI: `10.1146/annurev.fluid.30.1.539`. eprint: `https://doi.org/10.1146/annurev.fluid.30.1.539`.

[19] Robert Fedor. “Simulation of a Launch and Recovery of an UUV to an Submarine”. Thesis. Royal Institute of Technology, 2009.

[20] Carl Edward Rasmussen and Christopher K. I. Williams. *Gaussian processes for machine learning*. Adaptive computation and machine learning. OCLC: ocm61285753. Cambridge, Mass: MIT Press, 2006. 248 pp. ISBN: 978-0-262-18253-9.

[21] Joan Fisher Box. “R. A. Fisher and the Design of Experiments, 1922-1926”. In: *Taylor & Francis, Ltd* (2020), p. 8.

[22] Milton Friedman and L. J. Savage. “PLANNING EXPERIMENTS SEEKING MAXIMA”. In: *Selected Techniques of Statistical Analysis for Scientific and Industrial Research, and Production and Management Engineering*. New York and London: McGraw-Hill, 1947, pp. 363–373.

[23] J. Sacks, W. J. Welch, and T. J. Mitchell. “Design and analysis of computer experiments”. In: *Statistical Science* 4 (1989), pp. 409–423.

[24] K. Chaloner and I. Verdinelli. “Bayesian experimental design: A review”. In: *Statistical Science* 10 (1995), pp. 273–304.

[25] A. Blanchard and T. Sapsis. “Output-Weighted Optimal Sampling for Bayesian Experimental Design and Uncertainty Quantification”. In: *SIAM/ASA J. Uncertainty Quantification* 9 (2021), pp. 564–592.

[26] Javier Gonzalez, Michael Osborne, and Neil D Lawrence. “GLASSES: Relieving The Myopia Of Bayesian Optimisation”. In: *Proceedings of the 19th International Conference on Artificial Intelligence and Statistics (AISTATS)* (2015).

[27] *FS-Flow User manual*. URL: `www.dnvgl.com`.

[28] P. Perdikaris et al. “Multi-fidelity modelling via recursive co-kriging and Gaussian-Markov random fields.” In: *Proceedings. Mathematical, physical, and engineering sciences / the Royal Society* 471.2179 (July 2015), p. 20150018. ISSN: 1364-5021. DOI: `10.1098/rspa.2015.0018`.

[29] M. Kennedy. “Predicting the output from a complex computer code when fast approximations are available”. In: *Biometrika* 87.1 (Mar. 1, 2000), pp. 1–13. ISSN: 0006-3444, 1464-3510. DOI: `10.1093/biomet/87.1.1`.

[30] Shali Jiang et al. “Efficient Nonmyopic Active Search”. In: *Proceedings of the 34 th International Conference on Machine Learning* (2017), p. 10.

[31] Andrew Gordon Wilson and Ryan Prescott Adams. “Gaussian Process Kernels for Pattern Discovery and Extrapolation”. In: *Proceedings of the 30 th International Conference on Machine Learning* (2013), p. 9.

[32] R. B. Gramacy and H. K. Lee. “Adaptive design and analysis of supercomputer experiments”. In: *Techno- metrics* 51 (2009), pp. 130–145.

[33] Michael A Osborne, Roman Garnett, and Stephen J Roberts. *Gaussian Processes for Global Optimization.* 2008.

[34] Philippe Morere, Roman Marchant, and Fabio Ramos. “Bayesian Optimisation for solving Continuous State-Action-Observation POMDPs”. In: *30th Conference on Neural Information Processing Systems* (2016), p. 5.

[35] Andreas Damianou and Neil D. Lawrence. “Deep Gaussian Processes”. In: *Proceedings of the Sixteenth International Conference on Artificial Intelligence and Statistics.* Ed. by Carlos M. Carvalho and Pradeep Ravikumar. Vol. 31. Proceedings of Machine Learning Research. Scottsdale, Arizona, USA: PMLR, 2013, pp. 207–215.

[36] P. Perdikaris et al. “Nonlinear information fusion algorithms for data-efficient multi-fidelity modelling”. In: *Proceedings of the Royal Society A: Mathematical, Physical and Engineering Sciences* 473.2198 (Feb. 2017), p. 20160751. ISSN: 1364-5021, 1471-2946.

[37] D Cox et al. *Tuning complex computer code to data.* Technical Report AD-P-007148/0/XAB. United States: Illinois Univ., Urbana, IL. Dept. of Statistics, Jan. 1, 1992.

[38] Shifeng Xiong, Peter Z. G. Qian, and C. F. Jeff Wu. “Sequential Design and Analysis of High-Accuracy and Low-Accuracy Computer Codes”. In: *Technometrics* 55.1 (Feb. 2013), pp. 37–46. ISSN: 0040-1706, 1537-2723. DOI: `10.1080/00401706.2012.723572`.

[39] Eric Constans. *How to Simulate a Trebuchet Part 2: Equations of Motion.* 2013. URL: `http://www.benchtophybrid.com/TB_index.html`.

[40] Donald B. Siano. *Trebuchet Mechanics.* Nov. 16, 2013.

[41] Shawn Rutan and Becky Wieczorek. “Modern Siege Weapons: Mechanics of the Trebuchet”. In: (), p. 47.

[42] William V Harper and Sumant K Gupta. “Sensitivity/Uncertainty Analysis of a Borehole Scenario Comparing Latin Hypercube Sampling and Deterministic Sensitivity Approaches”. In: *Office of Nuclear Waste Isolation* (1983).

[43] Pasquale Sforza. “Wing Design”. In: *Commercial Airplane Design Principles.* Elsevier, 2014, pp. 119–212. ISBN: 978-0-12-419953-8. DOI: `10.1016/B978-0-12-419953-8.00005-X`.

[44] R. D. Finck. *USAF Stability and Control DATCOM.* Apr. 1978.

[45] Mauricio A. Alvarez, Lorenzo Rosasco, and Neil D. Lawrence. “Kernels for Vector-Valued Functions: a Review”. In: *arXiv:1106.6251 [cs, math, stat]* (Apr. 16, 2012). arXiv: `1106.6251`.

[46] Sonja Surjanovic and Derek Bingham. *Virtual Library of Simulation Experiments: Test Functions and Datasets*. 2013. URL: https://www.sfu.ca/~ssurjano/index.html.

[47] Xujian Lyu et al. *Simulation of Microbubble Resistance Reduction on a SUBOFF Model*. June 2014.

[48] Kenshiro Takahashi and Prasanta K. Sahoo. “Fundamental CFD Study on the Hydrodynamic Performance of the DARPA SUBOFF Submarine”. In: *Volume 2: CFD and FSI*. ASME 2019 38th International Conference on Ocean, Offshore and Arctic Engineering. Glasgow, Scotland, UK: American Society of Mechanical Engineers, June 9, 2019, V002T08A052. ISBN: 978-0-7918-5877-6. DOI: 10.1115/OMAE2019-96190.

[49] Nancy C. Groves, Thomas T. Huang, and Ming S. Chang. *Geometric Characteristics of DARPA SUBOFF Models*. Mar. 1989.

[50] Thomas T. Huang, Han-Lieh Liu, and Nancy C. Groves. *Experiments of the DARPA SUBOFF Program*. Dec. 1989.

[51] Robert F. Roddy. *Investigation of the Stability and Control Characteristics of Several Configurations of the DARPA SUBOFF Model(DTRC MODEL 5470) from Captive-Model Experiments*. Sept. 1990.

[52] Han-Lieh Liu and Thomas T. Huang. *Summary of DARPA Suboff Experimental Program Data*. June 1998.

[53] *Explorer AUV*. International Submarine Engineering. URL: https://ise.bc.ca/product/explorer/ (visited on 09/09/2020).

[54] “Practical Guidelines for Ship CFD Applications”. In: ITTC, Sept. 2014.

[55] Mohammad Moonesun, Yuri Korol, and Hosein Dalayeli. “CFD Analysis on the Bare Hull Form of Submarines for Minimizing the Resistance”. In: *International Journal of Maritime Technology* (2015), p. 16.

[56] Mohammad Moonesun et al. “CFD analysis of the bow shapes of submarines”. In: *Journal of Scientific and Engineering Research* (2016), p. 16.

[57] Christiaan M Klaij and Guilherme Vaz. “Numerical Uncertainty Estimation in Maritime CFD Applications”. In: *6th European Conference on Computational Fluid Dynamics* (2014), p. 11.

[58] B M Duda et al. “Scale-adaptive simulation of a hot jet in cross flow”. In: *Journal of Physics: Conference Series* 318.4 (Dec. 22, 2011), p. 042050. ISSN: 1742-6596. DOI: 10.1088/1742-6596/318/4/042050.

[59] F. R. Menter. “Two-equation eddy-viscosity turbulence models for engineering applications”. In: *AIAA Journal* 32.8 (Aug. 1994), pp. 1598–1605. ISSN: 0001-1452, 1533-385X. DOI: 10.2514/3.12149.

[60] R Pankajakshan et al. “Validation of Control-Surface Induced Submarine Maneuvering Simulations using UNCLE”. In: *24th Symposium on Naval Hydrodynamics* (2002), p. 16.

[61] Morton Gertler and Grant R. Hagen. *Standard Equations of Motion for Submarine Simulation*. June 1967.

[62] “Trident II D-5 Fleet Ballistic Missile”. In: *Federation of American Scientists* (May 1, 1998). URL: https://fas.org/nuke/guide/usa/slbm/d-5.htm.

[63] Leong et al. "Investigation into the Hydrodynamic Interaction Effects on an AUV Operating Close to a Submarine". In: *Australian Maritime College, University of Tasmania* (Jan. 2013).

[64] Timothy Prestero. *Verification of a six-degree of freedom simulation model for the REMUS autonomous underwater vehicle*. Woods Hole, MA: Massachusetts Institute of Technology and Woods Hole Oceanographic Institution, 2001. DOI: 10.1575/1912/3040.

[65] Michael R Benjamin, Henrik Schmidt, and Paul Newman. *An Overview of MOOS-IvP and a Users Guide to the IvP Helm - Release 19.8*. Aug. 29, 2021.

[66] David C Warner. "Design, simulation, and experimental verification of a computer model and enhanced position estimator for the NPS AUV II". Thesis. Naval Postgraduate School, Dec. 1991.

[67] Brady M Hammond. "Hydrodynamic Interactions of an Unmanned Underwater Vehicle Operating in Close Proximity to a Moving Submarine". PhD thesis. Massachusetts Institute of Technology, 2021.

[68] *Multi-National Submarine and Anti-Submarine Exercise Manual*. Mar. 2002.

[69] *AUV System Spec Sheet*. URL: https://auvac.org/226-2/.

[70] *Bluefin SandShark Unmanned Underwater Vehicle (UUV)*. URL: https://gdmissionsystems.com/products/underwater-vehicles/bluefin-sandshark-autonomous-underwater-vehicle#:~:text=The%20Bluefin%20SandShark%C2%AE%20is,platform%20for%20the%20next%20generation..

[71] *IVER 3 AUV Specifications*. URL: https://auvac.org/files/uploads/platform_pdf/iver3_auv_brochure.pdf.

[72] Katherine Owens. "New Navy Class III Undersea Drone to be in the Water by 2019". In: *Defense Systems* (Apr. 6, 2017).

[73] Brady M. Hammond and Themistoklis P. Sapsis. "Reduced order modeling of hydrodynamic interactions between a submarine and unmanned underwater vehicle using non-myopic multi-fidelity active learning [Manuscript submitted for publication]". In: *Ocean Engineering* (2023).

[74] Nastasia E. Winey. *Modifiable Stability and Maneuverability of High Speed Unmanned Underwater Vehicles (UUVs) Through Bioinspired Control Fins*. Woods Hole, MA: Massachusetts Institute of Technology and Woods Hole Oceanographic Institution, 2020. DOI: 10.1575/1912/26053.

[75] Xiaoxu Du, Zeqi Zheng, and Shumiao Guan. "Numerical Calculation of Hydrodynamic Interactions of Submarine Flow on AUV". In: *2018 OCEANS - MTS/IEEE Kobe Techno-Oceans (OTO)*. 2018 OCEANS - MTS/IEEE Kobe Techno-Ocean (OTO). Kobe: IEEE, May 2018, pp. 1–5. ISBN: 978-1-5386-1654-3. DOI: 10.1109/OCEANSKOBE.2018.8558789.

[76] Edward V. Lewis. *Principles of Naval Architecture Second Revision*. Vol. III - Motions in Waves and Controllability. The Society of Naval Architects and Marine Engineers, 1989.

[77] George Ellis. "Four Types of Controllers". In: *Control System Design Guide*. Elsevier, 2012, pp. 97–119. ISBN: 978-0-12-385920-4.

[78] Alistair Adcroft et al. "The GFDL Global Ocean and Sea Ice Model OM4.0: Model Description and Simulation Features". In: *Journal of Advances in Mod-*

eling Earth Systems 11.10 (Oct. 2019), pp. 3167–3211. ISSN: 1942-2466, 1942-2466. DOI: `10.1029/2019MS001726`.

[79] Thomas R. Osborn and Rolf G. Lueck. "Turbulence Measurements with a Submarine". In: *Journal of Physical Oceanography* 15.11 (Nov. 1985), pp. 1502–1520. ISSN: 0022-3670, 1520-0485. DOI: `10.1175/1520-0485(1985)015<1502:TMWAS>2.0.CO;2`.

[80] Kathryn K. McCreight. *A Note on the Selection of Wave Spectra for Design Evaluation*. Jan. 1998.

[81] Anthony J Healey and David Lienard. "Multivariable sliding mode control for autonomous diving and steering of unmanned underwater vehicles". In: *IEEE Journal of Oceanic Engineering* 18 (July 1993), p. 14.

[82] Armin Doerry. *Ship dynamics for maritime ISAR imaging.* SAND2008-1020, 929523. Feb. 1, 2008, SAND2008–1020, 929523. DOI: `10.2172/929523`.

[83] E. Pickering et al. "Discovering and forecasting extreme events via active learning in neural operators". In: *Nature Computational Science (Accepted)* (2022), p. 19.